UNIVERSITÀ
DEGLI STUDI
DI PADOVA

Sede Amministrativa: Università degli Studi di Padova

Dipartimento di Fisica Tecnica

SCUOLA DI DOTTORATO DI RICERCA IN INGEGNERIA INDUSTRIALE
INDIRIZZO FISICA TECNICA
CICLO XXIII

THEORETICAL AND EXPERIMENTAL STUDY OF SOLAR THERMAL COLLECTOR SYSTEMS AND COMPONENTS

Direttore della Scuola: Prof. Paolo Bariani
Coordinatore d'indirizzo: Prof. Luisa Rossetto
Supervisore: Prof. Alberto Cavallini
Correlatore: Prof. Davide Del Col

Dottorando: Enrico Zambolin

Abstract

Flat-plate and evacuated tube collectors are the most widely used device to convert solar radiation into heat. In conventional applications they can provide energy for domestic hot water or space heating in combination with low water temperature systems.

Testing of thermal efficiency and optimisation of these solar thermal collectors are addressed and discussed in the present work.

A new set of experimental data has been used to evaluate the performance of flat-plate and evacuated collectors at various conditions. Efficiency is measured following the standard EN 12975: standard efficiency curves, input/output energy curves and daily efficiency curves have been obtained from tests.

This approach allows a more comprehensive comparison of the effective performance of the solar thermal collectors considered here.

A simulation tool of the flat-plate thermal collector is also proposed. The numerical model permits to obtain a "virtual collector" and provides information on the predicted performance without constructing prototypes. The three-dimensional steady-state model for flat-plate solar collector is validated comparing model predictions with experimental results obtained from experimental tests on two flat-plate collectors. Measures of the temperature profile in the copper sheet, in the glass cover and in the tubes, and an infrared analysis, are used to investigate the heat losses and optical characteristics.

The numerical model has been also used to analyse comparative effects of varying design choices, with regard to geometry and materials.

The evacuated tube collectors are in principle more expensive than flat-plate collectors and they are suitable for more higher temperature systems (space heating, absorption cooling machines..). Their geometry makes more difficult to fully characterize the collector performance. A new procedure to characterize these type of collectors has been developed and described in this thesis. Efficiency tests have been performed on a U-tube evacuated tubular collector, using a cylindrical absorber, both with and without external CPC (compound parabolic concentrator) reflectors.

Experimental results have been used to validate the new procedure and to provide information on the improvement of collectors' performance obtained through the use of external CPC reflectors.

Riassunto

I collettori solari termici maggiormente impiegati per convertire la radiazione solare in calore sono i collettori a tipologia piana e a tubi evacuati. Nelle applicazioni convenzionali essi vengono utilizzati per la produzione di acqua calda sanitaria o riscaldamento domestico in combinazione con sistemi a bassa temperatura.

Prove d'efficienza termica ed ottimizzazione di questi dispositivi solari sono affrontati e discussi in questa tesi.

Nuove prove sperimentali in varie condizioni sono state effettuate su collettori piani vetrati e a tubi evacuati per effettuare una nuova analisi comparativa. L'efficienza è stata misurata secondo le indicazioni della normativa europea EN 12975 ed inoltre si sono ricavate curve input-output e di efficienza media giornaliera.

Questo approccio permette un confronto più ampio delle prestazioni effettive dei collettori solari considerati.

Uno strumento di simulazione delle prestazioni dei collettori a geometria piana è anche proposto. Il modello numerico permette di ottenere un "collettore virtuale" e fornisce informazioni sulle prestazioni di un collettore senza costruirne un prototipo funzionale. Il modello tridimensionale stima le prestazioni di un collettore a geometria piana in condizioni stazionarie ed è stato validato confrontando le prestazioni stimate con i risultati sperimentali ottenuti su due collettori diversi. Misure di temperatura della piastra assorbente, della copertura vetrata, dei tubi dell'arpa ed analisi all'infrarosso sono stati utilizzati per investigare le dispersioni termiche e le caratteristiche ottiche della geometria considerata.

Il modello è inoltre stato usato per analizzare gli effetti di alcune scelte progettuali riguardanti la geometria e i materiali dei componenti del collettore.

I collettori solari a tubi evacuati sono in linea di principio più costosi dei collettori piani e sono idonei ad applicazioni a più alta temperatura (sistemi di riscaldamento, macchine ad assorbimento..). La loro geometria rende più difficile la caratterizzazione completa delle prestazioni del collettore. Una nuova procedura per caratterizzare questo

tipo di collettori è stata sviluppata ed è qui descritta. Sono state eseguite prove sperimentali su un collettore a tubi evacuati, con tubi ad U, con assorbitore cilindrico, con e senza riflettori CPC (compound parabolic concentrator) esterni.

I risultati sperimentali sono stati utilizzati per validare la nuova procedura e per fornire indicazioni sull'incremento dell'efficienza dovuto all'impiego dei riflettori CPC.

Index

List of figures

List of tables

Introduction

The sun is a gaseous sphere with a diameter 1.39×10^9 m, it is 1.5×10^{11} m from the earth and it emits 63 MW/m^2 on the sun's surface. A fraction of the sun's global output energy is intercepted by the earth. The solar constant is the energy heat flux received on a unit area of surface perpendicular to the direction of the radiation at mean earth-sun distance outside the atmosphere. It has been measured as 1367 W/m^2 (Duffie and Beckman, 2006).

The greatest advantage of solar energy as compared with convectional energy source is that it is clean and can be supplied without any environmental pollution. The increase in oil prices in recent years gives a push to the renewable energy technologies and so to the utilisation of the solar radiation. The rational use of these technologies is a key point to ensure their diffusion and a concrete aid to limit the use of fossil fuels.

The solar radiation is directly used mainly by means of photovoltaic modules and solar thermal collectors.

In conventional uses solar thermal collectors can provide energy for domestic hot water or space heating in combination with low water temperature systems. In areas with high sunshine, solar collectors could also be used in absorption cooling machines, cooking process and in still plants.

The diffusion of thermal solar plants is mostly related to the economic viability, which can be verified by comparing the avoided costs due to energy savings to the initial investment cost. In this context the financial aids promoted by the national and local governments play a decisive role.

Two main types of liquid solar collectors exist: flat-plate collectors (FPC) and evacuated tube collectors (ETC). They are characterized by different costs and performances. So it is very important to choose the right collector for each application to optimize the behaviour of the whole system, the energy saved and the finance payback.

These two types of solar thermal collector are analysed in this thesis. The manuscript is organised as follows:

- Chapter 1. Description of the main parameters used to define the collector efficiency.
- Chapter 2. Description of the experimental apparatus.
- Chapter 3. Comparison between flat-plate and evacuated tube collectors: experimental analysis in stationary standard and daily conditions.
- Chapter 4. Numerical model to simulate flat-plate thermal performance: description and experimental validation.
- Chapter 5. Model results obtained by model simulations.
- Chapter 6. A new procedure for the experimental characterization of evacuated tube collectors and performance comparison with and without CPC reflectors.

Chapter 1.
Collector efficiency

1.1 Introduction

A solar thermal collector is a special heat exchanger that transforms solar radiative energy in heat.

A solar collector differs in several respects from conventional heat exchangers: it does not accomplish a fluid to fluid exchange, but the energy transfer is from a distant radiant source to a fluid (the most common working fluid is a mixture of water and propylene glycol).

In this chapter are described the main parameters need to describe the solar thermal collector performance.

1.2 Collector efficiency

The main parameter to describe the solar collector performance is the instantaneous efficiency η.

The collector efficiency is defined in steady-state conditions as:

$$\eta = \frac{\dot{Q}_{out}}{\dot{Q}_{in}} \tag{1.1}$$

where $\dot{Q}_{out}$ is the useful heat power (output) provided from the collector to the working fluid and $\dot{Q}_{in}$ is the input heat flux provided by the solar radiation.

The useful heat power $\dot{Q}_{out}$ is obtained as:

$$\dot{Q}_{out} = \dot{m} \cdot c_p \cdot (t_{out} - t_{in}) \tag{1.2}$$

where $\dot{m}$ is the mass flow rate flowing through the tube welded in the absorber element, t_{in} and t_{out} are the inlet and outlet fluid temperatures and c_p is the specific heat of the working fluid.

The input heat flux $\dot{Q}_{in}$ is defined as:

$$\dot{Q}_{in} = G \cdot A_c \tag{1.3}$$

where G is the global solar irradiance and A_c is the reference area of the collector.

To describe the collector efficiency is so necessary to define the reference area. Three kinds of area are defined for a solar thermal collector:

- the absorber area is the area of the absorber element;
- the aperture area is the area of the cover surface where the solar radiation enters the collector;
- the gross area is the total area occupied from a collector module.

In Figures 1.1, 1.2 and 1.3 are reported the reference areas in the most common solar thermal collector: flat-plate collector, evacuated tube collector with and without external reflector.

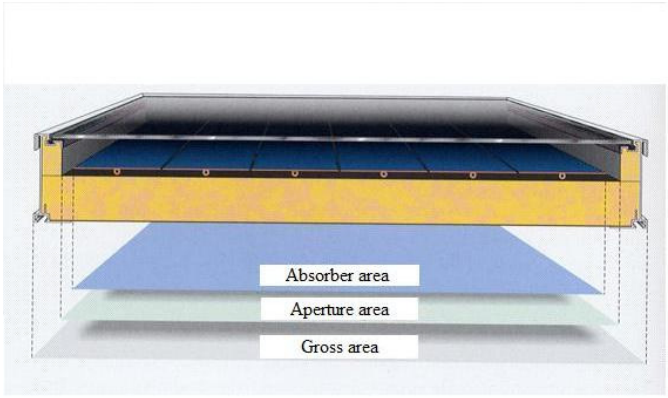

Figure 1.1. Reference areas for a flat-plate collector.

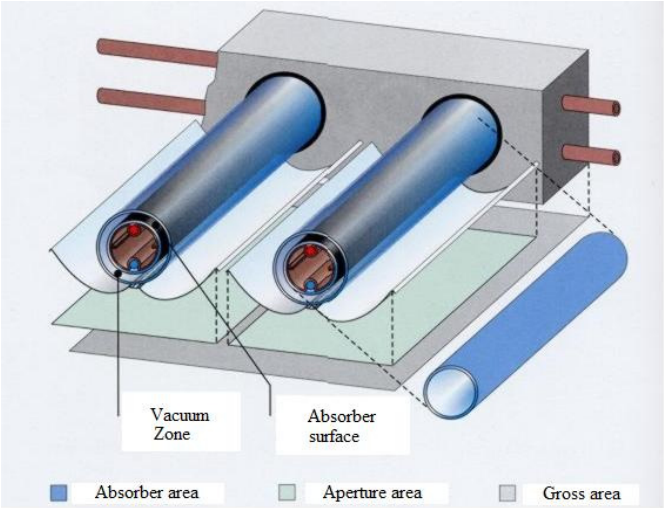

Figure 1.2. Reference areas for an evacuated tube collector with reflectors (CPC in this case).

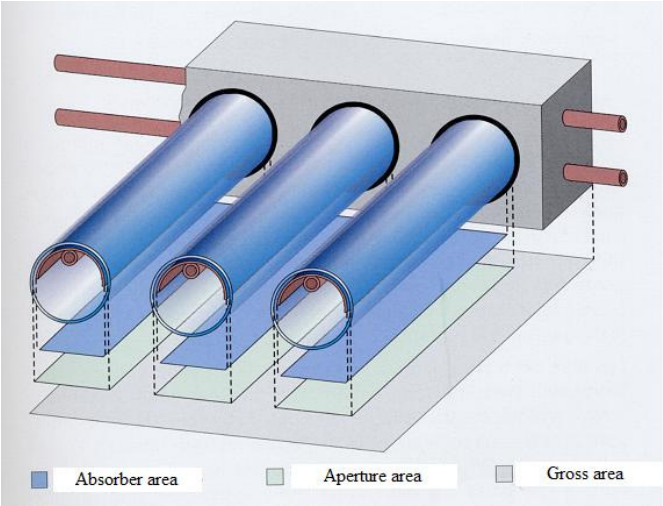

Figure 1.3. Reference areas for an evacuated tube collector without reflectors.

In following chapters the aperture area is taken as reference area.

1.3 Efficiency curve

The collector efficiency is a function of the external conditions and fluid temperature. Ad-hoc collector tests are performed to obtain the experimental efficiency curve.

The efficiency curve describes the trend of instantaneous collector efficiency varying the operating conditions. In EN 12975 (2006) for steady-state conditions and normal incidence angle of the direct radiation, it is described by the function:

$$\eta = \eta_0 - a_1 T_m^* - a_2 G (T_m^*)^2 \tag{1.4}$$

where η_0 is the optical efficiency, a_1 is the heat loss coefficient, a_2 is the temperature dependence of the heat loss coefficient, G is the global solar irradiance and T_m^* is the reduced temperature difference defined as:

$$T_m^* = \frac{\frac{t_{in} + t_{out}}{2} - t_a}{G} \tag{1.5}$$

where t_{in} and t_{out} are the inlet and outlet fluid temperature, t_a is the ambient air temperature and G is again the global solar irradiance.

In Figure 1.4 is shown an example of efficiency curve.

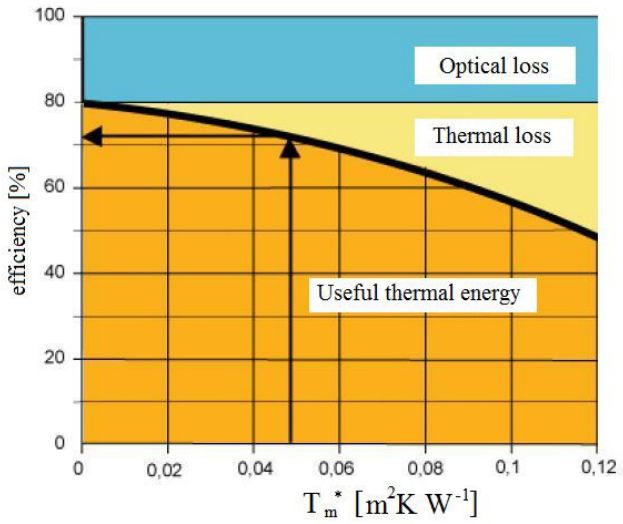

Figure 1.4. Collector efficiency curve and its meaning.

Another important parameter to describe the collector performance is the incidence angle modifier (IAM). It describes the efficiency at ambient operating temperature (optical efficiency) at different incidence angle, normalized to the value at normal incidence:

$$K_\theta(\theta) = \frac{(\tau\alpha)}{(\tau\alpha)_{en}} \tag{1.6}$$

where $(\tau\alpha)$ is the trasmittance-absorptance product for a general angle of incidence θ, that is directly linked with the optical efficiency, and $(\tau\alpha)_{en}$ is the same product at normal incidence conditions.

Chapter 2.
Experimental apparatus

2.1 Introduction

The experimental apparatus is described in the present chapter. The apparatus allows to perform measurements of solar collectors in agreement with the main guidelines of the standard EN 12975 (2006). Besides, it allows to acquire fifty thermocouples. In the work here presented these thermocouples have been used to measure local temperatures in a prototype collector, in order to obtain information on the local heat transfer between different components of the collector.

2.2 Test apparatus

The experimental apparatus is located on the terrace roof of the Dipartimento di Fisica Tecnica of the University of Padova (Del Col and Padovan, 2007). The apparatus has been set up to allow measurements of solar collector efficiency in agreement with the main guidelines of the standard EN 12975 (2006).

A schematic view of the test loop is reported in Figure 2.1.

Three collectors could be installed in the test apparatus. The hydraulic loop is divided in two independent lines.

Two pumps are used to circulate the liquid. Before entering the collectors, the fluid temperature is controlled in the storage 2, where four electrical heaters are located. Each heater has an electrical power of 5 kW. A control system, connected to a temperature sensor inserted in the storage, acts on these heaters to ensure an accurate control of the liquid temperature at the inlet of the collectors. The liquid temperature at the inlet and at the outlet of the collectors is measured by RTDs (platinum resistance thermometers), in the two hydraulic lines. The fluid, coming from the installed collectors, enters the storage 1 and then goes to a plate heat exchanger which works as a heat sink. In the plate

heat exchanger the heat flow rate provided by the solar radiation and by the electrical heaters is taken away by a secondary fluid, which is a mixture of water and propylene glycol. The heat flow rate is wasted in a second plate heat exchanger by the ground water of the building central plant. The ground water temperature in inlet of the second plate heat exchanger is constant (about 16°C); it's closed to the ground temperature.

A Coriolis effect and a magnetic type flow meter are used to measure the fluid flow rate in hydraulic lines. The second instrument measures a volumetric flow rate, thus the density of the fluid must be known. For the calibration of the test rig, the two flow meters can be connected in series: this allows checking the measurements obtained by the magnetic flow meter using the more accurate Coriolis effect sensor.

In Figure 2.2 is shown the instrumentation here described.

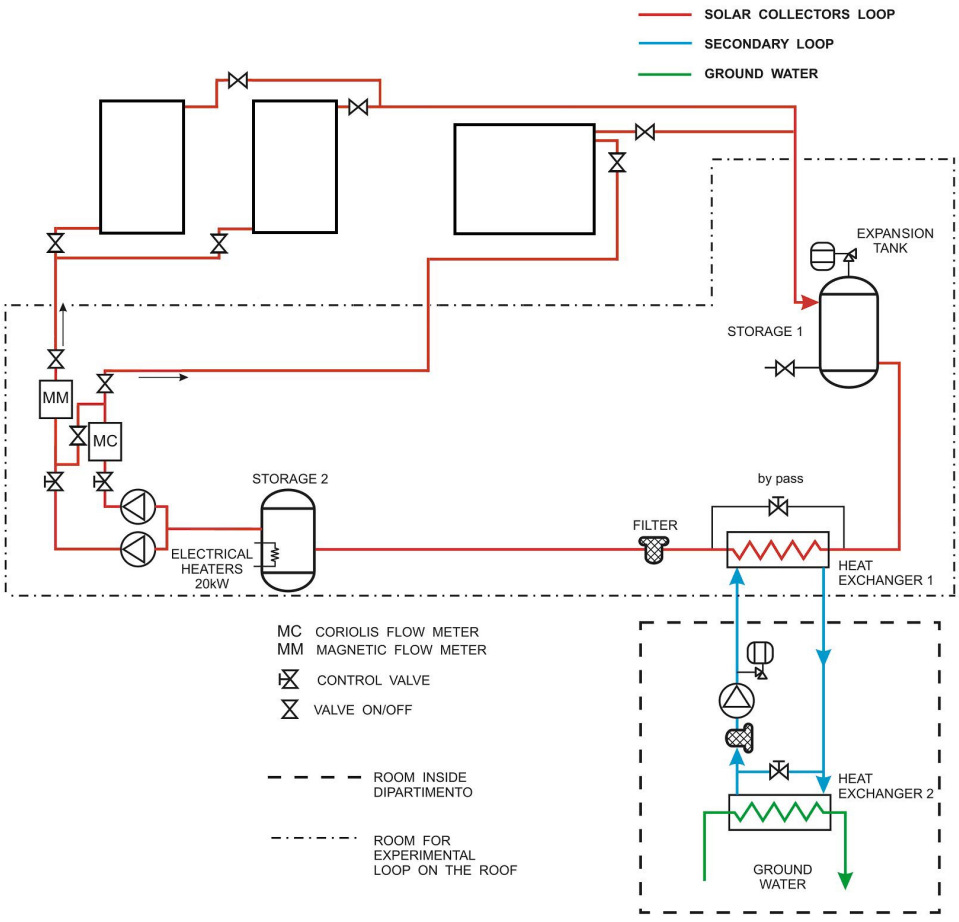

Figure 2.1. Schematic view of the experimental test rig.

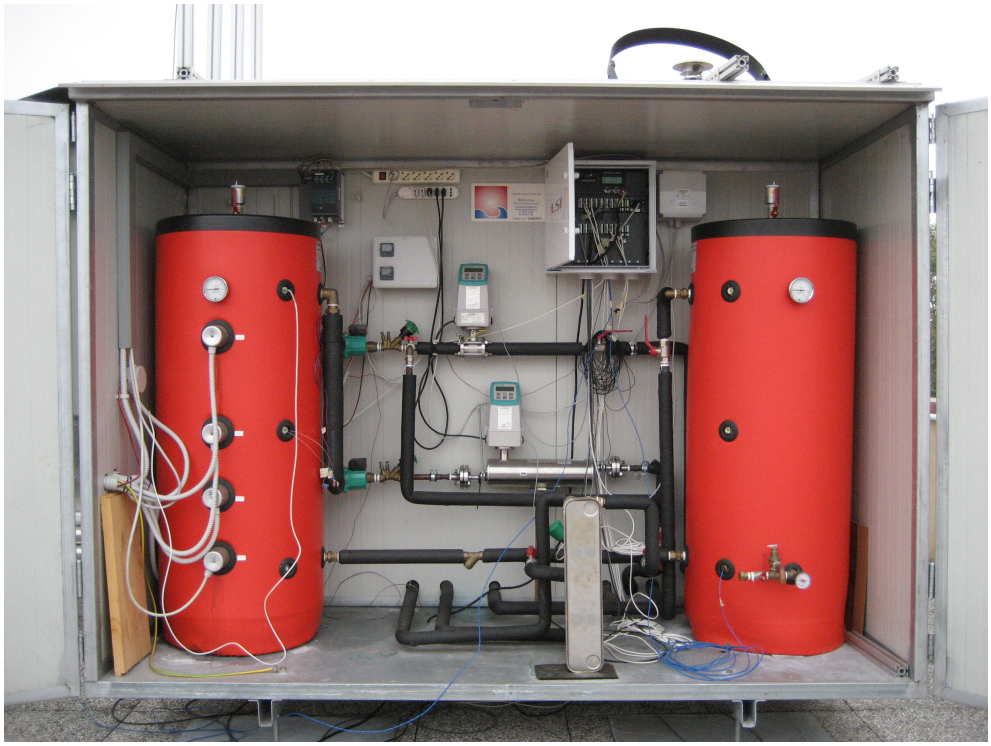

Figure 2.2. Hydraulic loop: Storages, pumps, fluid flow meters and plate heat exchanger (heat sink).

Three all black thermopile based pyranometers are used to measure the solar irradiance. A Kipp & Zonen pyranometer, classified as secondary standard by the WMO (World Meteorological Organization), measures the global solar irradiance on the plane of the collectors. Other two measurements are taken on the horizontal plane: a first class pyranometer measures the global solar irradiance on the horizontal plane; the third pyranometer (first class classified), shaded against the direct solar radiation, measures only the diffuse component. These instruments are shown in Figure 2.3.

Measurements are possible on two collectors at the same time. The ambient temperature is measured by means of another RTD positioned near the collectors in a shaded position. Finally an anemometer measures the air speed, being a parameter that influences the heat losses of the collector. The data acquisition is implemented by an Agilent 34970A data logger and by a Babuc ABC for meteorogical acquisitions (i.e. wind velocity, diffuse irradiance and global irradiance on the horizontal plane).

Figure 2.3. Irradiance measurements and anemometer.

Furthermore the acquisition system makes it possible to acquire fifty thermocouples to measure punctual temperatures. These measurements are T-type thermocouples (copper-constantan junction) and they have been used to measure local temperatures in a prototype collector, in order to obtain information on the local heat transfer between components of the collector.

The thermocouples have been connected to a Kaye K170-50C ice point. It provides a reference junction held at 0°C, required using this type of measurements.

The voltage output from the ice point is read by the Agilent 34970A data logger. In Figure 2.4 are shown the ice point and the Agilent 34970A.

Figure 2.4. Ice point and Agilent 34970A data logger.

2.3 Calibration procedure

The instruments used in the system and the whole measurement chain were calibrated before the performance tests.

The errors verified during a measurement can be categorised as systematic errors (i.e. “type B” errors) and random errors (i.e. “type A” errors) according to ISO GUM (1995).

The calibration procedure, described in this section, interests only “type B” errors.

2.3.1 RTDs (platinum resistance thermometer) calibration

Six RTDs are used in the system. The Agilent 34970A data logger with the appropriate settings provides directly the RTD measurement as a temperature value.

The RTDs were calibrated in-situ, by comparing their values to the values given by a high-precision platinum resistance thermometer PT 100 (measurement accuracy 0.002 K).

Calibration was performed at different temperatures, ranging from 10°C up to 90°C and a single correction equation (2^{nd} order polynomial function) was used for all the instruments. The measurement uncertainty does not vary after the calibration procedure. It is reported in Table 2.1, where are also reported the standard deviation and the average deviation from the temperature given by the PT 100 after calibration.

Table 2.1. Standard deviation among the RTDs measurements, average error and uncertainties for the whole measurement chain after calibration.

Temperature [°C]	Average error [K]	Standard deviation [K]	Uncertainty band [K]
13.0	-0.02	0.01	0.08
26.7	0.01	0.02	0.09
33.9	0.02	0.01	0.09
49.0	-0.02	0.02	0.10
62.4	-0.01	0.01	0.10
72.9	-0.02	0.02	0.10
88.9	0.01	0.03	0.11

2.3.2 Verification of pyranometers

Three all black thermopile based pyranometers are used to measure different components of the solar irradiance during the test runs.

A Kipp & Zonen pyranometer, classified as secondary standard measures the solar irradiance on the plane of the collectors: it is acquired by Agilent 34970A data logger (pyranometer 1).

Other two first class pyranometers measures the global solar irradiance (pyranometer 2) and the diffuse component (pyranometer 3) on the horizontal plane: they are acquired by Babuc ABC data logger.

Verification was performed comparing the global solar irradiance measurements applying pyranometers in a horizontal plane in the same position during two different days. The comparisons of two first class pyranometers with the “secondary standard pyranometer 1” are reported in Figure 2.5 and 2.6 where the whole measurement chain uncertainties are reported considering both “type A” and “type B” uncertainty terms.

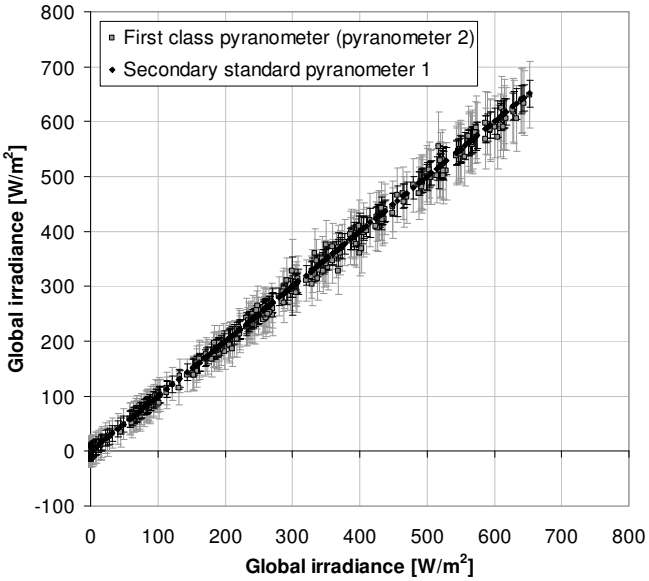

Figure 2.5. Comparison between first class pyranometer (pyranometer 2) and secondary standard pyranometer 1 measurements.

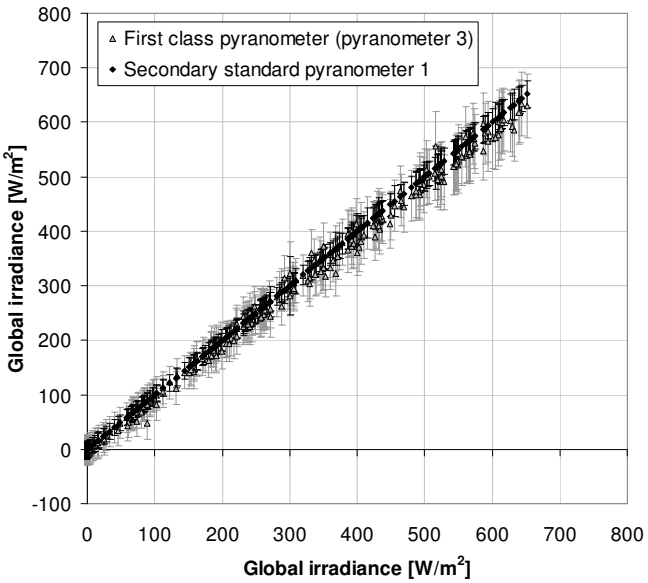

Figure 2.6. Comparison between first class pyranometer (pyranometer 3) and secondary standard pyranometer 1 measurements.

Another secondary standard pyranometer (pyranometer 4) was installed in the same way as other ones and it was acquired by means of Babuc ABC data logger, to compare the Agilent 34970A uncertainty term with the corresponding uncertainty related to the Babuc ABC. This comparison is shown in Figure 2.7 where the whole measurement chain uncertainties are reported considering both "type A" and "type B" uncertainty terms.

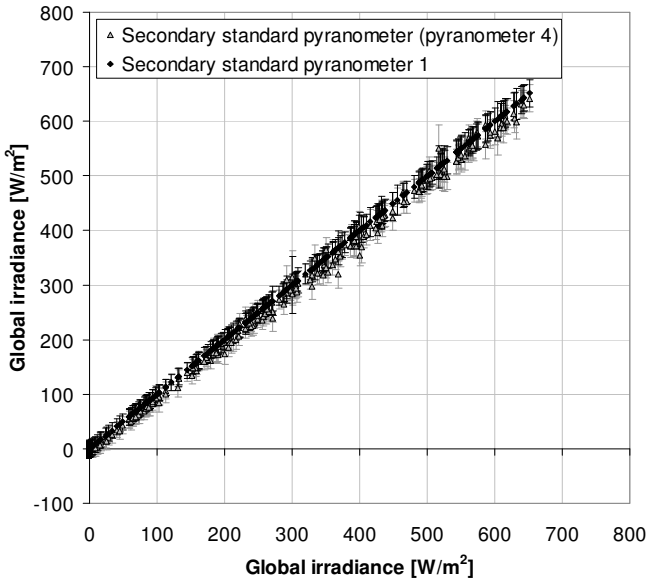

Figure 2.7. Comparison between secondary standard pyranometer (pyranometer 4) and secondary standard pyranometer 1 measurements.

From these diagrams it was concluded that the pyranometers are in agreement within their uncertainty ranges and the uncertainty term resulting from the use of the Agilent 34970A data logger is similar to the corresponding term obtained by the use of the Babuc ABC for pyranometer acquisitions.

2.3.3 Fluid flow meter calibration

A Coriolis effect and a magnetic type flow meter are used to measure the fluid flow rate in two separated hydraulic lines. For the calibration of the test rig, the two flow meters can be connected in series: this allows checking the measurements obtained by the magnetic flow meter using the more accurate Coriolis effect sensor. They both have a display and are acquired by means of Agilent 34970A data logger.

Calibration was performed at four different temperatures, ranging from 17°C up to 77°C, and at four different fluid flow rates ranging from 100 kg/h up to 400 kg/h.

The magnetic type instrument measures a volumetric flow rate, thus the density and so the temperature of the fluid must be known. The working fluid was water and a RTD was used to measure the fluid temperature in the line of instruments.

The mass flow rate obtained by the magnetic type flow meter was compared with the mass flow rate read in the display of the coriolis flow meter (without data logger uncertainty terms).

A single linear equation was used for the volumetric flow rate without temperature correction terms.

In Figure 2.8 is reported the difference between magnetic and coriolis instrument measurements and their uncertainties: the reference values are the coriolis measurements (provided by the display). The figure shows that the instrument measurements are in agreement within their uncertainty ranges after the calibration procedure

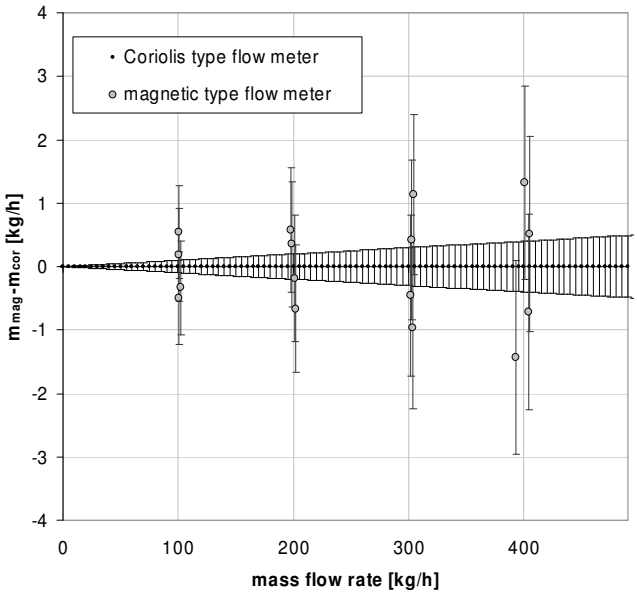

Figure 2.8. Difference between magnetic and coriolis measurements and their uncertainties after calibration.

2.3.4 Thermocouples calibration

Thermocouples were applied to the prototype collector to measure punctual temperatures. Being the calibration in-situ impossible, this procedure was made before thermocouples were welded to the solar collector.

The equation given in Nicholas and White (1994) was used for the voltage temperature characteristic of T-type thermocouples. Thermocouples have been then calibrated, by comparing the measure given by the thermocouple to the measure given by a platinum resistance thermometer PT 100. Calibration was performed at different temperature level, from 20°C up to 75°C and a single voltage-temperature correction (2^{nd} order polynomial function) was used for all the thermocouples.

The average deviation from the temperature provided by the platinum resistance thermometer and the standard deviation among the measurements given by the thermocouples after the calibration procedure are reported in Table 2.2.

After their application to the collector the thermocouple measurements were verified in-situ, without solar radiation with inlet fluid temperature equal to the ambient air temperature: condition without heat transfer between absorber plate, ambient air and working fluid.

The "type B" measurement uncertainty for the whole measurement chain was considered ±0.15 K with 95% confidence level.

Table 2.2. Standard deviation among the thermocouples measurements and average error after calibration.

Temperature [°C]	Average error [K]	Standard deviation [K]
19.7	0.01	0.03
34.6	-0.01	0.02
49.5	0.02	0.04
64.3	0.01	0.05
73.5	0.02	0.06

Chapter 3.
Collector comparison and daily efficiency

3.1 Introduction

Mainly two types of liquid solar collectors for domestic heating and hot water production are used presently: glazed flat-plate collectors and evacuated tube collectors. They are characterized by different cost and performance, so it is very important to choose the right collector for each application in order to optimize the behaviour of the whole system, the energy savings and the finance payback.

Glazed flat-plate collectors (FPC) usually present a metal absorber in a flat rectangular housing. The glass cover on the upper surface and the insulation on the other side limit the thermal losses. The solar energy absorbed by the plate is transferred to the liquid flowing within the collector tubes. The tubes are in good thermal contact with the absorber surface. Air is present in the space between the plate absorber and the transparent cover.

In comparison, evacuated tube collectors (ETC) allow to reduce the convection and the conduction thermal losses. This collector consists of glass vacuum-sealed tubes; the absorber profile is located into the inner glass tube and it can have several shapes.

The evacuated tube collectors may be subdivided in two types. In the direct flow through collector the heat transfer liquid is pumped in the tubes. The second type consists of heat pipes inside vacuum sealed glass tubes. A reflector can be present to optimize the absorption of the solar radiation.

The choice of the optimal collector depends on the temperature level required by the specific application and on the climatic conditions of the site of installation. Therefore, in terms of efficiency, each collector displays features which make it most suitable to a certain application.

In conventional uses solar collectors can provide energy for domestic hot water or space heating in combination with low water temperature systems (approximately 35-50°C), whereas this heat has to be provided above a minimum temperature of 75-80°C

in absorption cooling machines (Schmid et al., 1984). In areas with high sunshine, solar collectors could also be used in cooking process (Hussein et al., 2008) or in still plants (Badran, 2005).

The knowledge of the thermal performance of a solar collector is essential to make the right choice. With the publications of the European Standard EN 12975 (2006), a unique standard exists throughout Europe for solar thermal collector testing. This standard specifies a reproducible procedure and guarantees thus comparable results. It includes two alternative test methods for the thermal performance characterization of solar collectors: steady-state and quasi-dynamic tests.

Sets of results deriving from the steady-state and quasi-dynamic test methods should be fully comparable between them and allow to draw efficiency curves. However these efficiency curves do not necessarily represent the usual operating conditions and do not describe the global performance of the collector for the entire day.

Long-term performance predictions would allow the comparison between different collectors in several conditions. These predictions are provided by softwares using the parameters obtained from the tests. It is also possible to predict the short-term thermal performance of a solar energy collector under transient operating conditions by means of the overall response function (Prapas et al., 1988), provided that ad-hoc measurements are performed.

In this chapter a new set of data are presented: both flat-plate and evacuated tube collectors are tested simultaneously. For this purpose, steady-state and quasi-dynamic efficiency tests following the standard EN 12975 (2006) have been performed.

Extensive data have also been collected in dynamic conditions to evaluate the performance of the collectors in the whole day (daily tests), at various conditions: the experimental results have been reported in the so called input/output diagrams, where the daily useful collected energy is plotted against the daily solar irradiation.

This approach allows a more comprehensive comparison of the effective performance of the two types of solar thermal collectors considered here.

Experimental data taken in the entire day are also used to determine a daily efficiency for both type of collectors. Collector efficiency is a single parameter that combines collector and system characteristics, therefore its values must be carefully handled. The definition of a daily mean efficiency, as compared to steady-state efficiency, allows to enlighten and to quantify the advantage or disadvantage of different collectors provided that the test conditions are clearly defined on a bounded test variable space. This work has been also described in Zambolin and Del Col (2010) and Zambolin et al. (2009).

3.2 Test collectors

The experimental apparatus is described in Chapter 2. Two types of collectors are installed: evacuated tube collector (ETC) and standard glazed flat-plate collector (FPC).

The FPC system is made of two collectors with connected hydraulic header tubes. The size of the collectors is typical for domestic hot water applications in northern Italy.

Flat-plate collectors are connected in parallel. Each collector has a copper absorber plate, covered by a selective coating, with 10 parallel cooper tubes. The tubes are welded to the absorber plate with ultrasonic welding.

The evacuated tube collector is a direct flow type composed by 21 tubular glasses, with cylindrical aluminium profiles inside the glass tubes to contact the selective glass surface to the U-tube flow channel. In the back side of the glass tubes are located external CPC (compound parabolic concentrator) reflectors.

These two different collector geometries are described with their advantages and disadvantages in Kalogirou (2004).

Figure 3.1 shows a picture of the collectors. In Tables 3.1 and 3.2 some characteristics of the collectors installed are reported (the flat plate collectors area is the total area of the two collectors).

The tests have been performed using a mixture of water and propylene glycol as working fluid to prevent freezing during the winter season.

Figure 3.1. Collectors installed in the test apparatus and tested.

Table 3.1. Characteristics of the flat-plate collectors (FPC) installed in the test rig.

Gross area (two collectors)	5.16 m^2
Aperture area (two collectors)	4.76 m^2
Absorber plate material	Copper
Thermal insulation material	Glass wool + mineral wool
Selective coating	Tinox
Internal fluid volume(two collectors)	5.0 L

Table 3.2. Characteristics of the evacuated tube collector (ETC) installed in the test rig.

Gross area	3.9 m^2
Aperture area	3.5 m^2
Absorber plate material	glass
Thermal insulation material	vacuum + mineral wool
Selective coating	Aluminium nitrate
Internal fluid volume	3.2 L

3.3 Efficiency in steady-state conditions

During steady-state operating conditions, the useful output power of a solar collector for near normal incidence angle of the solar radiation can be written as reported in Duffie and Beckman (2006):

$$\dot{Q}_{out} = F' \cdot A_a \cdot \left[(\tau\alpha)_{en} \cdot G - U_c \cdot (t_m - t_a) \right] \tag{3.1}$$

where $\dot{Q}_{out}$ is the useful output power transmitted to the liquid, F' the collector efficiency factor, A_a the aperture area of collector, $(\tau\alpha)_{en}$ the effective trasmittance-absorptance product at normal incidence, G the global solar irradiance, U_c the overall heat loss coefficient and $(t_m - t_a)$ the difference between the average fluid temperature of the collector t_m and the ambient air t_a.

The efficiency is equal to:

$$\frac{\dot{Q}_{out}}{G \cdot A_a} = F' \cdot \left[(\tau\alpha)_{en} - U_c \cdot \frac{(t_m - t_a)}{G} \right] \tag{3.2}$$

and thus:

$$\eta = F' \cdot \left[(\tau\alpha)_{en} - U_c \cdot T_m^* \right] \tag{3.3}$$

where T_m^* is the reduced temperature difference.

If the heat loss coefficient is considered as the sum of two terms, a constant factor and a second term dependent on the temperature difference between fluid and ambient air $(t_m - t_a)$, the efficiency equation can be written as in Eq. (1.4):

$$\eta = \eta_0 - a_1 T_m^* - a_2 G (T_m^*)^2 \tag{3.4}$$

This form is in agreement with that provided by the standard EN 12975 (2006) for steady-state tests.

If the a_2 coefficient is assumed to be without statistical significance, a first order equation is obtained, Eq. (3.5), which means that the overall heat loss is a linear function of the temperature difference between fluid and ambient air.

$$\eta = \eta_0 - a T_m^* \tag{3.5}$$

In the case of steady-state tests, only high irradiance levels and thus low diffuse fractions are accepted by the standard. Therefore very stable and sunny weather conditions are needed.

The test runs have been performed in agreement with the guidelines of the standard EN 12975 (2006), apart from the measurement of the wind speed. The following measurements have been acquired: global irradiance on the collector plane, inlet and outlet fluid temperature in the collectors, surrounding air temperature and fluid flow rate. The surrounding air speed has been measured on the side of the test rig, the values are pretty constant, between 0.7 and 1.3 m/s. In the present data, the effect of the wind speed is reduced as compared to the test requirements given by the standard and therefore the present results are comparable to the condition of negligible surrounding air speed.

Each experimental point is obtained by setting a constant liquid flow rate and a constant fluid temperature at the inlet of the collectors.

A collector is considered to operate in steady-state conditions if the deviation of the experimental parameters is within the range indicated in Table 3.3. The test period includes a pre-conditioning period of at least 15 minutes, followed by measurement periods of 10 minutes.

Table 3.3. Test conditions and permitted deviations for steady-state tests according to EN 12975 (2006).

Parameter	Value	Deviation from the mean
Global radiation G [W/m^2]	> 700	± 50
Diffuse fraction G_d/G [%]	< 30	
Incidence angle beam irradiance [°]	< 20	
Inlet fluid temperature [°C]		± 0.1
Surrounding air temperature [°C]		± 1.5
Mass flow rate [%]		± 1
Surrounding air speed [m/s]	2÷4	

This procedure has been repeated varying the inlet fluid temperature and finally the results are reported in diagrams plotting the efficiency against the reduced temperature difference.

The curve parameters has been obtained by multiple linear regression (MLR), following the procedure reported in the standard EN 12975 (2006) and discussed in Kratzenberg et al. (2006), Sabatelli et al. (2002) and Mathioulakis et al. (1999), by developing a process in Matlab environment. This procedure is described in Annex A.

Experimental measurements for steady-state tests for both types of collectors are reported in Figure 3.2, where the second order curves obtained with the MLR method are also drawn.

For each point in Figure 3.2 the experimental uncertainties of the measured efficiency and of the reduced temperature difference (95% confidence interval) are reported, as calculated following the instructions provided in ISO GUM (1996) and described in Kratzenberg, et al. (2006) for the measured efficiency.

From the comparison between these curves, obtained for a global irradiance G = 1000 W/m^2, it can be observed that the efficiency of the flat-plate collector is higher in the case of low values of reduced temperature difference; the opposite occurs when the reduced temperature is higher than 0.037 m^{2}K/W. This is an expected result for commercial flat-plate and evacuated tube collectors: the efficiency of FPC is higher because of the better value of zero loss efficiency; when increasing the reduced temperature difference, the FPC efficiency is penalised by the higher heat loss coefficient.

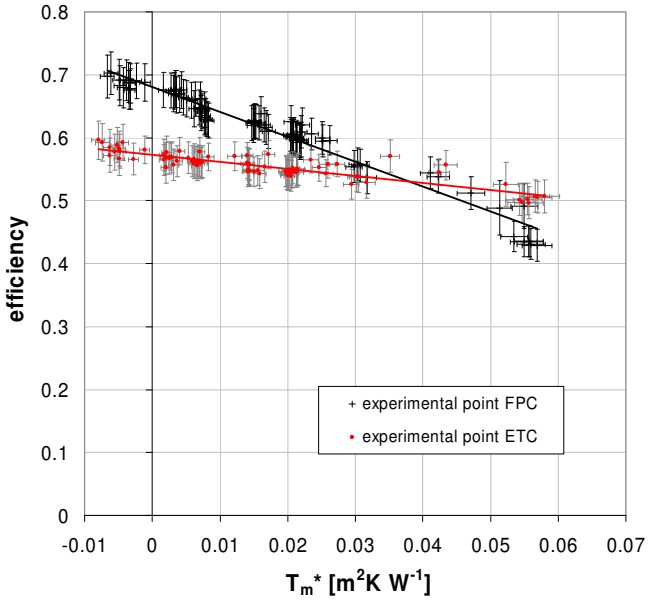

Figure 3.2. Efficiency curves at G = 1000 W/m^2 and normal incidence angle of the solar direct radiation: experimental points are reported for evacuated and flat-plate collectors obtained in steady-state conditions.

Assuming a solar irradiance of 1000 W/m^2 and an ambient air temperature of 20°C, the cross over point is obtained at an average liquid temperature t_m=57°C; if the solar irradiance is 700 W/m^2, the cross over point increases from 0.037 to 0.038 m^{2}K/W which means, at the same ambient air temperature, the average liquid temperature t_m decreases to 46.6°C.

3.4 Test in quasi-dynamic conditions

An alternative test method for the thermal performance characterisation of solar collectors is the quasi-dynamic method; it allows to achieve comparable results of the steady-state method even at less stable meteorological and operating conditions.

The following is the basic equation for the energy balance of the solar thermal collectors, as reported in the European Standard EN 12975 (2006) for the quasi-dynamic method:

$$\frac{\dot{Q}_{out}}{A_a} = F' \cdot (\tau\alpha)_{en} \cdot K_{\theta b} \cdot (\theta) \cdot G_b + F' \cdot (\tau\alpha)_{en} \cdot K_{\theta d} \cdot G_d - c_6 \cdot u \cdot G +$$
$$- c_1 \cdot (t_m - t_a) - c_2 \cdot (t_m - t_a)^2 - c_3 \cdot u \cdot (t_m - t_a) + c_4 \cdot \left(E_L - \sigma \cdot T_a^{\,4}\right) - c_5 \cdot dT_m / d\tau \qquad (3.6)$$

where the coefficients c_i are constant parameters used for the characterization of a solar collector.

In the quasi-dynamic approach the optical efficiency term is divided into two parts: the zero loss efficiency for beam radiation $F' \cdot (\tau\alpha)_{en} \cdot K_{\theta b}(\theta) \cdot G_b$ and the one for diffuse radiation $F' \cdot (\tau\alpha)_{en} \cdot K_{\theta d} \cdot G_d$.

The wind-dependence is modelled by two correction terms: one term gives the dependence in the zero loss efficiency $c_6 \cdot u \cdot G$, while the term $c_3 \cdot u \cdot (t_m - t_a)$ gives the wind influence of heat losses.

In this model the long-wave ''thermal'' irradiance dependence of the heat losses is given by $c_4 \cdot \left(E_L - \sigma T_a^{\,4}\right)$ and the effective thermal collector capacitance term is expressed as $c_5 \cdot dT_m / d\tau$.

The coefficients c_6, c_3 and c_4 can be assumed to be without statistical significance for covered solar collectors (EN 12975, 2006), where the wind and the long-wave irradiance losses are neglected; thus the c_1 and c_2 terms are equivalent to a_1 and a_2 in Eq. (3.4) Furthermore, as previously stated, the present data are characterized by negligible surrounding air speed.

3.4.1 Incidence angle modifiers

For flat-plate collectors with flat covers, the angular dependence of the incidence angular modifier for direct solar radiation is given by:

$$K_{\theta b}(\theta) = 1 + b_0 \cdot \left(\frac{1}{\cos(\theta)} - 1 \right) \qquad (3.7)$$

where b_0 is the incidence angle modifier coefficient (Duffie and Beckman, 2006) (negative value) and θ is the angle of incidence between direct solar beam and normal to the collector plane. Eq. (3.7) is used to expand the first term in the collector model expression described in Eq. (3.6).

For evacuated tube collectors the incidence angle dependence can be much more complicated and $K_{\theta b}$ is not merely dependent on the global angle θ. In fact, the incident beam must be split in two dimensions and the modifier can be described as $K_{\theta b}(\theta_t, \theta_l)$, where θ_t and θ_l are the transverse and longitudinal projection of incidence angle θ, respectively, as reported in Figure 3.3.

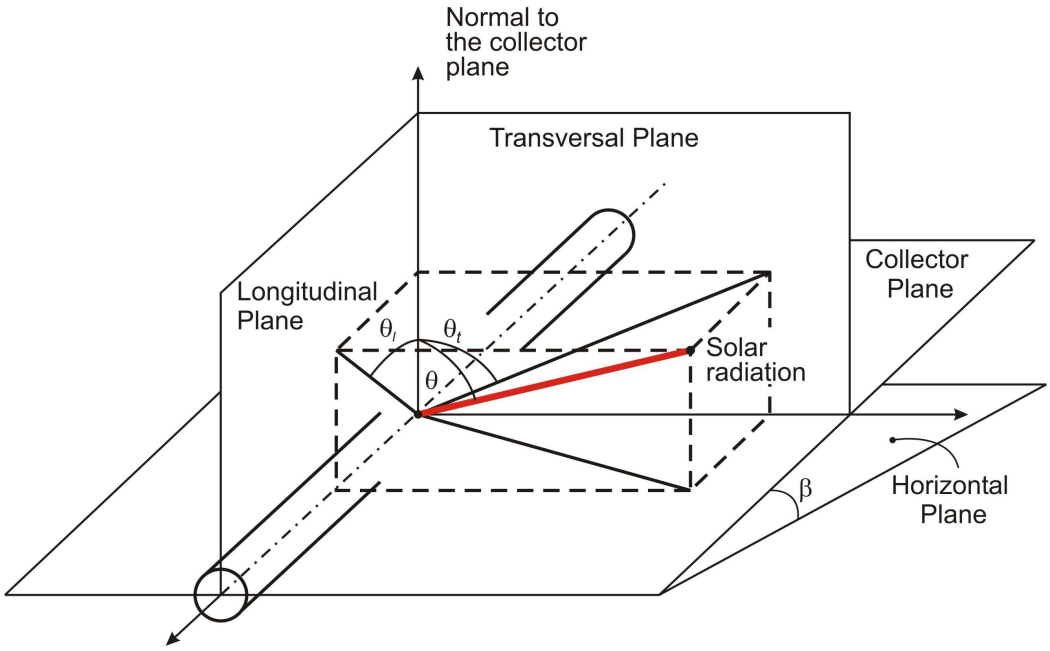

Figure 3.3. Reference geometrical parameters in the tubular collector.

For this type of collectors, McIntire and Reed (1983) have been suggested that the incidence angle modifier can be approximated by the product of two separate incidence angle modifiers:

$$K_{\theta b}(\theta_t, \theta_l) = K_{\theta t}(\theta_t, 0) \cdot K_{\theta l}(0, \theta_l) \tag{3.8}$$

For the computation of these parameters two methods are applicable using a stationary test installation: a routine described in EN 12975 (2006) based on a steady-state method, where the results are obtained in fixed conditions, and the so called extended multiple linear regression in the quasi-dynamic method, also described in EN 12975 (2006).

The extended MLR method, may determine the zero loss efficiency by applying it to small ranges of incidence angle (Rönnelid et al., 1997 and Perers, 1997). The disadvantage of the extended method is that several "sub regressions" must be performed instead of only one. Using the same experimental test data, this may increase the uncertainty of the results due to the lower number of data points in each "sub regression".

In this work an alternative method has been used; this method is described in Chapter 6.

Perers (1997) reports a diagram showing the incidence angle modifier versus the incidence angle for a number of different collector designs (including evacuated tube collectors); these results are not obtained with the standard b_0-function, but with the extended MLR. In Budihardjo and Morrison (2009) the transverse incidence angle modifier $K_{\theta t}$ of the water-in-glass evacuated tube collector is reported, which is obtained using experimental measurements and a simulation model.

The quasi-dynamic test method covers a wider range of test conditions as compared to the steady-state test method. In the present selected test data the global solar radiation G ranges between 150 W/m^2 and 1100 W/m^2, the diffuse solar radiation G_d between 33 W/m^2 and 379 W/m^2, the temperature difference $(t_m - t_a)$ between -11 K and 62 K.

As a result, the incidence angle modifiers obtained from the tests are shown in Figure 3.4, where $K_{\theta l}$ and $K_{\theta t}$ are reported versus the incidence beam angle along with the values provided by the manufacturer. The manufacturer's values are reported for mere comparison. These curves are reported only in the range covered by the tests, where the modifiers have been experimentally validated. The longitudinal projection of incidence angle θ_l in the evacuated collector ranges between 0° and 44° while the transverse projection θ_t goes from 0° to 66° in the tests. It can be seen that $K_{\theta t}$ is higher than one for the whole range of angles in the tests. Comparable trends have been reported in Perers (1997) and in Budihardjo and Morrison (2009).

Since the collector tilt and azimuth angle are kept constant during test runs, the longitudinal angle has been varied in a narrow range and therefore the curve of $K_{\theta l}$ reported in Figure 3.4 is verified only for incidence angles between 0° and 44°, which corresponds to $cos(\theta)$ ranging between 1 and 0.72. The absolute value of b_0 obtained from these tests ($|b_0|$=0.03) is lower as compared to the usual value reported in the literature, which is about 0.1 (Budihardjo and Morrison, 2009), but this has a minor effect on the efficiency curve due to the limited range of θ_l (at θ_l=44° $K_{\theta l}$=0.985 from the tests, whereas for the same angle $K_{\theta l}$=0.961 when $|b_0|$=0.1).

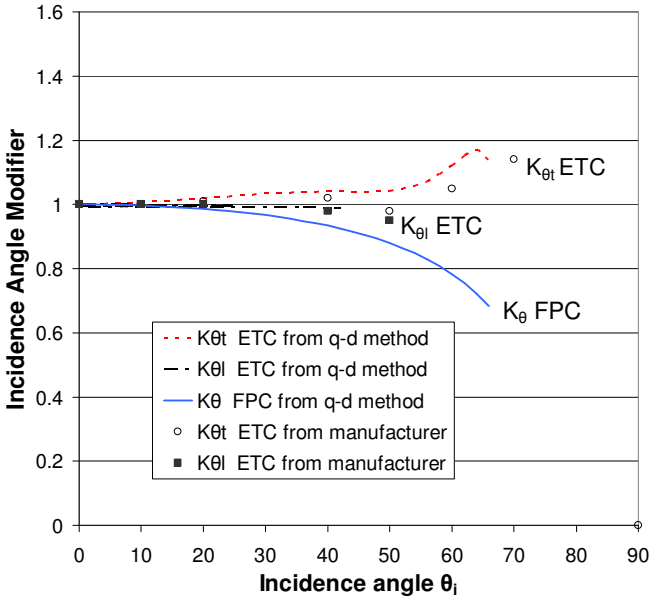

Figure 3.4. Incidence angle modifiers obtained from quasi-dynamic tests and values provided by the manufacturer. K_θ is the modifier of FPC as defined in Eq. (3.7) with $\theta_i = \theta$. $K_{\theta l}$ and $K_{\theta t}$ are the modifiers of ETC as defined in Chapter 6, with $\theta_i = \theta_l$ and $\theta_i = \theta_l$ respectively.

3.4.2 Efficiency curves

In according to the guidelines of the standard EN 12975 (2006), the following measurements have been performed during test runs: global irradiance on the collector plane, global and diffuse irradiance on the horizontal plane, inlet and outlet fluid temperature of the collector, surrounding air temperature and fluid flow rates. The incidence angles between direct beam and collector area are calculated for each time step (10 minutes) for both the FPC and ETC collectors as described in McIntire and Reed (1983).

The direct and the diffuse radiation on the tilted plane of the collector are calculated from the global radiation measurement on the collector plane and the diffuse radiation measured on the horizontal plane. With regard to the diffuse radiation, the pyranometer is equipped with a shading ring. A correction for the utilization of the shading band is calculated using the Drummond model (Drummond, 1956), to determine the effective diffuse radiation on the horizontal plane, and the Liu-Jordan method (Liu and Jordan, 1963) is then used for calculating the diffuse radiation on the tilted plane of the collector. The direct radiation on the tilted plane is obtained from the difference between global and diffuse radiation on the collector plane.

During each test run the fluid temperature at the inlet of the collectors and the fluid flow rate have been kept constant within about ± 1 K and ± 1 % respectively. The test

conditions and the permitted deviation of the measured parameters during quasi-dynamic tests are listed in Table 3.4.

Table 3.4. Test conditions and permitted deviations for the quasi-dynamic test procedure according to EN 12975 (2006).

Parameter	Value	Deviation from the mean
Global radiation G [W/m^2]	> 150 *	
Inlet fluid temperature [°C]		± 1
Outlet-Inlet fluid temperature	> 1	
Mass flow rate [%]		± 1
Surrounding air speed [m/s]	1 ÷ 4	

* It is the lower limit in the present tests; EN 12975 (2006) does not specify a lower limit for the global radiation

The test period includes a pre-conditioning period of at least 15 minutes; instantaneous readings are acquired with a time step of 10 seconds and are reduced to calculate characteristic mean values for each time interval equal to 10 minutes.

This procedure has been repeated in different days and for different inlet fluid temperatures; the tests have been performed simultaneously for flat-plate and evacuated tube collectors. The parameters of the efficiency curves and their regression uncertainties, determined from the steady-state and quasi-dynamic procedures for both the collector types, are listed in Table 3.5. In this table the uncertainties of the target parameters are obtained as the square root of the variances, determined as reported in the procedure described in Kratzenberg et al. (2006) in the case of the weighted least square (WLS) method, considering only the variance because all the collector coefficients are considered uncorrelated.

The parameter identification method applied to the quasi-dynamic model is described in Annex A.

Table 3.5. Collector coefficients obtained with quasi-dynamic and steady-state methods for both the collectors.

	Quasi-dynamic test ETC		Quasi-dynamic test FPC	
Parameter	**Value**	**Uncertainty**	**Value**	**Uncertainty**
$F'(\tau\alpha)_{en}$	0.560	0.007	0.682	0.005
b_0	-0.039	0.192	-0.217	0.022
$K_{\theta d}$	1.075	0.022	0.980	0.017
c_1 [W/(m^{2}K)]	0.978	0.184	3.407	0.187
c_2 [W/(m^{2}K^2)]	0.003	0.003	0.014	0.004
c_5 [J/(m^{2}K)]	24284	1028	12023	773
	Steady-state test ETC		**Steady-state test FPC**	
η_0	0.572	0.004	0.676	0.006
a_1 [W/(m^{2}K)]	0.995	0.445	3.059	0.565
a_2 [W/(m^{2}K^2)]	0.002	0.009	0.023	0.012

The efficiency curves, at G=1000 W/m^2 global irradiance, obtained by this test procedure for both the collector types, are reported in Figure 3.5: the uncertainty band (95% confidence interval) is also drawn for several T_m^* values. The uncertainty bands are the expanded uncertainties of the normalized efficiency curves as described in Kratzenberg et al (2006).

From the comparison between the curves obtained in steady-state and in quasi-dynamic conditions, reported in Figure 3.6 for the same irradiance conditions, it can be observed that the results obtained by these different procedures are fully compatible within their uncertainty ranges. Similar agreement between the two collector test procedures is also found in Kratzenberg et al. (2005), Rojas et al. (2008) and Cucumo et al. (2008) and for several flat-plate collectors in Fisher et al. (2004).

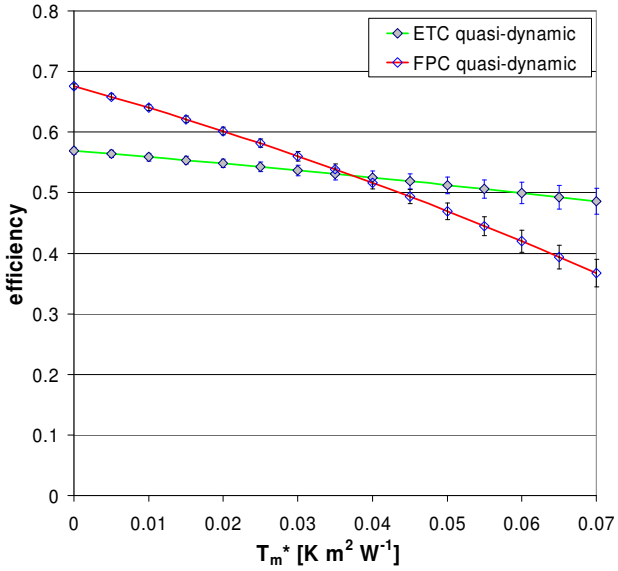

Figure 3.5. Efficiency curves of evacuated and flat-plate collectors obtained in quasi-dynamic conditions at G = 1000 W/m^2 and normal incidence angle of the solar direct radiation.

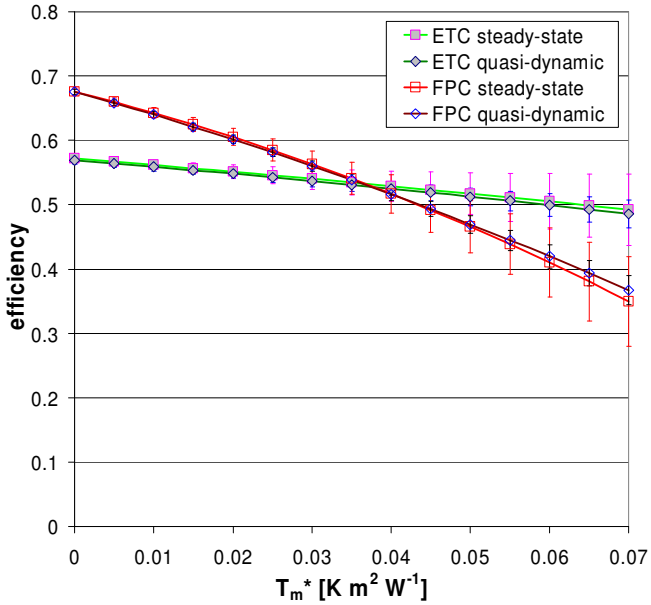

Figure 3.6. Compared efficiency curves in steady-state and quasi-dynamic conditions at G=1000 W/m^2 and normal incidence angle of the solar direct radiation.

3.5 Daily tests

Since optical characteristics and heat losses of these two collectors are very different from each other, the standard stationary efficiency (Sect. 3.3) is not sufficient to characterize the distinct behaviour of the collectors. The test in quasi-dynamic conditions (Sect. 3.4) provides a more comprehensive information on the collectors performance. As a further step, daily tests have been analyzed on these two collectors, at the same operating conditions. For the purpose of comparison, the two collectors have worked for the same period of the day, and with the same inlet temperature. This may lead to zero or even negative converted energy for some time: this is accepted here for the purpose of full characterization, although in practical applications collectors do not usually work when the heat losses exceed its absorbed solar energy.

For each day the test period ranges between 9:45 a.m. and 5:45 p.m. (legal time). Daily tests have been performed for several environment conditions and different days (sunny, variable, cloudy and rainy conditions): experimental data reported here were measured from July to October 2008 for 30° tilt angle of collectors.

Three different inlet temperatures (about 20, 43 and 73 °C) and fluid flow rates (17, 29 and 50 kg/(m^2h)) have been investigated.

Characteristic parameters are the incident solar energy in the collector area (input) and the output energy provided by the collectors over 10 minutes. The entire day is divided in n time intervals of 10 minutes: the total daily input and output energies are obtained as the sum of the input and the output energy quantities of each time interval. With the regard to the output energy, the negative terms are also considered in the sum; this case occurs when the fluid temperature at the outlet of the collector is lower than the inlet temperature, which means that thermal losses are larger than the heat produced by the absorber.

Figure 3.7 shows the main parameters recorded during a daily test run for a sunny day (July 16). Flow rate $\dot{m}$ is kept constant for the whole day. The inlet fluid temperature t_{in} of the liquid into collectors is the same for FPC and ETC. Inlet fluid temperature is roughly constant for the whole day: small variations depend on the ground water used to extract the heat from collectors. Irradiance G and ambient air temperature t_a are also reported.

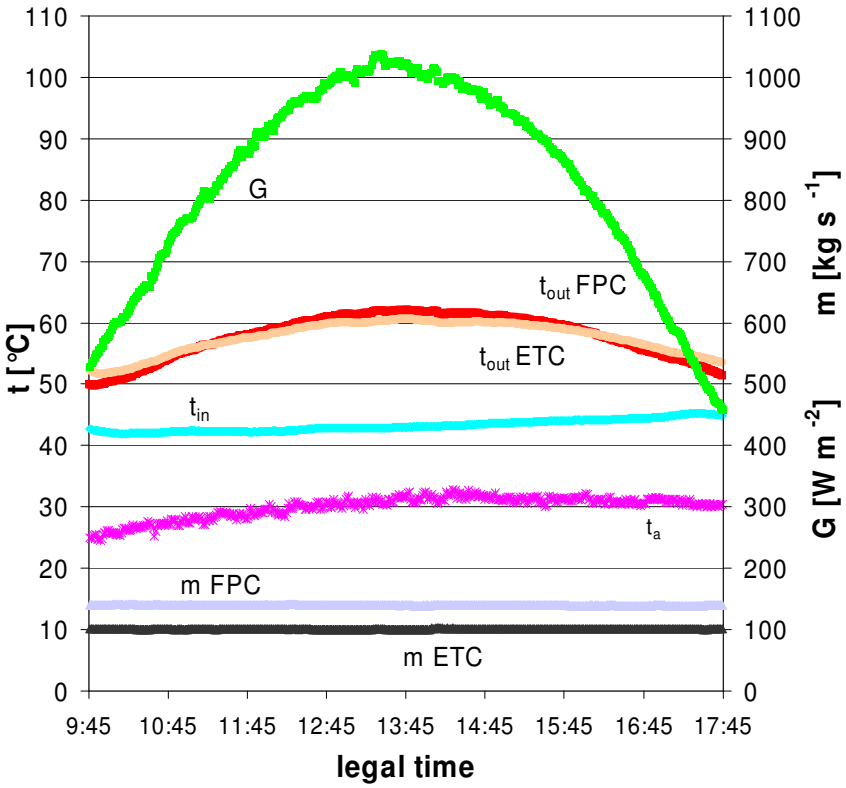

Figure 3.7. Measurements during a daily test (July 16, 2008): irradiance, inlet outlet and ambient temperatures, mass flow rate.

Outlet temperatures t_{out} vary as dependent on the irradiance conditions. It may be noticed that in the case of the day to which Figure 3.7 is referred, the outlet temperature of the flat-plate collector overcomes the one of the evacuated tube collector only in the central part of the day.

The collectors' performance for the same day can be seen in Figures 3.8 and 3.9, where the measured efficiency during the whole test day is reported for both the collector types at the same operating conditions (inlet liquid temperature, specific mass flow rate and ambient temperature). In this graphs the reduced temperature is also reported: this parameter has roughly the same value for both of the collector types.

By knowing the reduced temperature and the efficiency curves of the collectors (Figure 3.2) one can calculate the efficiency assuming that the collectors operate constantly at steady-state standard conditions. The calculated values of steady-state efficiency are plotted in Figure 3.9 with empty symbols. In the case of ETC, the experimental and calculated efficiencies in Figure 3.9 display a similar trend for the entire day. For FPC, the experimental efficiency is penalized in the morning and evening

hours. In fact, in the daily tests, steady-state conditions requirements (Table 3.3) are not satisfied. In particular the solar radiation incidence angle varies with time. The effect of incidence angle on the collector performance is usually characterized by means of the parameter $K_{\theta b}$. In Figure 3.9, the difference between measured and modelled efficiency with steady-state model is mainly due to the effect of $K_{\theta b}$ in the early and the last hours of the day. In the case of FPC this parameter (Eq. (3.7)) is lower than unity if the beam is not perpendicular to the collector plane and therefore the efficiency decreases; on the contrary, for ETC this parameter remains approximately constant along the test period. This is clearly shown in Figure 3.4.

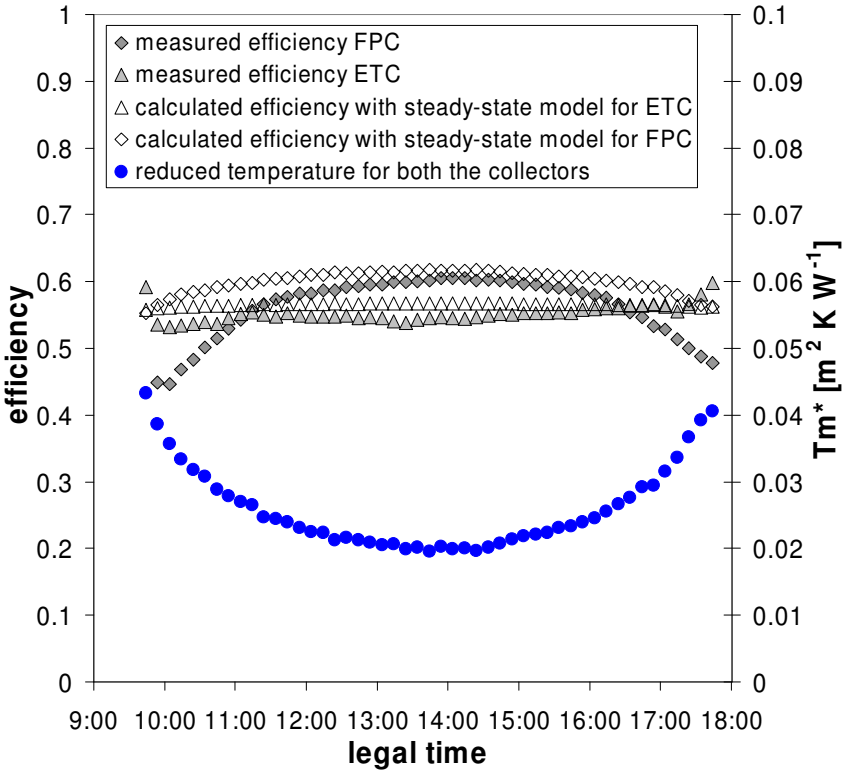

Figure 3.8. Comparison between experimental efficiency (solid symbols) and calculated efficiency (empty symbols) during an entire day (July 16, 2008). The calculated efficiency is obtained by means of steady-state model.

In Figure 3.9 the same experimental efficiencies are compared to the values computed by means of the quasi-dynamic model. As one would expect, measured and calculated values are in good agreement in this case.

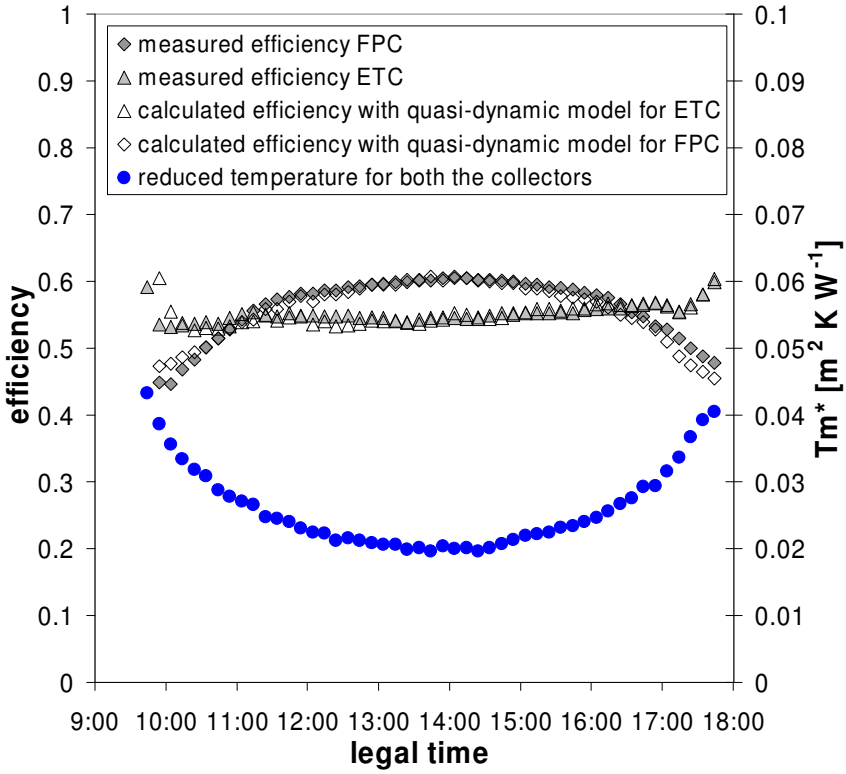

Figure 3.9. Comparison between experimental efficiency (solid symbols) and calculated efficiency (empty symbols) during an entire day (July 16, 2008). The calculated efficiency is obtained by means of quasi-dynamic model.

The results obtained in daily tests are plotted in the input/output diagrams, where the daily incident solar radiation on the collector (x-axis) is related to the daily useful energy collected (y-axis). An example of a similar procedure is described in Perers et al. (1984).

Figure 3.10 illustrates a typical input/output diagram where each energy value is referred to one daily test and to a collector area of 1 m^2. All the daily experimental points reported are collected for both collector types and are characterized by different inlet fluid temperature, mass flow rate and environmental conditions. One can see that the data scattering is larger for the flat-plate collector. This feature is clarified in Figures 3.11 and 3.12, where the data points are reported for the evacuated tube and flat-plate collectors, respectively, at constant flow rate of 29 kg/(m^2 h).The test conditions and the main outputs for these daily tests are reported in Table 3.6.

Experimental points with similar inlet fluid temperatures are grouped together and the regression curves drawn here show a linear trend.

The three lines in Figures 3.11 and 3.12 display a medium value of $\left(\overline{t}_m - \overline{t}_a\right)$ (defined in Sect. 3.6) equal to 0 K, 25 K and 50 K in the case of 20°C, 43°C and 73°C inlet temperature, respectively. It must be reminded here that the temperature difference between liquid and ambient changes during the daily tests and therefore the results of present experimental tests can be described by a quasi-dynamic model, as in Eq. (3.6).

The daily performances of the FPC and the ETC collectors operating in dynamic conditions are compared to each other in Figures 3.13, 3.14 and 3.15, at low, medium and high inlet temperature respectively. It can be seen that these interpolation lines have different slopes for ETC and FPC at the same inlet temperature of the liquid to the collector. This result will be discussed in the following section.

Only at low inlet temperature (Figure 3.13), the output energy of the FPC overcomes the one of ETC, because when increasing the fluid-to-ambient temperature difference this leads to larger heat losses and thus larger penalization of the FPC efficiency as compared to the ETC.

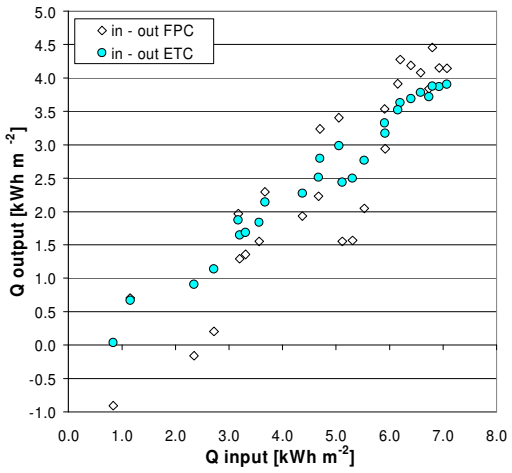

Figure 3.10. Experimental points in input-output diagram for both types of collectors

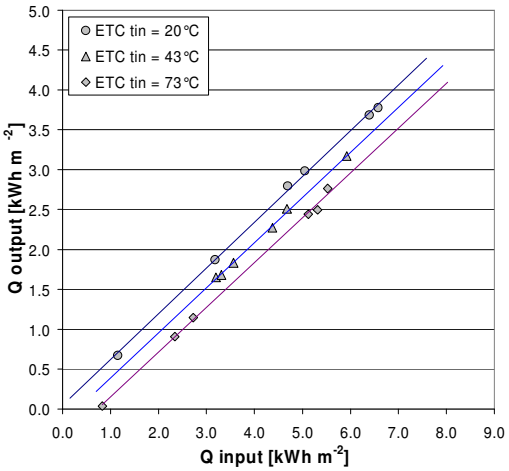

Figure 3.11. Input-output diagram for the daily energies converted by the ETC at three different operating temperatures and constant flow rate (t_{in} is inlet fluid temperature to the collector).

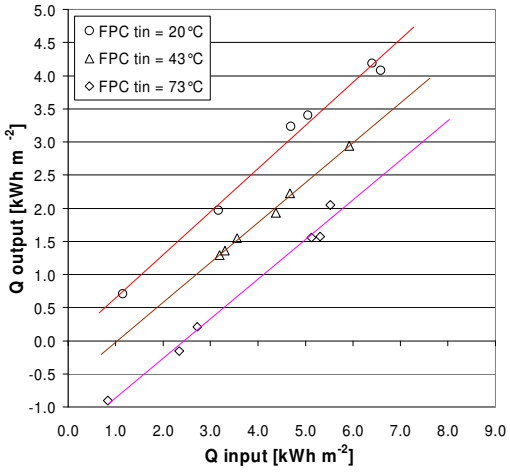

Figure 3.12. Input-output diagram for the daily energies converted by the FPC at three different operating temperatures and constant flow rate (t_{in} is inlet fluid temperature to the collector).

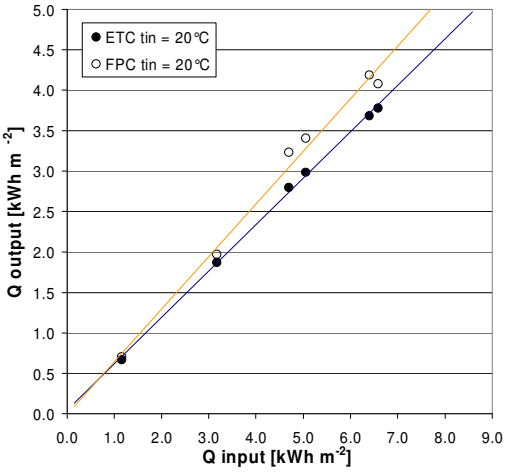

Figure 3.13. Comparison of the input-output curves of both collector types at low operating temperatures.

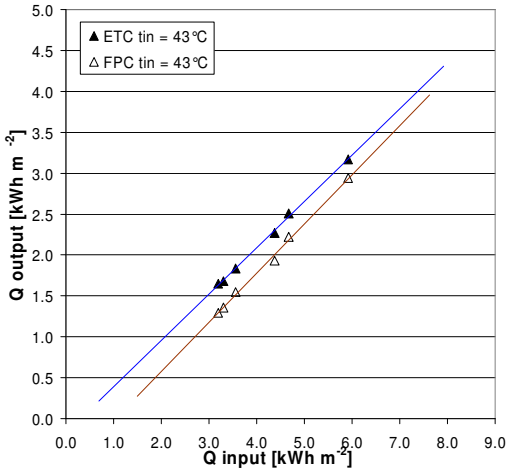

Figure 3.14. Comparison of the input-output curves of both collector types at medium operating temperatures.

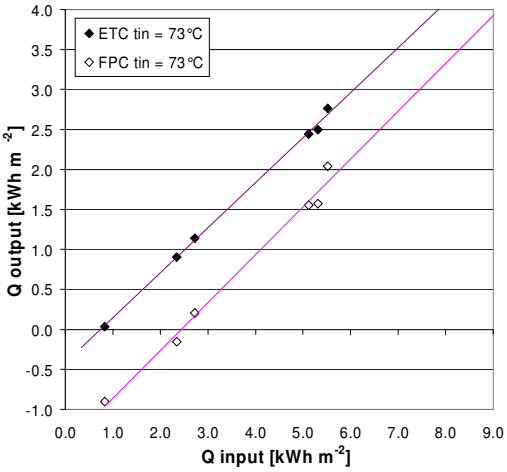

Figure 3.15. Comparison of the input-output curves of both collector types at high operating temperatures.

Table 3.6. Results obtained for daily tests reported in input/output diagrams.

FPC										ETC									
DATA	Q_{in} [kWh/m^2]	Q_{out} [kWh/m^2]	$\frac{\dot{m}}{A_a}$ [kg/(m^{2}h)]	$\overline{ti}$ [°C]	$\overline{tm}$ [°C]	$\overline{ta}$ [°C]	$\overline{tm}-\overline{ta}$ [K]	$\overline{\eta}$	$T_m{}^*{}_m$ [(m^{2}K)/W]	Q_{in} [kWh/m^2]	Q_{out} [kWh/m^2]	$\frac{\dot{m}}{A_a}$ [kg/(m^{2}h)]	$\overline{ti}$ [°C]	$\overline{tm}$ [°C]	$\overline{ta}$ [°C]	$\overline{tm}-\overline{ta}$ [K]	η	$T_m{}^*{}_m$ [(m^{2}K)/W]
10-Jul	4.70	3.23	29.7	18.9	25.1	30.2	-5.1	0.69	-0.009	4.70	2.80	28.8	18.9	24.4	30.2	-5.8	0.60	-0.010
11-Jul	6.40	4.19	29.5	27.0	35.0	31.9	3.1	0.65	0.004	6.40	3.68	28.9	27.1	34.2	31.9	2.3	0.58	0.003
11-Sep	5.05	3.41	29.6	19.7	26.3	31.1	-4.9	0.67	-0.008	5.05	2.98	28.9	19.8	25.6	31.1	-5.5	0.59	-0.009
15-Sep	3.17	1.97	29.6	19.9	23.7	18.5	5.2	0.62	0.013	3.17	1.87	29.1	20.0	23.7	18.5	5.2	0.59	0.013
16-Sep	6.58	4.08	29.6	19.9	27.7	21.9	5.8	0.62	0.007	6.58	3.78	29.0	19.9	27.3	21.9	5.4	0.57	0.007
28-Oct	1.16	0.70	29.5	17.7	19.1	16.4	2.6	0.61	0.018	1.16	0.67	29.2	17.7	19.1	16.4	2.6	0.58	0.018
16-Jul	6.74	3.84	29.4	43.2	50.5	30.0	20.5	0.57	0.024	6.74	3.72	28.9	43.2	50.4	30.0	20.4	0.55	0.024
17-Sep	4.68	2.23	29.2	42.6	46.9	20.5	26.4	0.48	0.045	4.68	2.51	29.1	42.6	47.4	20.5	26.9	0.54	0.046
18-Sep	3.20	1.29	29.2	42.9	45.4	19.0	26.4	0.40	0.066	3.20	1.65	29.0	43.0	46.1	19.0	27.1	0.52	0.068
22-Sep	5.92	2.94	29.2	43.0	48.7	20.1	28.6	0.50	0.039	5.92	3.17	29.1	43.0	49.1	20.1	29.0	0.54	0.039
09-Oct	3.56	1.55	29.1	43.8	46.8	21.8	25.0	0.44	0.056	3.56	1.84	29.1	43.7	47.3	21.8	25.5	0.52	0.057
20-Oct	4.38	1.93	29.1	42.9	46.6	19.0	27.6	0.44	0.050	4.38	2.27	29.1	42.9	47.3	19.0	28.2	0.52	0.052
22-Oct	3.31	1.36	29.1	42.1	44.7	19.7	25.0	0.41	0.060	3.31	1.68	29.1	42.0	45.3	19.7	25.6	0.51	0.062
10-Sep	5.52	2.04	29.2	73.9	77.8	30.6	47.2	0.37	0.068	5.52	2.77	28.7	73.7	79.0	30.6	48.4	0.50	0.070
26-Sep	2.72	0.21	28.9	71.1	71.5	18.6	52.9	0.08	0.156	2.72	1.14	29.1	70.9	73.0	18.6	54.5	0.42	0.160
28-Sep	5.31	1.57	28.6	72.6	75.6	19.1	56.4	0.30	0.085	5.31	2.50	29.1	72.5	77.3	19.1	58.1	0.47	0.088
30-Sep	2.34	-0.16	28.6	72.1	71.8	17.7	54.1	-0.07	0.185	2.34	0.91	29.1	71.9	73.7	17.7	56.0	0.39	0.191
10-Oct	5.12	1.56	28.6	72.1	75.1	22.9	52.2	0.30	0.082	5.12	2.44	29.1	72.0	76.6	23.0	53.6	0.48	0.084
16-Oct	0.83	-0.91	28.4	71.5	69.7	18.0	51.7	-1.09	0.496	0.83	0.04	28.8	71.3	71.4	18.1	53.3	0.04	0.512

3.6 Collector model for daily tests

An analytical expression for the daily energy extracted by the collector can be derived from Eq. (3.6).

The same assumptions described in Sect. 3.4 are possible; besides, the radiation term is not split into separated sub-models for the direct and diffuse radiation components as it happens in the quasi-dynamic collector model.

As a further simplification, the term $c_2 (t_m - t_a)^2$ is here set equal to zero: in the case of ETCs this assumption is verified because the T-ratio (as defined in EN 12975, 2006) is lower than 2 (T-ratio=1.88 in this case) and thus under EN 12975 (2006) criterion c_2 can be set equal to zero. In the case of FPCs such a criterion would not allow us to neglect c_2; however $(t_m - t_a)$ is kept within a limited value, around 55 K in the present tests and the product $c_2 (t_m - t_a)^2$ is neglected as a first approximation. This assumption is necessary to obtain at the end of the integration procedure an equation with only parameters immediately computable by daily data and will be later checked with reference to daily test data.

Finally the energy balance in the test period is described by the Eqs. (3.9) and (3.10):

$$\int_{n\cdot\Delta\tau} \frac{\dot{Q}_{out}}{A_a}\cdot d\tau = \int_{n\cdot\Delta\tau}\left[F'\cdot(\tau\alpha)\cdot G - c\cdot(t_m - t_a) - c_5\cdot\frac{dT_m}{d\tau}\right]\cdot d\tau \tag{3.9}$$

$$\int_{n\cdot\Delta\tau} \frac{\dot{Q}_{out}}{A_a}\cdot d\tau + \int_{n\cdot\Delta\tau} c_5\cdot dT_m = \int_{n\cdot\Delta\tau} F'\cdot(\tau\alpha)\cdot G\cdot d\tau - \int_{n\cdot\Delta\tau} c\cdot(t_m - t_a)\cdot d\tau \tag{3.10}$$

where the left-hand side is the output energy Q_{out}. This term is calculated by knowing the temperatures trend, the mass flow rate of the collector during the test period and the parameter c_5. The thermal capacitance, reported in Table 3.5 has been calculated from the quasi-dynamic methods: it does not have an important effect in the present tests, because the inlet temperature is constant during each daily test. For example the thermal capacitance contribution for the FPC in the test day reported in Figure 3.7 is lower than 6 Wh/m^2 which is only 0.2% of the daily heat production (3836 Wh/m^2).

Therefore:

$$Q_{out} = F'\cdot\overline{(\tau\alpha)}\cdot Q_{in} - \int_{n\cdot\Delta\tau} c\cdot(t_m - t_a)\cdot d\tau \tag{3.11}$$

where:

$$\overline{(\tau\alpha)} = \frac{\int_{n\cdot\Delta\tau} (\tau\alpha)\cdot G\cdot d\tau}{Q_{in}} \tag{3.12}$$

$\overline{(\tau\alpha)}$ is the average of $(\tau\alpha)$ defined in Eq. (3.12) and $n\cdot\Delta\tau$ is the test period duration.

$$Q_{out} = F'\cdot\overline{(\tau\alpha)}\cdot Q_{in} - c\cdot\left(\overline{t_m} - \overline{t_a}\right)\cdot n\cdot\Delta\tau \tag{3.13}$$

$\overline{t_m}$ and $\overline{t_a}$ are the average temperatures over the test period.

Eq. (3.13) provides an explanation of the experimental trends plotted in the input-output diagrams (from Figure 3.11 to Figure 3.15). In fact, according to the above equation, the output energy is a linear function of the input energy and also depends on the liquid to ambient temperature difference. The slope of the straight lines is due to the parameter $F'\cdot\overline{(\tau\alpha)}$ which is different for the two types of collectors. The flat-plate collector displays a higher slope as compared to the evacuated collector, which in turn is due to its higher value of $F'\cdot\overline{(\tau\alpha)}$.

For a given collector, the slope of the input/output energy curves does not vary with the inlet liquid temperature to the collector (see Figures 3.11 and 3.12).

From Eq. (3.13) it is also possible to obtain an expression of the average collector efficiency during the test period, in agreement with the results obtained by Perers et al (1984b). This equation can be written similarly as in Eq. (3.5) for steady-state conditions:

$$\frac{Q_{out}}{Q_{in}} = F'\cdot\overline{(\tau\alpha)} - c\cdot\frac{\left(\overline{t_m} - \overline{t_a}\right)}{\frac{Q_{in}}{n\cdot\Delta\tau}} \tag{3.14}$$

$$\overline{\eta} = \overline{\eta_0} - c\cdot T_m^{*}{}_m \tag{3.15}$$

where $\overline{\eta}$ is the average daily efficiency, $\overline{\eta_0}$ is the zero-loss average efficiency and $T_m^{*}{}_m$ is the average reduced temperature computable only by the knowledge of $\overline{t_m}$, $\overline{t_a}$ and Q_{in}.

Therefore, using all the experimental points reported in the input/output diagrams (Figure 3.10) the daily efficiency has been calculated. In Figure 3.16 the daily efficiency is plotted against the daily average reduced temperature $T_m^{*}{}_m$; the experimental data and the curves fitting the points are reported.

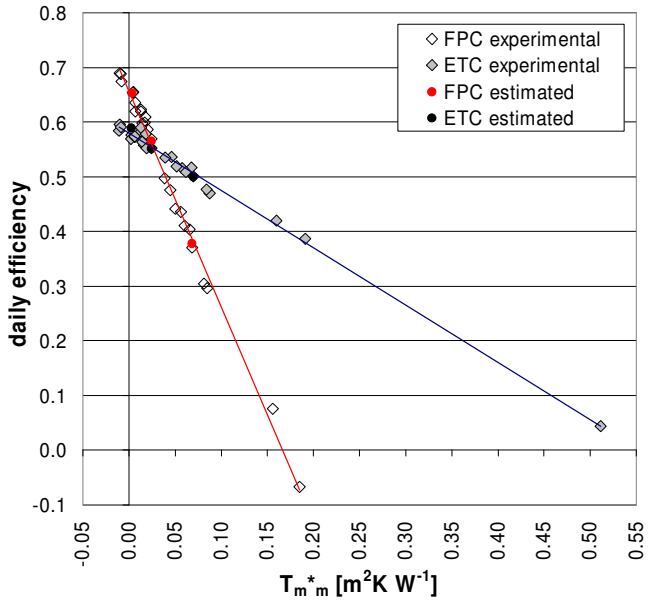

Figure 3.16. Daily efficiency curves (best-fit linear regression curves) of the evacuated and flat-plate collectors (characteristic parameters defined in Eq. (3.15); collector constants in Table 3.7).

This data shows a linear trend and this is in agreement with the simplified model presented here; the cross-over point of the regression curves occurs at an average reduced temperature value equal to 0.027 m^2K/W.

Assuming a solar daily irradiated energy of 5.6 kWh/m^2 over 8 hours, which means 700 W/m^2 average solar irradiance, and an average ambient air temperature of 20°C, the cross over point is obtained for an average fluid temperature $\overline{t_m}$ equal to 39°C (0.027 m^2K/W).

Some tests have also been performed at different mass flow rates (low flow and high flow). It is worth mentioning here that when changing the flow rate, the collector efficiency may be different but the experimental points follow the linear trend just found in the daily efficiency diagram. For instance if the mass flow rate decreases, the outlet liquid temperature increases, the mean reduced temperature increases too and the efficiency goes down.

For the sake of comparison, Figure 3.16 reports the daily efficiency estimated on three different days from the quasi-dynamic model (Sect. 3.4). For each time interval, the efficiency is calculated as in Figure 3.9 and the output power is determined as the product $\dot{Q}_{out} = G \cdot A_a \cdot \eta$. By integrating $\dot{Q}_{out}$ over the entire day, one can calculate Q_{out} and the daily efficiency can be reported in Figure 3.16. Those estimated values are in agreement with the experimental trends both for FPC and ETC. It can be seen that the

daily efficiency curve can be well plotted from the parameters determined during tests under quasi-dynamic conditions.

In Table 3.7 the parameters of the efficiency curves are reported for steady-state (second and first order curves) and daily tests.

Table 3.7. Efficiency curve parameters.

	Steady-state parameters (second order equation) $\eta = \eta_0 - a_1 T_m^* - a_2 G (T_m^*)^2$			Steady-state parameters (best-fit linear regression) $\eta = \eta_0 - a T_m^*$		Daily parameters (best-fit linear regression) $\overline{\eta} = \overline{\eta_0} - c \cdot T_m^*{}_m$	
	η_0	a_1 [W/(m^{2}K)]	a_2 [W/(m^{2}K^2)]	η_0	a [W/(m^{2}K)]	$\overline{\eta_0}$	c [W/(m^{2}K)]
FPC	0.676	3.059	0.023	0.680	3.945	0.658	3.950
ETC	0.572	0.995	0.002	0.573	1.111	0.580	1.049

From the comparison between standard stationary and daily efficiency curves, it can be observed that the zero loss efficiency parameter for evacuated tube collector has the same value for the two data sets. This is due to the $K_{\theta b}$ modifier equation: it can be seen in Figure 3.4 from $K_{\theta l}$ and $K_{\theta t}$ and in Figure 3.8, where the $K_{\theta b}$ trend is described by the difference between the experimental and the calculated efficiency. In the case of the flat-plate collector, the zero loss efficiency is lower for the daily tests as compared to the steady-state and quasi-dynamic tests due to the effect of the incidence angle. In the case of the daily curve the incidence angle modifier is lower than unity for most of the time and this explains why the efficiency decreases. In fact in the flat-plate collector the optical efficiency of the collector in the morning and in the afternoon hours decreases due to more reflection losses. In the vacuum tube collector, these efficiency losses are reduced, since because of its cylindrical geometry the most of the absorber area is exposed to quasi-normal incidence radiation for a longer period of the day.

The data points in the daily efficiency curves can be well fitted with a linear function and this verifies the hypothesis to neglect the second order term $c_2 \cdot \left(t_m - t_a\right)^2$ in Eq. (3.6) for the treatment of the daily efficiency.

The collector heat loss factor in daily conditions c and in steady-state conditions a have a similar physical mean. As shown in Figure 3.17 for both the collector types, roughly the same slope has been found for steady-state and daily tests.

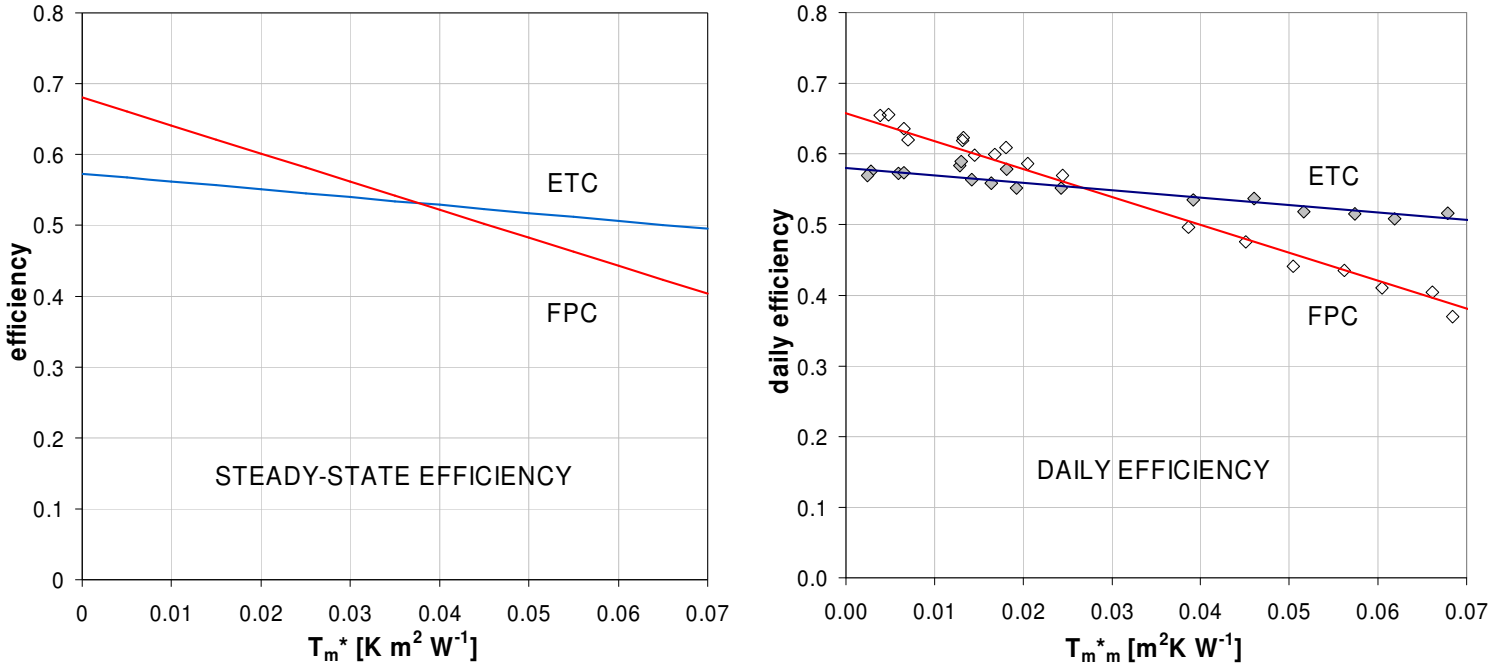

Figure 3.17. Efficiency of tested collectors: on the left, efficiency in steady-state conditions as defined in Eq. (3.5), on the right: daily efficiency as defined in Eq. (3.15).

From the comparison between the efficiency diagrams obtained in standard stationary and daily conditions, reported in Figure 3.17, as before mentioned two different cross-over points between the evacuated and flat-plate efficiency curves are observed: 0.037 m^2K/W in standard conditions and 0.027 m^2K/W in the daily tests. This difference is essentially due to the variations of $(\tau\alpha)$ in the daily tests for the evacuated tube and flat-plate collector, in fact the heat loss coefficients (in the first order curve) for both sets of data have roughly the same values.

As a result, in the daily tests the evacuated collector displays a higher efficiency for a larger range of operating conditions, as compared to the flat-plate collector.

The daily average reduced temperature can represent a proper characteristic parameter for usual working conditions and it may be calculated from ambient data and operating conditions. Moreover by using the parameters of the quasi-dynamic model, it is possible to estimate the daily efficiency, covering a wider range of operating conditions as compared to the stationary standard case.

The collector coefficients from the quasi-dynamic model can be used for the simulation of the yearly energy production in a region with specified climatic characteristics using TMY (Typical Meteorological Year) described in Marion and Urban (1995), but can also been used to construct a daily efficiency curve which represents an easy-to-use tool for quick evaluation of collectors (without to consider the system) in a wide range of operating conditions.

Chapter 4.
Numerical model for flat-plate solar thermal collector

4.1 Introduction

The glazed flat-plate collector is the most widely used device to convert solar radiation in many Countries. The main function of its simple geometry is to optimize the absorption of the incident radiation and to transfer the retained heat flux to the working fluid flowing through the tubes welded to the absorber sheet; to achieve this goal, the heat transfer to the surrounding has to be minimized.

Numerical models permit to obtain virtual prototypes and provide information on the predicted performance without constructing expensive series of prototypes. From this analysis it is possible to identify aspects that need improvement to optimize the flat-plate collector design.

Duffie and Beckman (2006) developed a model for flat-plate solar collector in steady-state conditions that has been widely used for design and prediction, employing a 1-D approach to describe the heat transfer from the absorber sheet to the thermal fluid and external ambient.

Some works present similar or different approaches: Cadafalch (2009) considers an extension of the aforementioned Duffie and Beckman model; Al-Ajlan et al. (2003) present a similar approach to simulate the performance of a solar system; Minn et al. (2002) present a 3-D approach where the absorber plate is modelled as a 2-D parameter to consider the effects of the thermal conduction; these effects are studied in depth in Phillips (1979).

In this chapter a new 3-D stationary model is described: the edge losses are considered, the thermo-physical properties of collector insulation and working fluid are dependent on the temperature and the effect of axial and transversal (referred to mass flow direction) conduction are accounted for.

The model allows to simulate the behaviour of glazed solar flat-plate collectors in steady-state conditions obtaining the efficiency curve as a function of the reduced

temperature difference. Besides it is able to predict the temperature profiles across the absorber sheet and along the tubes.

This model allows to analyse comparative effects of varying design choices, with regard to geometry and materials.

In this chapter is illustrated the theoretical basis of the collector model and its experimental validation using as a comparative tool the efficiency curve obtained from experimental tests on two flat-plate collectors following the European standard EN 12975 (2006). One collector used in the tests has been realised exclusively for the validation of the present model: fifty thermocouples are applied to investigate the heat losses and optical characteristics, measuring the temperature profile in the copper sheet between contiguous tubes, the internal and external glass cover temperature, the temperature profile along the tubes and the air temperature between plate and cover.

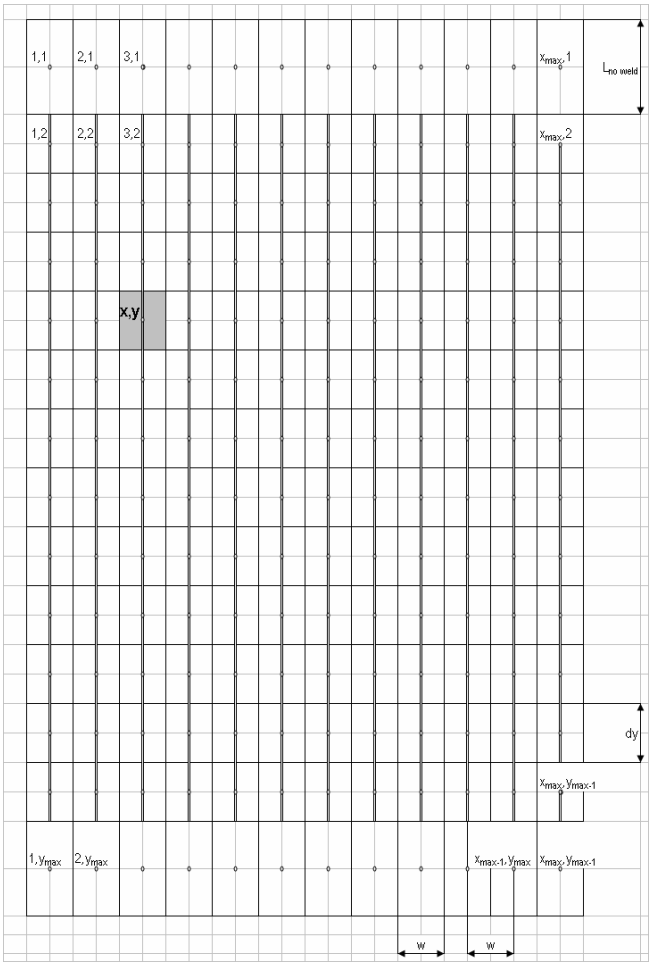

Figure 4.1. Scheme of the absorber plate divided in control elements.

4.2 The numerical model

The solar collector is modelled as a pile of components: the back insulation, the absorber plate, the air gap and the glass cover, where the absorber plate is the main element and it is exposed to an input heat flux (solar radiation); the loss heat transfer is obtained from the heat flux transfer computation between each other element, where the driving force for the global loss heat transfer is the temperature difference between plate and external ambient.

To obtain a more detailed model the absorber plate has been divided in 2-dimensional control elements and it is also considered the conductive heat transfer between contiguous elements in a steady-state analysis. In Figure 4.1 is shown the scheme of the absorber plate divided in control elements.

4.2.1 The overall computational procedure

The flow chart reported in Figure 4.2 describes the collector computational procedure. This procedure is divided in two different steps: in the first step, the simulation does not consider the thermal conduction between different control elements while in the second one this term is calculated using the temperature map previously obtained.

Considering a control element, one element of the absorber plate with the welded tube in the centre, length *dx* and width *w* the distance between two adjacent tubes, as shown in Figure 4.1, the useful heat flux $\dot{Q}_{out\_x,y}$ can be written as:

$$\dot{Q}_{out\_x,y} = \vartheta \cdot \dot{m}_{x,y} \cdot c_p \cdot \left(t_{out\_x,y} - t_{in\_x,y}\right) \tag{4.1}$$

where $\dot{m}_{x,y}$ is the mass flow rate flowing through the tube welded to the absorber element, $t_{in\_x,y}$ and $t_{out\_x,y}$ are the inlet and outlet fluid temperatures and c_p is the specific heat of the working fluid. The switching function ϑ is equal to 1 for the control element welded with the tube and equal to 0 in the case of edge elements where the tubes are not welded (the zone where is positioned the manifold tubes). This division is necessary in fact the behaviour of the edge elements is completely different from the other ones. If the function ϑ is equal to 1, the useful heat flux can be described by the Bliss equations:

$$\dot{Q}_{out\_x,y} = A_{x,y} \cdot \left((\tau\alpha) \cdot G - U_{c\_x,y} \cdot \left(t_{p\_x,y} - t_a\right)\right) \tag{4.2}$$

where $A_{x,y}$ is the control element area, $(\tau\alpha)$ is the transmittance-absorptance term, G is the global solar irradiance, $U_{c\_x,y}$ is the overall heat loss coefficient, $t_{p\_x,y}$ is the

average absorber plate temperature in the control element and t_a is the ambient air temperatures. The energy balance for a generic control element in the case where thermal conduction between different control elements is not considered (first step) is described by:

$$0 = (\tau\alpha)\cdot G - U_{c\_x,y}\cdot\left(t_{p\_x,y} - t_a\right) - \vartheta\cdot U_{tp\_x,y}\cdot\left(t_{p\_x,y} - t_{m\_x,y}\right) \tag{4.3}$$

where the first term in the right-side represents the input heat flux coming from the solar radiation through the glass cover, the second one corresponds to thermal heat losses toward the external ambient and the third term represents the useful heat flux which is transferred between the plate and the fluid flowing into the tubes (temperature difference $t_{p\_x,y} - t_{m\_x,y}$). $U_{tp\_x,y}$ is the heat transfer coefficient between the plate and the fluid; it also accounts the convective heat transfer coefficient of the fluid flow inside the tubes. The convective heat transfer coefficient is calculated by using the equations from Duffie and Beckman (2006) with the empirical values reported in Lazzarin (1981) in the case of laminar flow, and the Colburn equation reported in Incropera and DeWitt (1996) in the case of turbulent flow.

The same energy balance can be written in the case where the thermal conduction between different control elements is also considered:

$$\begin{aligned} 0 = {} & (\tau\alpha)\cdot G - U_{c\_x,y}\cdot\left(t_{p\_x,y} - t_a\right) - \vartheta\cdot U_{tp\_x,y}\cdot\left(t_{p\_x,y} - t_{m\_x,y}\right) + \\ & + \lambda_p\cdot\delta_p\cdot\frac{\partial^2 t_{p\_x,y}}{\partial x^2} + \left(\lambda_p\cdot\delta_p + \lambda_t\cdot\pi\cdot\left(\frac{D^2 - d^2}{4}\right)\right)\cdot\frac{\partial^2 t_{p\_x,y}}{\partial y^2} \end{aligned} \tag{4.4}$$

where the fourth and fifth terms are the term of the conduction heat transfer through the absorber plate (and along the welded tube in its direction), λ_p and λ_t are the thermal conductivities of the absorber plate and the tube respectively, δ_p is the plate thickness, D and d are the internal and external tube diameters.

From the fin theory is calculated the collector efficiency factor F' and the collector heat removal factor F_R as reported in Duffie and Beckman (2006); these factors are used to obtain the useful heat transfer in the control element.

From the computation of these coefficients, with an iterative method, it is possible to obtain the plate temperature of the control elements from Eqs. (4.3) and (4.4).

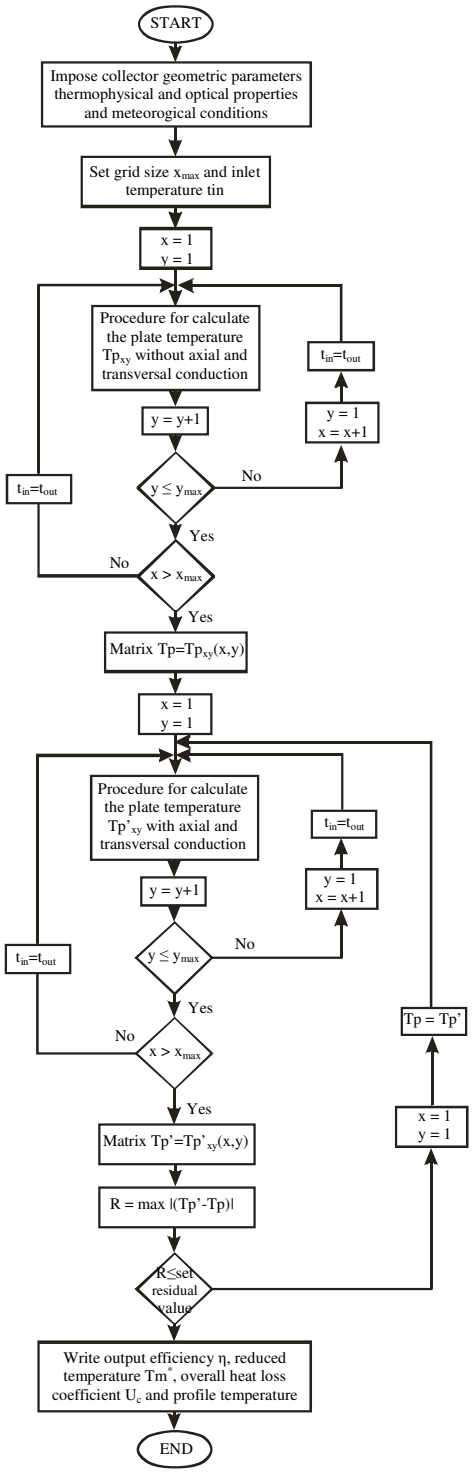

Figure 4.2. Overall collector computational procedure flow chart.

4.2.2 Input heat flux in the absorber plate element

In the energy balances reported in Eqs. (4.3) and (4.4).the input flux in the absorber plate coming from the solar radiation through the glass cover is described by the transmittance-absorptance *(τα)* term. To maintain the form of Eq. (4.2) and account for the reduced thermal losses due to absorption of solar radiation by the glass, an effective transmittance-absorptance product *(τα)* is introduced following the guidelines described in Duffie and Beckman (2006):

$$(\tau\alpha) = (\tau\alpha)' + \left(1-\tau_a\right)\sum_{i=1}^{n_{cover}} a_i \tau^{i-1} \tag{4.5}$$

where a_i is the ratio of the top loss coefficient from the ith cover to the surroundings and τ_a is the transmittance of a single cover defined as:

$$\tau_a = e^{-\frac{K \cdot s_c}{\theta_{ref}}} \tag{4.6}$$

where K is the extinction coefficient, s_c is the cover thickness and θ_{ref} is the angle of refraction.

The values of a_i actually depend upon the plate temperature, ambient temperature, plate emittance and wind speed. In Table 4.1 are reported a_i values for one, two and three covers and for different plate emittances. These values are provided by Duffie and Beckman (2006) and Lazzarin (1981) for fixed conditions.

Table 4.1. Coefficients used in Eq. (4.5).

Number of cover	a_i	ε_p=0.95	ε_p=0.50	ε_p=0.20	ε_p=0.10
1	a_1	0.27	0.21	0.14	0.13
2	a_1	0.15	0.12	0.10	0.09
	a_2	0.62	0.53	0.44	0.40
3	a_1	0.14	0.08	0.08	0.06
	a_2	0.45	0.40	0.35	0.31
	a_3	0.75	0.67	0.58	0.53

In the present work it has been considered the case of a collector with a single glass cover, perpendicular incident solar radiation and a selective absorber surface (ε_p=0.20):

$$(\tau\alpha) = (\tau\alpha)' + 0.14 \cdot \left(1 - e^{-(K \cdot s_c)}\right) \tag{4.7}$$

where the value for the extinction coefficient K is 4 m^{-1} ("water white" glass).
The first term in the right-side of Eq. (4.7) is obtained by the numerical series:

$$(\tau\alpha)' = \tau_c \cdot \alpha \cdot \sum_{n=0}^{\infty}[(1-\alpha)\cdot\rho_d]^n = \frac{\tau_c \cdot \alpha}{1-(1-\alpha)\cdot\rho_d} \tag{4.8}$$

It describes the multiple absorption terms described in Figure 4.3. Of the incidence energy, $\tau\alpha$ is absorbed by the absorber plate and $(1-\alpha)\tau$ is reflected back to the cover system. The reflection from the absorber plate is assumed to be diffuse so the fraction $(1-\alpha)\tau\rho_d$ is reflected back to the absorber sheet. The quantity ρ_d is the reflectance of the cover for diffuse radiation and can be estimated as the difference between τ_a and τ_c at an angle of 60°. The multiple reflections of diffuse radiation can be considered infinites.

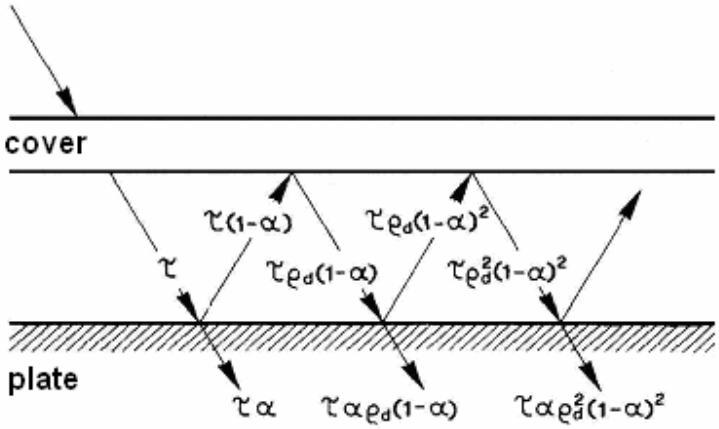

Figure 4.3. Multiple absorption terms of the solar radiation in a single glazed collector.

In Eq. (4.8) τ_c is the transmittance of the cover sheet: its value is obtained from the test report for the considered cover. The term α is the absorptance of the absorber plate: it is considered to change with the angle of incidence of the solar radiation θ as described in Duffie and Beckman (2006):

$$\alpha = \alpha_0 \cdot (\cos\theta)^{1/4} \tag{4.9}$$

where α_0 is obtained from the test report of the coating surface of the absorber plate and in the case of the welded control elements (switching function ϑ=1), it is

considered an average value α_0 considering the ultrasonic welding trail, where is not present the selective coating.

4.2.3 Element overall heat loss coefficient

In the energy balances reported in Eqs. (4.3) and (4.4) the overall heat loss between a control element of the absorber plate and the external ambient is described by the term $U_{c\_x,y} \cdot \left(t_{p\_x,y} - t_a\right)$, where U_c is the overall heat loss coefficient.

The overall heat loss coefficient between plate and surrounding is the sum of the top, bottom and edge loss coefficient:

$$U_c = U_{up} + U_{down} + U_{edge} \tag{4.10}$$

The input heat flux, the top and the bottom heat transfer components are shown in Figure 4.4.

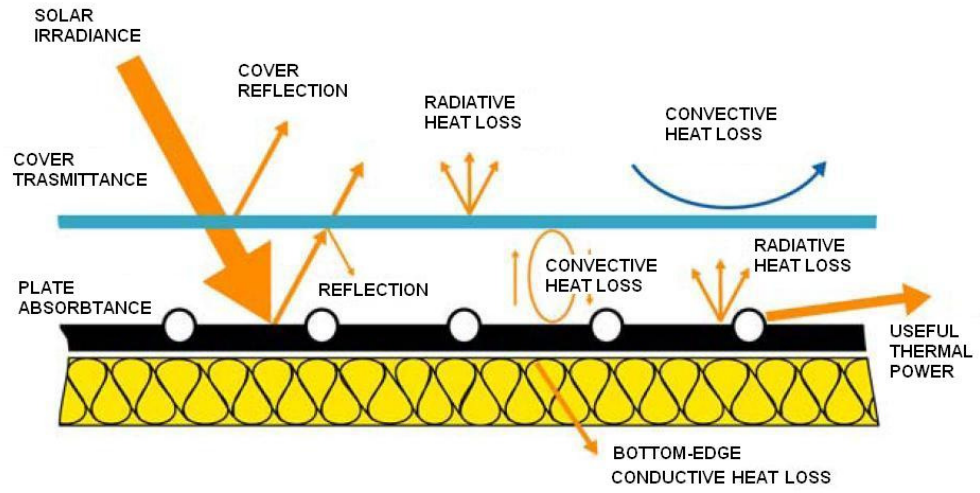

Figure 4.4. Schematic view of different heat transfer components in a flat-plate solar collector.

The top coefficient U_{up} is obtained as described in Duffie and Beckman (2006):

$$U_{up} = \left(\frac{1}{h_{Rad\_p-c} + h_{Conv\_p-c}} + \frac{1}{h_{Rad\_c-a} + h_{Conv\_c-a}} \right)^{-1} \tag{4.11}$$

The $h_{Conv\_p\text{-}c}$ term considers the free-convection between absorber sheet and glass cover:

$$h_{Conv\_p-c} = \frac{\mathrm{Nu}_{\mathrm{p\text{-}c}} \cdot \lambda_{p-c}}{s_{p-c}} \tag{4.12}$$

where $\lambda_{p\text{-}c}$ is the thermal conductivity of the air gap between plate and cover at the average temperature between plate and cover temperatures, $s_{p\text{-}c}$ is the air gap thickness and $\mathrm{Nu}_{\mathrm{p\text{-}c}}$ is the Nusselt number calculated using the model suggested by Hollands et al. (1976) for tilt angles from 0 to 75°:

$$\mathrm{Nu}_{\mathrm{p\text{-}c}} = 1 + 1.44 \cdot \left(\frac{|Z_1| + Z_1}{2} \right) \cdot \left(1 - \frac{1708 \cdot (\sin 1.8\beta)^{1.6}}{\mathrm{Ra} \cdot \cos\beta} \right) + \left(\frac{|Z_2| + Z_2}{2} \right) \tag{4.13}$$

where Ra is the Rayleigh number, β is the collector tilt, Z_1 is defined as:

$$Z_1 = 1 - \frac{1708}{\mathrm{Ra} \cdot \cos\beta} \tag{4.14}$$

and Z_2 is defined as:

$$Z_2 = \left(\frac{\mathrm{Ra} \cdot \cos\beta}{5830} \right)^{1/3} - 1 \tag{4.15}$$

The model reported in VDI (1993) for vertical surfaces can be used for tilt angle $\beta >$ 75°.

For the $h_{Conv\_c\text{-}a}$ term (external convection) in Eq. (4.11), the relationship recommended by Mc Adams (1954) is used:

$$h_{Conv\_c-a} = 5.7 + 3.8 \cdot u \tag{4.16}$$

where u is the wind speed.

The $h_{Rad\_p\text{-}c}$ term in Eq. (4.11), considers the radiative heat transfer between absorber plate and cover:

$$h_{Rad\_p-c} = \frac{\sigma \cdot (T_p + T_c) \cdot (T_p^{\,2} + T_c^{\,2})}{\frac{1}{\varepsilon_p} + \frac{1}{\varepsilon_c} - 1} \tag{4.17}$$

where σ is the Stefan-Boltzman constant, T_p is the plate temperature, T_c is the cover temperature, ε_p and ε_c are the emittances in the infrared wavelength range of the plate and of the cover respectively.

The $h_{Rad\_c\text{-}a}$ term in Eq. (4.11) considers the radiative heat transfer between cover and sky:

$$h_{Rad\_c-a} = \frac{\sigma \cdot \varepsilon_c \cdot (T_c^{\,4} - T_s^{\,4})}{(T_c - T_a)} \tag{4.18}$$

where T_c is the cover temperature, T_a is the ambient air temperature and T_s is the sky temperature obtained by means of the simple Whillier equation for clear sky (for cloudy conditions it can be assumed $T_s = T_a$):

$$T_s = T_a - 6 \tag{4.19}$$

The bottom coefficient in Eq. (4.10) considers the conduction heat transfer through the back board insulation; this coefficient is considered variable with the average temperature of the insulation following the standard EN ISO 10456 (2008):

$$U_{down} = \frac{\lambda_b}{s_b} = \frac{\lambda_{b0} \cdot F_t}{s_b} \tag{4.20}$$

where λ_b and λ_{b0} are the actual and the reference values for the thermal conductivity of the back insulation, s_b is the thickness of the back board insulation and F_t is the corrective factor calculated as:

$$F_t = e^{ft \cdot (t_b - t_{b0})} \tag{4.21}$$

where *ft* is the temperature conversion coefficient and t_{b0} is the reference temperature provided by the standard. t_b is the insulation temperature calculated as the average temperature between plate and external ambient.

The computation of the edge heat losses in Eq. (4.10) considers different terms. In the zone above the insulation board, the convective and radiative heat transfer is considered because in the analyzed case there is not lateral insulation.

$$U_{edge} = \frac{h_{Cond\_p-e} \cdot A_{edge\_dw} + \left(h_{Conv\_p-e} + h_{Rad\_p-e}\right) \cdot A_{edge\_up}}{A_{x,y}} \tag{4.22}$$

where $A_{x,y}$ is the control element area, A_{edge_dw} is the edge lateral area in the back side of the absorber plate, A_{edge_up} is the edge lateral area in the upper side of the absorber plate, h_{Cond_p-e}, h_{Conv_p-e}, h_{Rad_p-e} are the conductive, convective and radiative coefficient obtained as:

$$h_{Cond\_p-e} = \frac{\lambda_b}{s_{edge}} \tag{4.23}$$

$$h_{Conv\_p-e} = h_{Conv\_p-c} \tag{4.24}$$

$$h_{Rad\_p-e} = \frac{A_{x,y}}{A_{edge\_up}} \cdot F_v \cdot \varepsilon_p \cdot \sigma \cdot \left(T_p + T_a\right) \cdot \left(T_p^{\,2} + T_a^{\,2}\right) \tag{4.25}$$

where s_{edge} is this case the distance between the edge of the insulation board and the plate edge, F_v is the view factor between absorber control area and lateral surface, considered at external air temperature T_a.

4.2.4 Useful heat transfer coefficient

In Figure 4.5 are reported the characteristic dimensions of the case considered in this procedure.

The heat transfer coefficient U_{tp} in Eqs. (4.3) and (4.4) is calculated from the useful heat flux for each control element. This term $\dot{Q}_{out}$ (reported in Eq. (4.1)) is zero in the control areas where the switching function ϑ=0, whereas it is calculated in the welded area, where the switching function ϑ=1 as:

$$\dot{Q}_{out} = F_R \cdot A_{x,y} \cdot \left[(\tau\alpha) \cdot G - U_c \cdot \left(t_{in\_x,y} - t_a\right)\right] \tag{4.26}$$

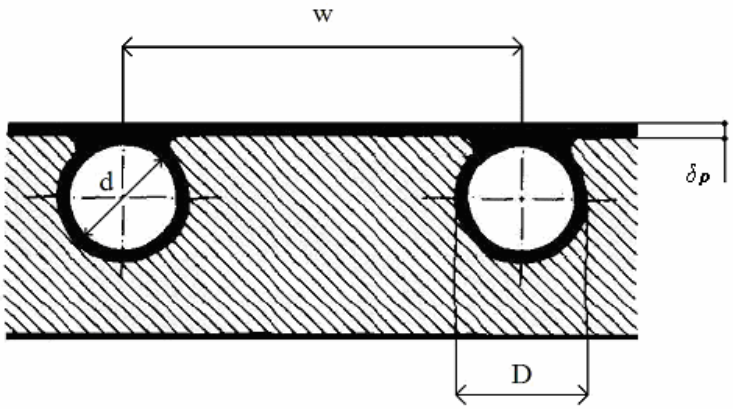

Figure 4.5. Sheet and tube dimensions.

For each control element the collector heat removal factor F_R is the ratio of the actual useful energy gain to the useful gain that would result if the absorbing surface had been at the local fluid inlet temperature. It is defined as reported in Duffie and Beckman (2006):

$$F_R = \frac{\dot{m} \cdot c_p}{A_{x,y} \cdot U_c} \cdot \left[1 - e^{-\frac{A_{x,y} \cdot U_c \cdot F'}{\dot{m} \cdot c_p}} \right] \tag{4.27}$$

where $\dot{m}$ is the mass flow rate in a single tube and F' is the efficiency factor, that represents the ratio of the actual useful energy gain to the useful gain that would result if the absorbing surface had been at the local (average) fluid temperature. For the plate and tube configuration shown in Figure 4.5 it is defined as:

$$F' = \frac{1}{\frac{w \cdot U_c}{\pi \cdot d \cdot h_f} + \frac{w \cdot U_c}{C_b} + \frac{w}{D + (w - D) \cdot F}} \tag{4.28}$$

where w, D and d are the dimensions reported in Figure 4.5, C_b the bond (welding) conductance, h_f the convective heat transfer coefficient for fluid inside tubes and F is:

$$F = \tanh\left(\frac{m \cdot (w - D)}{2}\right) \Big/ \left(\frac{m \cdot (w - D)}{2}\right) \tag{4.29}$$

and

$$m = \sqrt{\frac{U_c}{\lambda_p \cdot \delta_p}} \tag{4.30}$$

where λ_p is the thermal conductivity of the absorber plate and δ_p is the plate thickness.

The convective heat transfer coefficient for fluid flow inside the tubes in Eq. (4.28) is calculated as:

$$h_f = \frac{\mathrm{Nu_f} \cdot \lambda_f}{d} \tag{4.31}$$

where λ_f is the fluid thermal conductivity; $\mathrm{Nu_f}$ is the Nusselt number, obtained from Duffie and Beckman (2006) by equations with parameter values reported in Lazzarin (1981) for the laminar flow:

$$Nu_f = 4.36 + \frac{0.067 \cdot \left((d/L) \cdot \mathrm{Re} \cdot \mathrm{Pr}\right)}{1 + 0.04 \cdot \left((d/L) \cdot \mathrm{Re} \cdot \mathrm{Pr}\right)^{2/3}} \qquad \text{for Re} \leq 2300 \tag{4.32}$$

For the turbulent flow is used the Colburn equation reported in Incropera and DeWitt (1996):

$$\mathrm{Nu_f} = 0.023 \cdot \mathrm{Re}^{0.8} \cdot \mathrm{Pr}^{1/3} \qquad \text{for Re} > 2300 \tag{4.33}$$

where L is the tube length, Re and Pr are the Reynolds and Prandtl numbers.

Other equations has been analyzed for the laminar flow case: Shah and London reported in VDI (1993) for constant heat flux and constant wall temperature, Mohammed and Salman (2007) for different tilt angle, Sieder and Tate and Hausen reported in Incropera and DeWitt (1996).

The heat transfer coefficient between the plate and the fluid U_{tp} (in Eqs. (4.3) and (4.4)) accounts also the convective heat transfer coefficient of the fluid flow inside the tubes. It is obtained knowing the useful heat flux Q_{out}, fluid t_f and plate t_p temperatures:

$$U_{tp} = \frac{\dot{Q}_{out}}{\left(t_p - t_m\right) \cdot A_{x,y}} \tag{4.34}$$

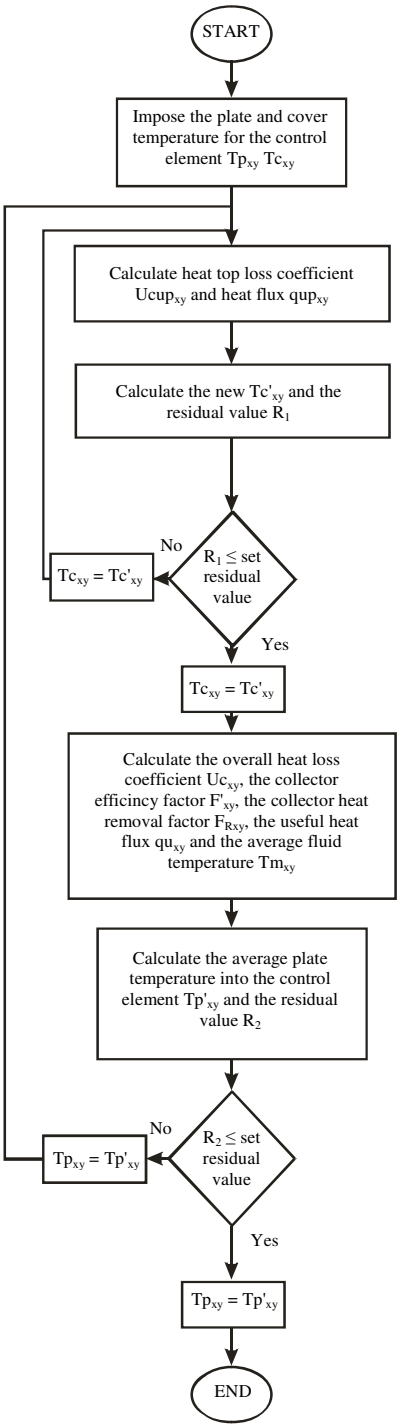

Figure 4.6. Plate temperature computational procedure.

The iterative method to obtain the useful heat transfer coefficient, the average working fluid temperature and the plate temperature of a control element is described in the flow chart in Figure 4.6 where it is reported a scheme valid for both the considered cases, with and without plate and tube conduction.

4.3 Numerical model validation

The purpose of this work is to develop and validate a tool to predict the stationary behaviour of solar flat-plate collectors. Therefore, an important step is to compare the efficiency curve measured in steady-state conditions on the tested collector with the predicted curve obtained from the simulation of a virtual solar collector with the same geometrical and physical characteristics.

Two flat-plate collectors have been tested to compare experimental results with model predictions: a prototype collector realised exclusively for this purpose and a flat-plate collector with aluminium absorber plate.

4.3.1 First validation phase: prototype collector

Test measurements have been performed in a flat-plate collector, which is a prototype collector composed by a copper absorber sheet, covered by a selective coating, with 12 parallel cooper tubes, a low-iron glass cover and a posterior mineral wool board insulation. The collector housing is composed by lateral frames and an aluminium back sheet. The tubes are bonded to the plate by ultrasonic welding.

In Figure 4.7 is shown the prototype collector installed in the test plant and in Table 4.2 are reported its main characteristics.

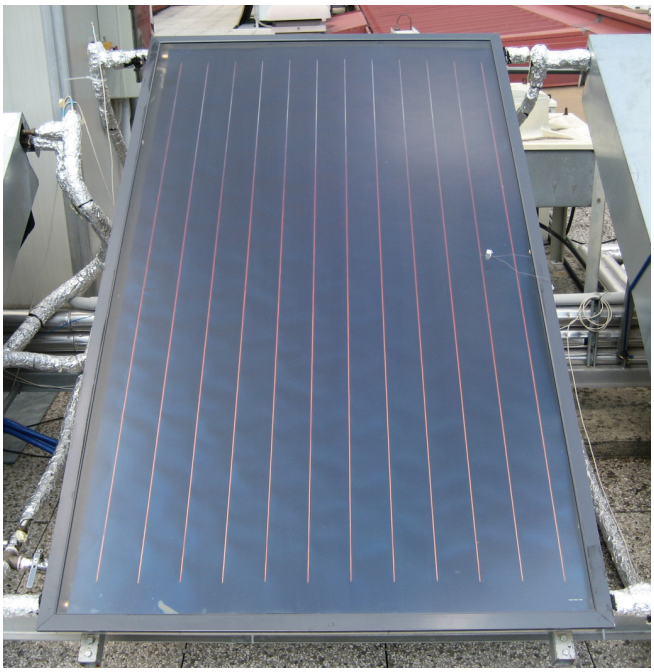

Figure 4.7. Prototype collector.

Table 4.2. Characteristics of the collector prototype.

Aperture surface [m^2]	2.2
Absorber length [m]	1.955
Absorber width [m]	1.092
Tilt angle [°]	45
Number of flow channels in parallel	12
Spacing between tubes, *w* [m]	0.091
Internal tube diameter [m]	0.007
Absorber plate thickness, δ[mm]	0.18
Back insulation thickness [m]	0.04
Glass cover thickness [m]	0.0032
Cover-plate distance [m]	0.0025
Trasmittance-absorptance product at normal incidence $(\tau\alpha)_{en}$	0.886
Absorber emittance, ε	0.04

In this collector 49 copper-constantan thermocouples are installed:

- 12 at the outlet section of the tubes grid (in each tube as shown in Figure 4.8)
- 8 at the inlet section of the tubes
- 16 in the copper plate between adjacent tubes at the central section of the collector (Figure 4.9)
- 7 in the copper plate at ¾ of the total length from the inlet (Figure 4.10)

- 3 axially welded to a tube to describe the temperature profile along its length
- 2 pasted to the glass by means of a high conducting glue; both inside and outside the glass, punctually shaded by a reflective and insulating protection (Figure 4.11)
- 1 to measure the air temperature between copper sheet and glass (Figure 4.12).

A similar approach for the prototype instrumentation is described in Groenhout et al. (2002).

In the back side of the collector some inspection windows are applied to make it possible to use an infrared camera for the analysis of the temperature profile in the copper sheet.

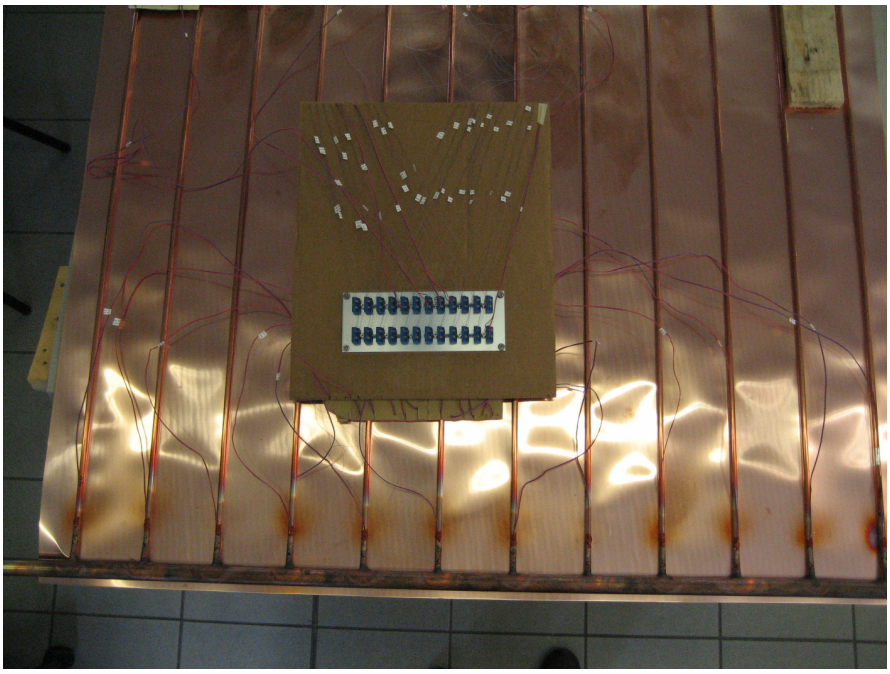

Figure 4.8. Back side of the absorber sheet. Thermocouples welded to the outlet section of the tubes.

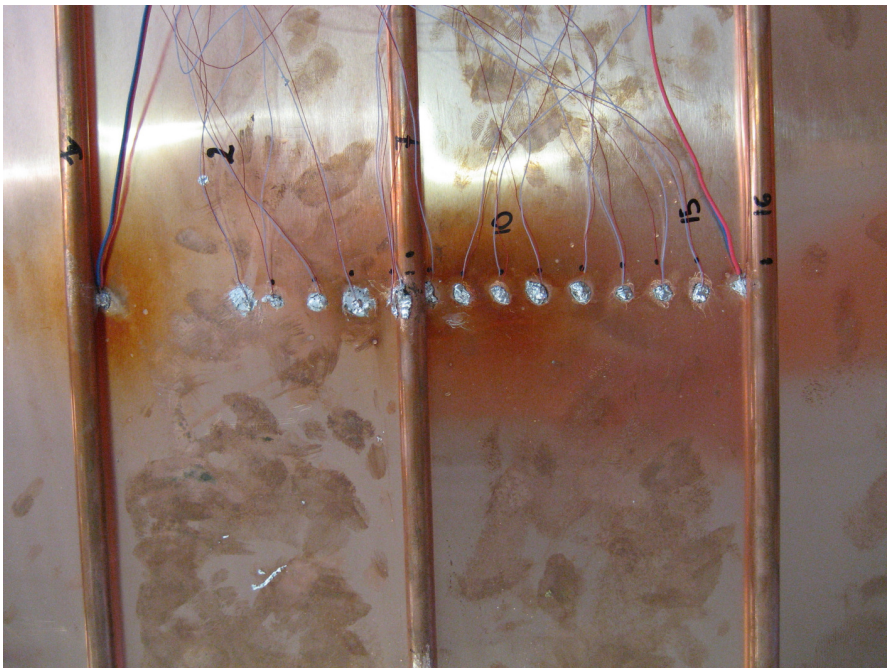

Figure 4.9. Back side of the absorber sheet. Thermocouples welded to the central section.

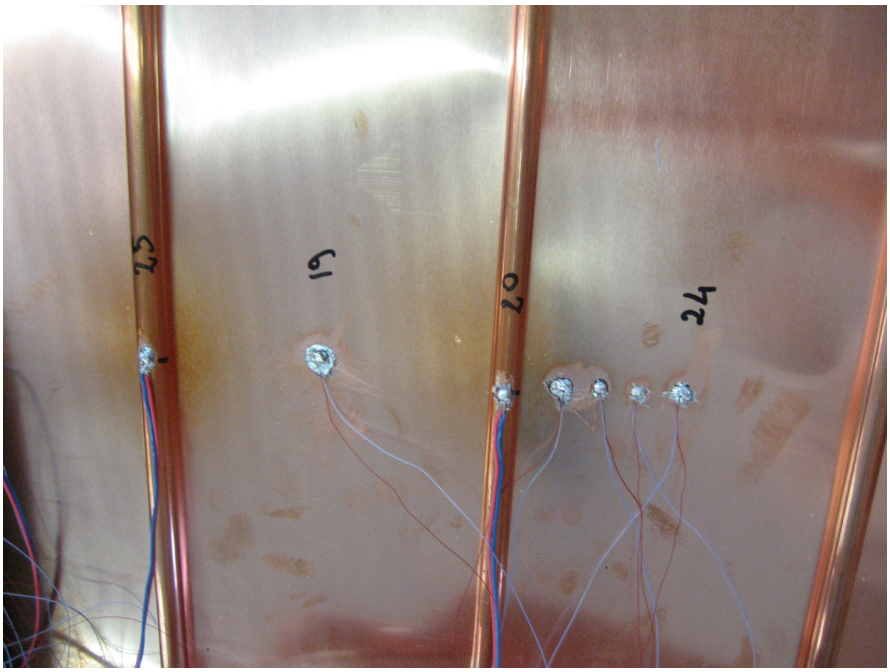

Figure 4.10. Back side of the absorber sheet. Thermocouples welded at ¾ of the total length from the inlet section.

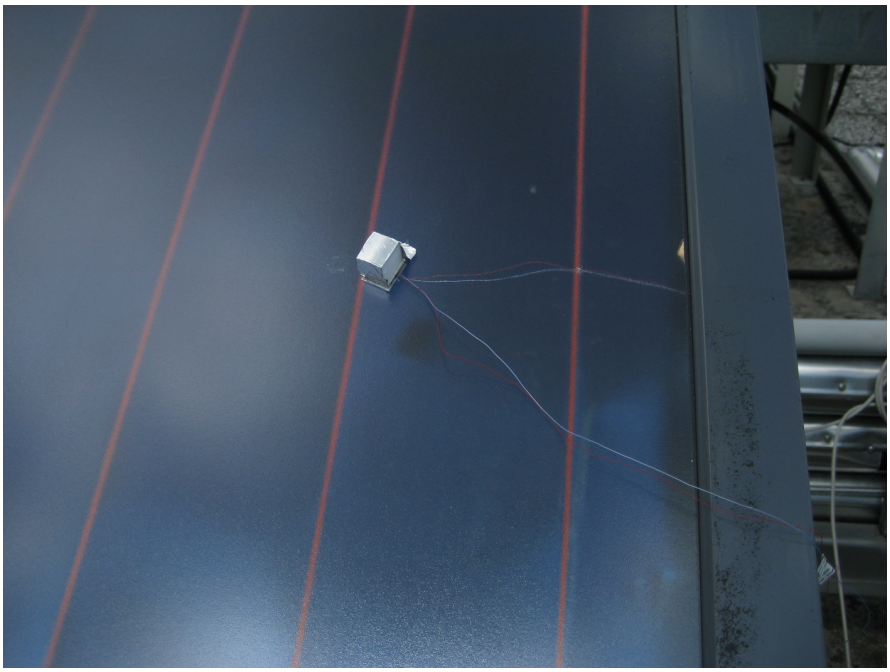

Figure 4.11. Two thermocouples applied to the glazed cover: inside and outside the glass.

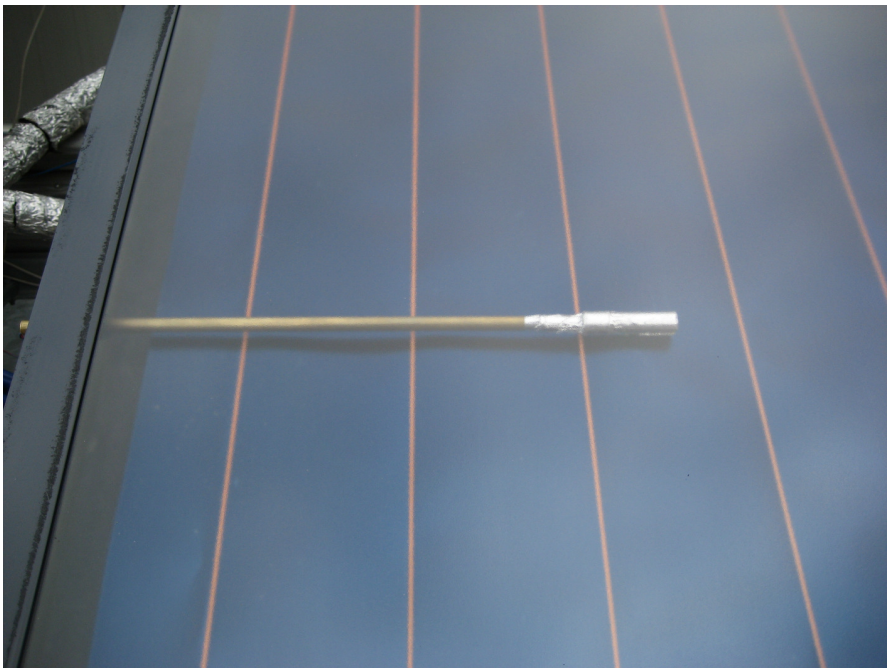

Figure 4.12. Thermocouple applied to measure the air temperature between absorber sheet and cover.

4.3.1.1 Experimental tests and results

The purpose of this work is to develop and validate a tool to predict the stationary behaviour of solar flat-plate collectors. Therefore the efficiency curve measured in steady-state conditions on the tested collector has been compared with the predicted curve obtained from the simulation of a virtual solar collector with the same geometrical and physical characteristics (reported in Table 4.2).

The model validation in this phase is not based only on the comparison of the global performance given by the efficiency curve, but the local heat transfer has been also examined, by comparing the measured temperature profile in the plate, in the tubes, in the glass cover and in the air gap between plate and cover, with the correspondent predicted temperatures.

The test runs have been performed in agreement with the standard EN 12975 (2006) as described in Zambolin and Del Col (2010) for steady-state conditions to measure the efficiency curve. This work is also described in Zambolin and Del Col (2010b).

The experimental results obtained by the steady-state efficiency tests are reported in Figure 4.13. The efficiency curve is obtained at G=1000 W/m^2.

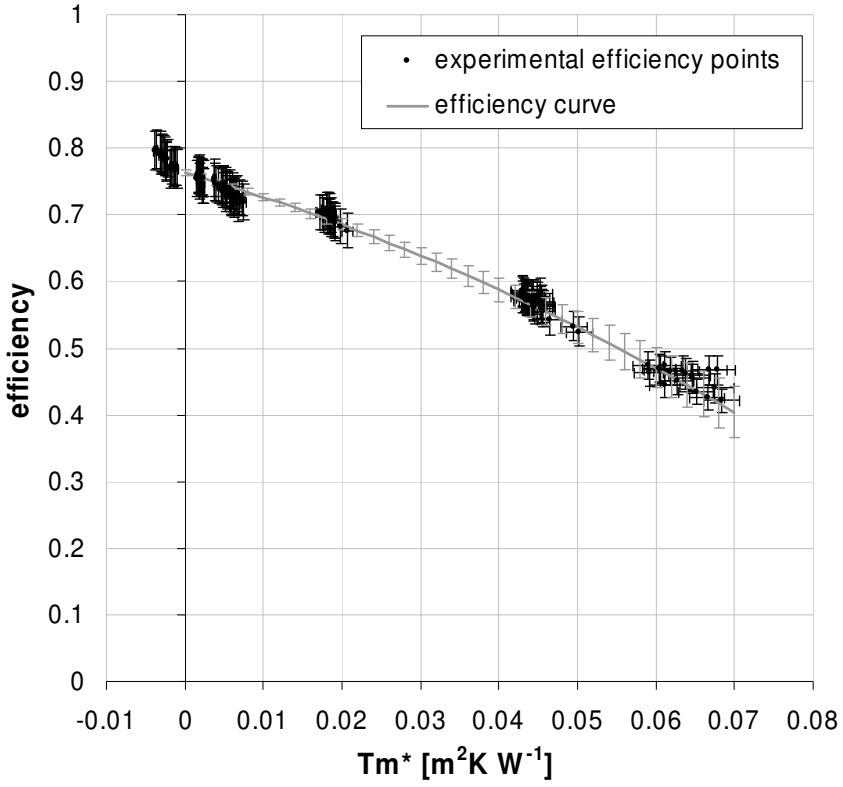

Figure 4.13. Experimental efficiency points and efficiency curve obtained at *G*=1000 W/m^2.

In Figure 4.14 the estimated efficiency curve by the model is compared with the experimental curve. The comparison between the theoretical predictions and the experimental data shows that the efficiency curve deviation is below 4.5% in the reduced temperature range between 0 and 0.07 m^2K/W; the coefficient values related to these two curves are reported in Table 4.3.

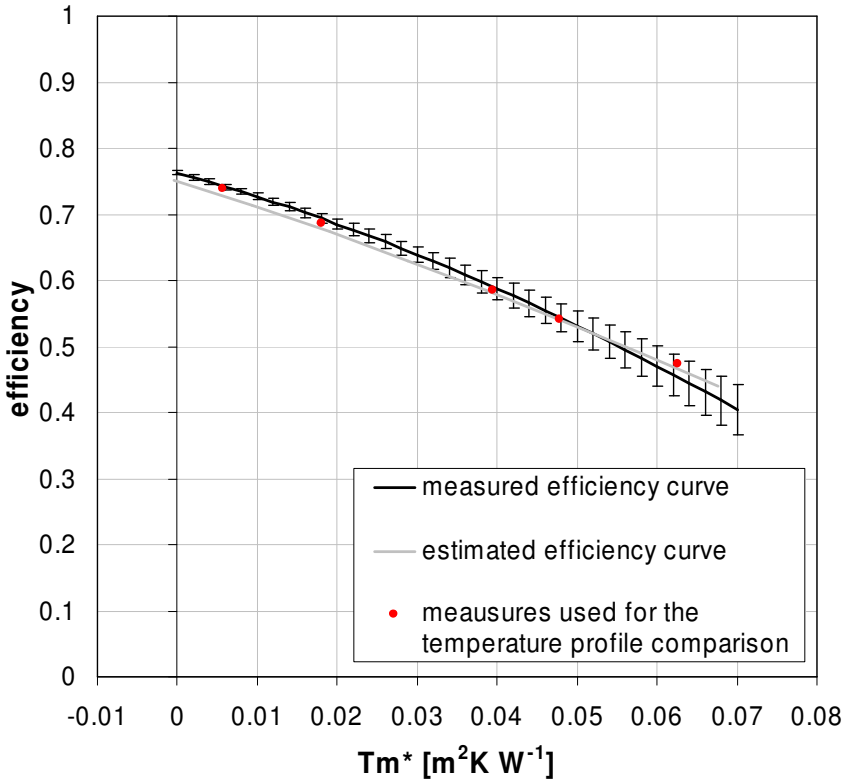

Figure 4.14. Measured and predicted efficiency curves at *G*=1000 W/m^2.

Table 4.3. Calculated and measured collector coefficients obtained by steady-state method for the prototype collector.

Coefficient	η_0 [-]	c_1 [W/(m^{2}K)]	c_2 [W/(m^{2}K^2)]
Experimental value	0.763 ± 0.004	-3.403 ± 0.345	-0.025 ± 0.006
Estimated value	0.751	-3.917	-0.010

Other five measurements used for the comparison of the temperature profiles have been performed for a range of inlet temperature between 17°C and 88°C. They are

reported as efficiency points in Figure 4.14. These experimental results are in agreement with the measured efficiency curve.

The results obtained from the temperature profile analysis at the inlet temperature 17°C and 88°C are here reported.

In Figures 4.15 and 4.16 are reported measured and estimated temperatures in the central zone of the absorber plate for the two analysed temperatures. The experimental measurements are obtained by the thermocouples shown in Figure 4.9. The fin theory used in the model describes a sheet temperature trend in good agreement with the experimental results, mostly in the low temperature case. In these diagrams the lowest temperatures are obtained in the tubes, where there is the direct heat transfer between the plate and the working fluid. The experimental temperatures obtained in the high temperature case result about 2 K higher that estimated values.

The same results are obtained from the Figures 4.17 and 4.18, where are reported measured and estimated temperatures in the zone at ¾ of the total length of the absorber plate for the two analysed cases. The experimental measurements are obtained by the thermocouples shown in Figure 4.10.

In Figure 4.19 and 4.20 are reported the measured temperatures on the tube surface, in the tube grid inlet section. The model does not estimate directly these values, so the experimental measurements are compared with the estimated fin base and fluid temperatures. From the estimated temperature profiles is possible to notice the edge effect.

The same considerations can be done for the temperatures on the tube surface in the outlet section reported in Figure 4.21 and 4.22. These measurements are obtained by the thermocouples shown in Figure 4.8.

In Figure 4.23 and 4.24 are reported the measured and estimated temperatures along a single tube of the grid.

Also in these Figures the experimental tube temperature result between the fin base temperature and the fluid temperature, in fact the tube is a intermediate element between the absorber plate and the working fluid.

Figure 4.25 reports the measured and estimated glass temperatures for the 5 different tests. These measurements have been performed with the thermocouple shown in Figure 4.11. Internal and external glass temperatures result closed. The estimated values are dependent on the wind velocity and sky temperature, characteristics don't easily valuable, so in some case the estimated values is lower than the measured values (the temperature difference is about 2 K).

In Figure 4.26 are shown the measured temperature of the air between absorber plate and glass sheet. These measurements have been performed with the thermocouple shown in Figure 4.12. The air temperature is assumed at the average value between plate and cover temperature by the model; the experimental results are similar to the model assumption for high temperature cases. In the lowest inlet temperature case this assumption has not been verified (measured $(t_a - t_c)=0.88(t_p - t_c)$), but it has been verified that the effect of this parameter is negligible on the efficiency estimation.

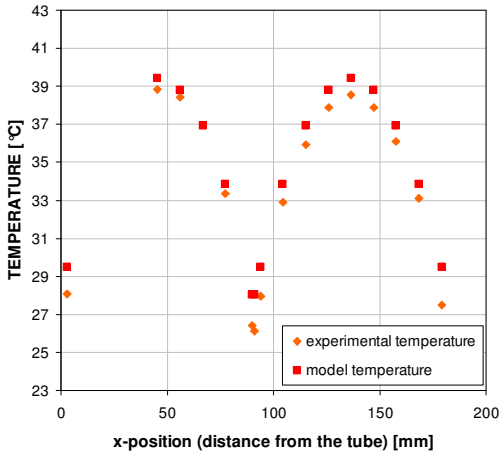

Figure 4.15. Comparison between measured and estimated temperatures in the central zone of the absorber plate at inlet temperature 17°C. The x-axis reports the distance from the tube.

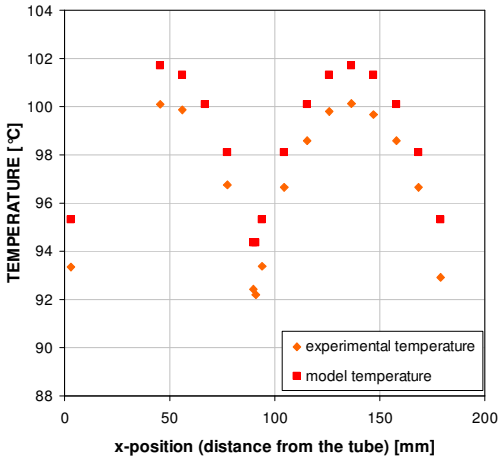

Figure 4.16. Comparison between measured and estimated temperatures in the central zone of the absorber plate at inlet temperature 88°C. The x-axis reports the distance from the tube.

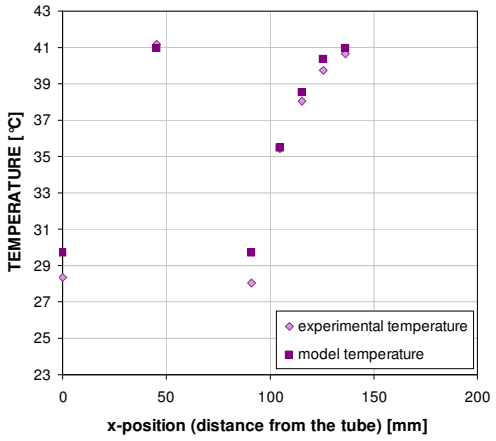

Figure 4.17. Comparison between measured and estimated temperatures in the zone at ¾ of the total length of the absorber plate at inlet temperature 17°C. The x-axis reports the distance from the tube.

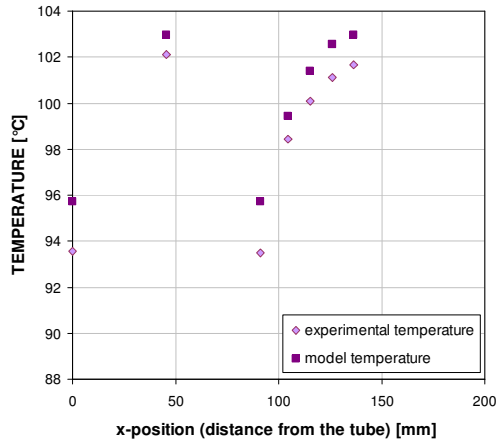

Figure 4.18. Comparison between measured and estimated temperatures in the zone at ¾ of the total length of the absorber plate at inlet temperature 88°C. The x-axis reports the distance from the tube.

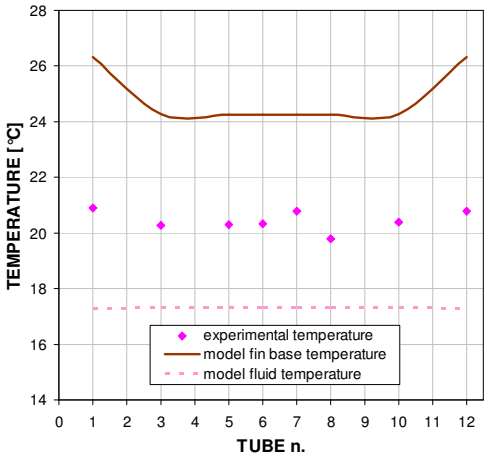

Figure 4.19. Measured and estimated temperatures in the tube inlet section at inlet temperature 17°C. Estimated values are relative to the fin base and to the fluid temperatures.

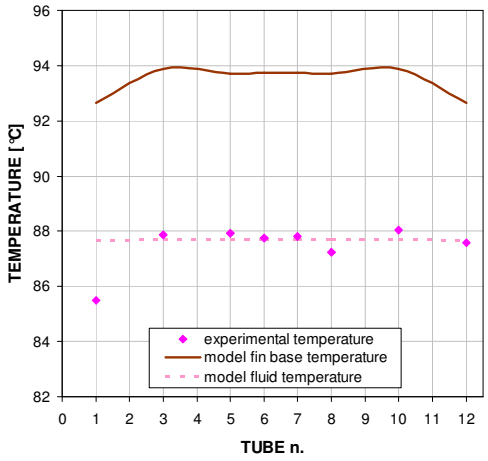

Figure 4.20. Measured and estimated temperatures in the tube inlet section at inlet temperature 88°C. Estimated values are relative to the fin base and to the fluid temperatures.

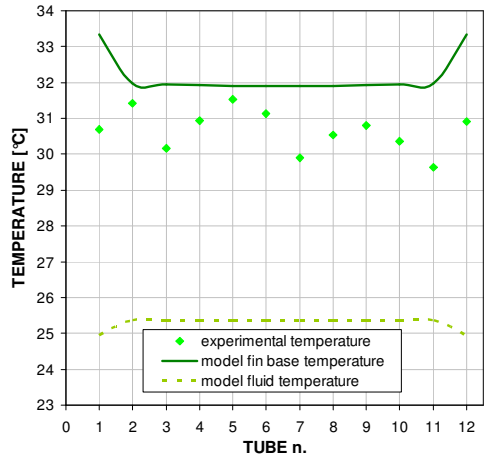

Figure 4.21. Measured and estimated temperatures in the tube outlet section at inlet temperature 17°C. Estimated values are relative to the fin base and to the fluid temperatures.

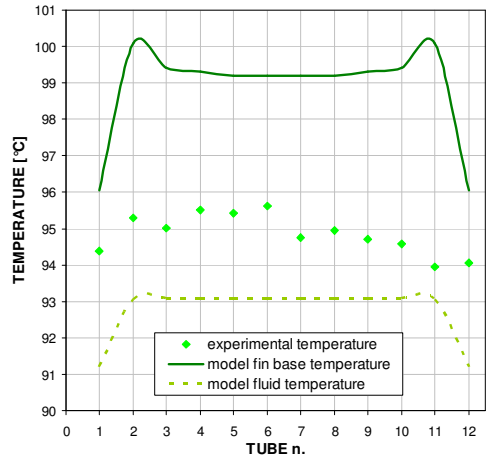

Figure 4.22. Measured and estimated temperatures in the tube outlet section at inlet temperature 88°C. Estimated values are relative to the fin base and to the fluid temperatures.

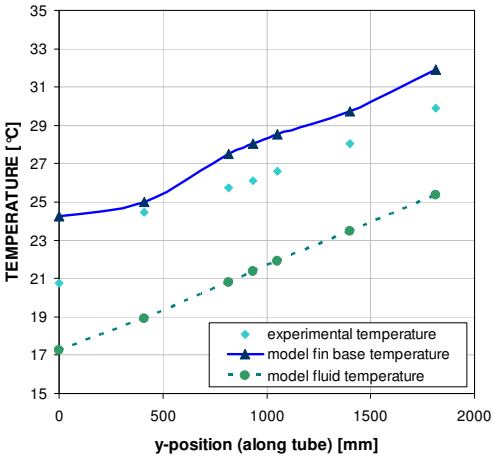

Figure 4.23. Measured and estimated temperatures along the tube at inlet temperature 17°C. Estimated values are relative to the fin base and to the fluid temperatures.

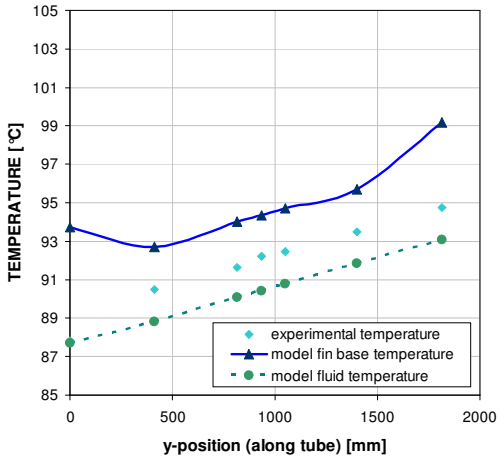

Figure 4.24. Measured and estimated temperatures along the tube at inlet temperature 88°C. Estimated values are relative to the fin base and to the fluid temperatures.

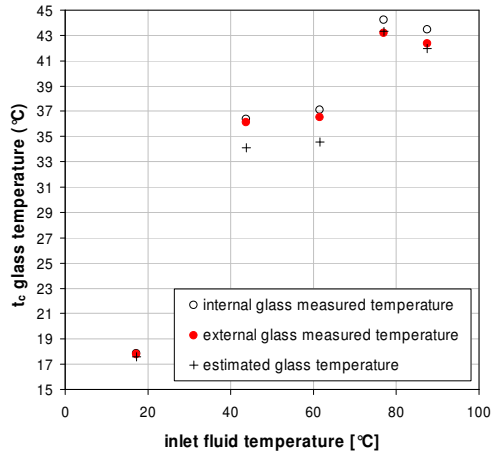

Figure 4.25. Measured and estimated glass temperatures.

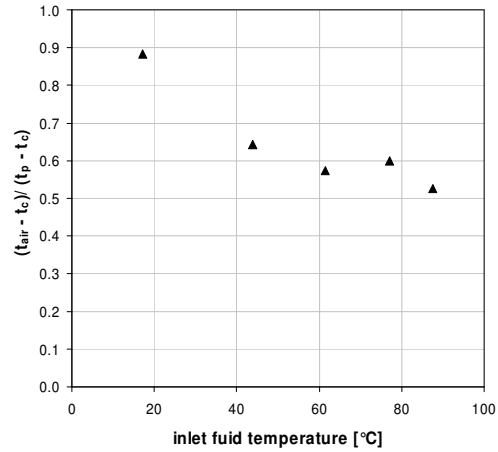

Figure 4.26. Measured air temperature between absorber plate and glass sheet.

Other tests have been done with an infrared camera at high fluid temperature, mainly to analyse the plate temperature between adjacent tubes in the middle of the collector and in the zone of the collector where the ultrasonic welding between plate and tube is interrupted.

In Figure 4.27 the result of the analysis in the zone where the ultrasonic welding is interrupted is shown; the picture shows two completely different temperature distributions, in the zone where the plate is welded to the tube and where the welding is interrupted. This analysis explains the model assumption: the control element welded to the plate (where switching function ϑ in Eq. (4.4) is equal to 1) and the control elements not welded (where switching function ϑ is equal to 0) have been considered separately. The upper zone (without welding) is hotter because the tubes don't directly remove the heat from the absorber sheet.

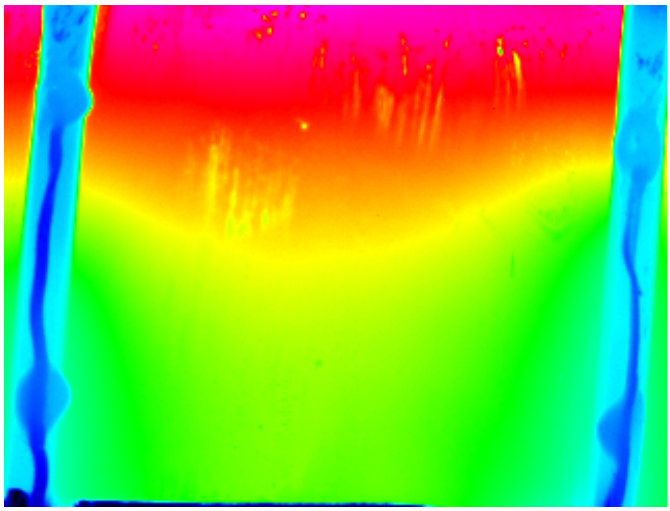

Figure 4.27. Infrared thermal analysis: absorber plate between two adjacent tubes where the welding between tube and plate is interrupted.

The solar collector efficiency considers two effects: the input power provided by the solar radiation and the heat losses to the ambient. To measure the heat losses, experimental tests without solar radiation have been performed, in night conditions. In these conditions the outlet temperature is lower than the inlet temperature and the collector works to dissipate heat. The results obtained by these tests are reported in Figure 4.28 where they are compared to the corresponding values obtained by the model at the same test conditions. In this graph the heat losses are reported vs. the temperature difference between the working fluid in the collector and the ambient air.

The heat loss investigation without solar radiation is in agreement with the results obtained from the efficiency tests and it denotes a small underestimations in the overall collector heat loss where the difference temperature $(t_m - t_a)$ is higher.

This conclusion is coherent with the temperature profile shown in Figure 4.16 and 4.18, where the estimated temperatures are higher than the measured temperatures. These results could mean underestimation in the overall collector heat loss, or

underestimation in the heat transfer coefficient between absorber plate and working fluid but this last conclusion is not consistent with the efficiency curve reported in Figure 4.14, because an higher heat transfer coefficient at high values of reduced temperature difference T_m^*, means higher estimated efficiency and this has not been obtained by experimental results.

The efficiency curve comparison between estimated and measured efficiency shows that the efficiency curve deviation is below 4.5% in the analysed temperature range between 0 and 0.07 m^2K/W. This deviation is lower than the experimental efficiency uncertainty in a wide range of the considered conditions.

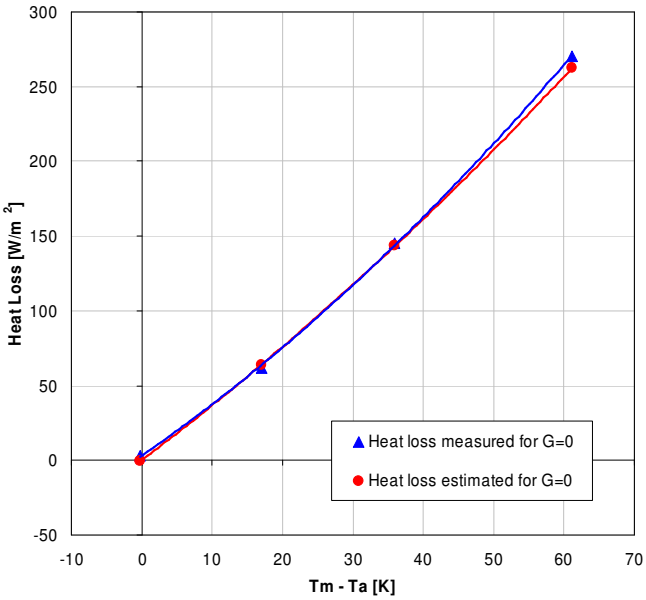

Figure 4.28. Measured and estimated heat losses in the collector at varying fluid temperatures during night (without solar radiation).

4.3.2 Second validation phase: collector with aluminium absorber plate

In a second phase, test measurements have been performed in a flat-plate collector with aluminium absorber plate.

The tested collector is based on a commercial solar collector where the copper sheet and tubes are replaced by plate and tubes in aluminium to reduce the product cost. In the selective absorber plate are welded (ultrasonic welding) 10 parallel tubes connected together by two manifolds.

The collector heat losses are reduced by a low-iron glass cover and back mineral wool board insulation. The collector housing is composed by lateral frames and an

aluminium back sheet. In Figure 4.29 is shown the collector installed in the test plant and in Table 4.4 are reported its main characteristics.

Figure 4.29. Tested collector.

Table 4.4. Characteristics of the tested collector (second case).

Aperture surface [m^2]	2.019
Absorber length [m]	1.804
Absorber width [m]	1.000
Tilt angle [°]	30 and 45
Number of flow channels in parallel	10
Spacing between tubes, *w* [m]	0.091
Internal tube diameter [m]	0.007
Absorber plate thickness, δ[mm]	0.30
Back insulation thickness [m]	0.03
Glass cover thickness [m]	0.0032
Cover-plate distance [m]	0.0025
Trasmittance-absorptance product at normal incidence $(\tau\alpha)_{en}$	0.886
Absorber emittance, ε	0.05

4.3.2.1 Experimental tests and results

In this section is reported the comparison between the efficiency curve measured in steady-state conditions on the tested collector and the predicted curve obtained from the simulation of a virtual solar collector with the same geometrical and physical characteristics (reported in Table 4.4).

The model validation in this phase is based exclusively on the comparison of the global performances given by the efficiency curve.

The experimental results obtained by the steady-state tests are reported in Figure 4.30. The measured efficiency curve is validated comparing it with results obtained by quasi-dynamic method.

In Figure 4.31 the estimated efficiency curve by the model is compared with the experimental steady-state curve. The comparison between the theoretical predictions and the experimental data shows that the efficiency curve deviation is below 5% in the reduced temperature range between 0 and 0.06 m^2K/W; the coefficient values related to these two curves are reported in Table 4.5.

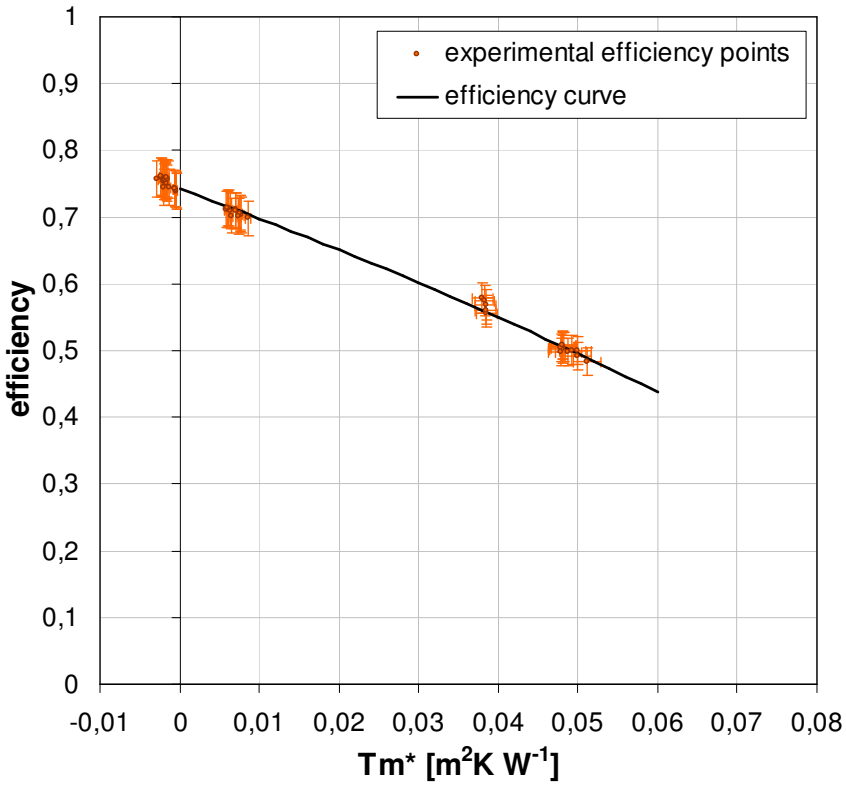

Figure 4.30. Experimental efficiency points and efficiency curve obtained by steady-state tests at G=1000 W/m^2.

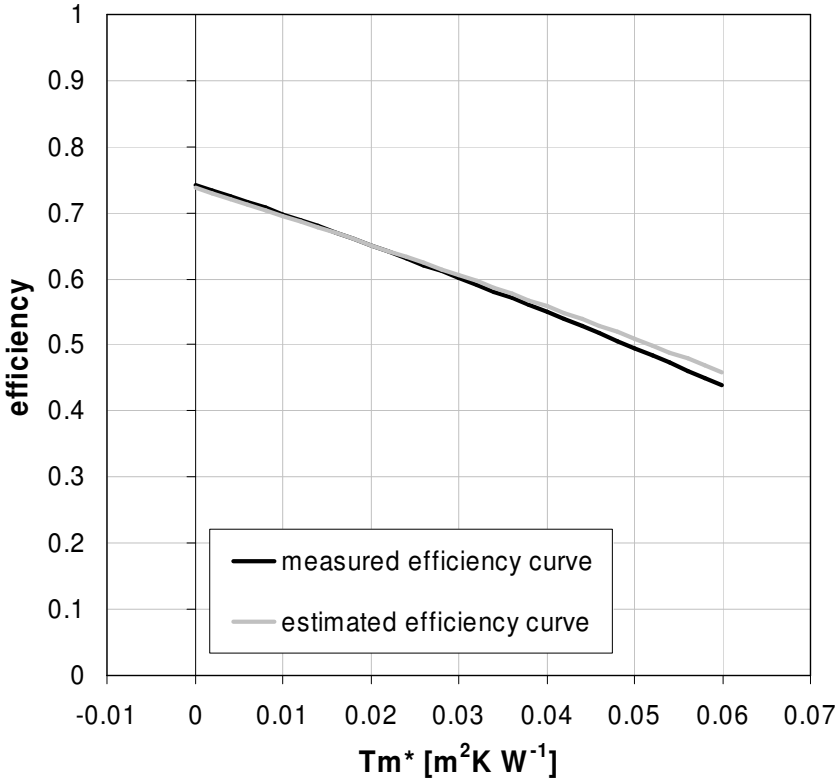

Figure 4.31. Measured and predicted efficiency curves at G=1000 W/m^2.

Table 4.5. Calculated and measured collector coefficients obtained by steady-state method for the tested collector (second case).

Coefficient	η_0 [-]	c_1 [W/(m^{2}K)]	c_2 [W/(m^{2}K^2)]
Experimental value	0.743 ± 0.005	-4.338 ± 1.010	-0.012 ± 0.021
Estimated value	0.737	-4.089	-0.009

The efficiency test investigation denotes a small underestimations in the overall collector heat loss mostly where the difference temperature $(t_m - t_a)$ is higher.

This conclusion is coherent with the results reported in the Section 4.3.1.1.

Chapter 5.
Model simulations

5.1 Introduction

The flat-plate collector geometry is a simple geometry; it permits to absorb the solar incident radiation transferring the heat to the working fluid flowing through the tube grid minimizing the heat losses to the surrounding.

Numerical models permit to obtain virtual prototypes and provide information on the predicted performances. From this analysis it is possible to identify aspects that need improvement to optimize the flat-plate collector design and allow to analyse comparative effects of varying design choices, with regard to geometry and materials.

This analysis could allow to optimize the performance of the collector or to obtain information to reduce it cost.

In this chapter are reported the results obtained by the numerical model described in Chapter 4.

5.2 Configuration analysis

In this work has been analysed different configuration of the flat-plate collector geometry using the numerical model to obtain information on the effect of:

- different metal sheet used as absorber plate
- diameter and number of tubes (tube grid)
- tube connection: number of passes
- ultrasonic welding length
- posterior insulation

- reduced convection on the air gap between absorber plate and cover
- roll-bond geometry.

These cases are analyzed using as base geometry the virtual prototype described in Section 4.3.1.

The results are reported as predicted efficiency curve obtained in steady-state condition with a global irradiance G=1000 W/m^2 and a specific mass flow rate $\frac{\dot{m}}{A_a} = 0.02$ kg/(m^{2}s).

5.3 Copper and aluminium absorber plate

Most solar collectors available on the market today have a copper absorber plate. In fact the copper is characterized by a high thermal conductivity and it allows to obtain high collector performance, optimizing the fin heat transfer.

In recent years the price of copper has risen strongly and new solution are necessary to contain the collector cost. An alternative solution is the aluminium sheet.

In this section are reported the results obtained by the model simulations considering four cases:

Case 1. copper absorber plate: thickness δ_p=0.18 mm (reference case)

Case 2. aluminium alloy absorber plate: thickness δ_p=0.18 mm

Case 3. aluminium alloy absorber plate: thickness δ_p=0.30 mm

Case 4. aluminium alloy absorber plate: thickness δ_p=0.50 mm.

Only material and thickness of the absorber sheet are varied in these analyses. The other characteristics are kept constant.

Cases 3 and 4 are considered because the aluminium suppliers provide these solutions for ordinary aluminium sheets.

In Table 5.1 are reported the predicted efficiency values obtained for the considered cases. In Figure 5.1 are reported the related efficiency curves.

Table 5.1. Predicted efficiency values for copper and aluminium absorber plate.

T_m^* [$m^2K\ W^{-1}$]	Efficiency [-] Case 1	Efficiency [-] Case 2	Efficiency [-] Case 3	Efficiency [-] Case 4
-0.0005	0.756	0.731	0.750	0.762
0.009	0.717	0.692	0.711	0.723
0.019	0.680	0.655	0.674	0.686
0.029	0.650	0.625	0.644	0.656
0.039	0.605	0.580	0.599	0.610
0.048	0.558	0.534	0.552	0.563
0.058	0.509	0.487	0.504	0.514
0.068	0.458	0.438	0.453	0.463

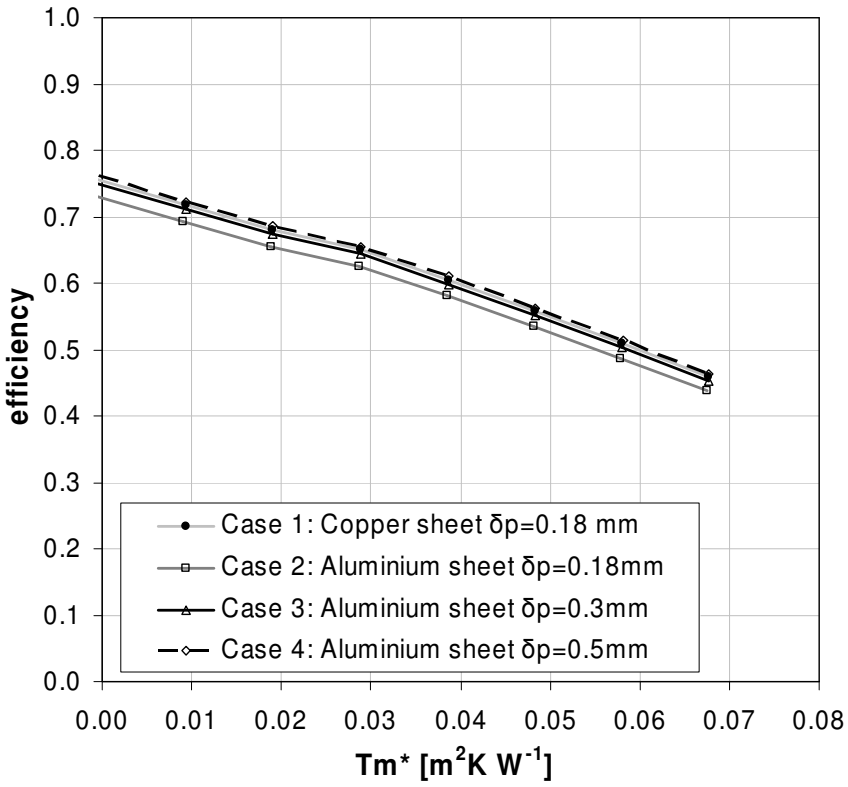

Figure 5.1. Predicted efficiency curves for copper and aluminium absorber plate.

It results that the considered copper absorber plate with δ_p=0.18 mm is equivalent (in term of collector efficiency curve) to an aluminium absorber plate with thickness δ_p≈0.40 mm.

5.4 Diameter and number of tubes

An alternative solution to reduce the collector cost could be to reduce the number or the diameter of the tubes composing the tube grid. These solutions involve also a variation on the pressure drops of the solar collector. In this work this effect is not accounted for.

In the first phase are reported the results obtained by the model simulations considering three cases:

Case 1. single pass, 12 tubes, internal diameter d=7 mm (reference case)

Case 2. single pass, 12 tubes, internal diameter d=5 mm

Case 3. single pass, 12 tubes, internal diameter d=9 mm.

Only the internal diameter is varied in this analysis. The other characteristics are kept constant.

In Table 5.2 are reported the predicted efficiency values obtained for the considered cases. In Figure 5.2 are reported the related efficiency curves.

Table 5.2. Predicted efficiency values for different tube diameter.

T_m^* [$m^2K\ W^{-1}$]	Efficiency [-] Case 1	Efficiency [-] Case 2	Efficiency [-] Case 3
-0.0005	0.752	0.751	0.754
0.009	0.714	0.712	0.716
0.019	0.673	0.671	0.675
0.029	0.630	0.628	0.632
0.039	0.585	0.584	0.587
0.048	0.539	0.554	0.540
0.058	0.490	0.506	0.492
0.068	0.441	0.455	0.442

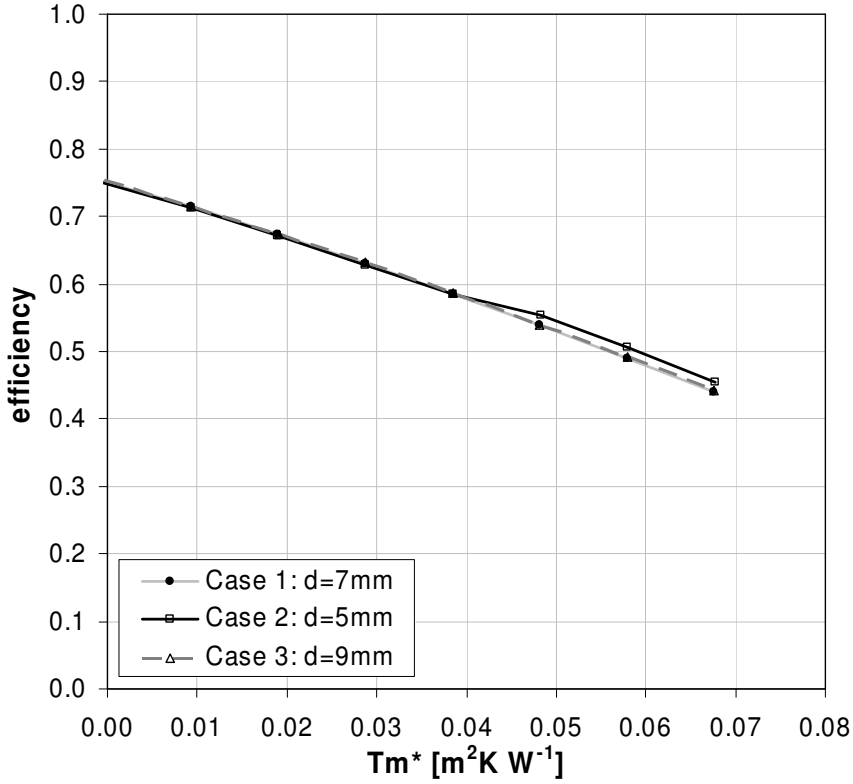

Figure 5.2. Predicted efficiency curves for different tube diameter.

The estimated results show an efficiency increase at about T_m^*=0.045 m^{2}K/W for the case with d=5mm. It is due to the laminar-turbulent transition and the efficiency increase is about 3% in the considered range of condition. So the same effect could be obtained increasing the mass flow rate in the Case 1: this conclusion has been justified because only the convective heat transfer coefficient for fluid inside tubes h_f strongly varies in the considered cases.

In the second phase are considered the effect on the collector performance varying the number of the tubes of the tube grid. This characteristic has a heavier effect than the tube diameter on the collector cost. Five cases are considered:

Case A. single pass, 12 tubes, internal diameter d=7 mm (reference case)

Case B. single pass, 8 tubes, internal diameter d=7 mm

Case C. single pass, 10 tubes, internal diameter d=7 mm

Case D. single pass, 14 tubes, internal diameter d=7 mm

Case E. single pass, 16 tubes, internal diameter d=7 mm.

Only the number of tubes is varied in this analysis. The other characteristics are kept constant.

In Table 5.3 are reported the predicted efficiency values obtained for the considered cases. In Figure 5.3 are reported the related efficiency curves.

Table 5.3. Predicted efficiency values for different number of tube.

T_m^* [$m^2K\ W^{-1}$]	Efficiency [-] Case A	Efficiency [-] Case B	Efficiency [-] Case C	Efficiency [-] Case D	Efficiency [-] Case E
-0.0005	0.752	0.710	0.737	0.762	0.769
0.009	0.714	0.672	0.698	0.724	0.731
0.019	0.673	0.632	0.658	0.683	0.689
0.029	0.630	0.591	0.615	0.639	0.646
0.039	0.585	0.554	0.571	0.594	0.600
0.048	0.539	0.524	0.526	0.547	0.552
0.058	0.490	0.478	0.490	0.498	0.504
0.068	0.441	0.431	0.446	0.448	0.453

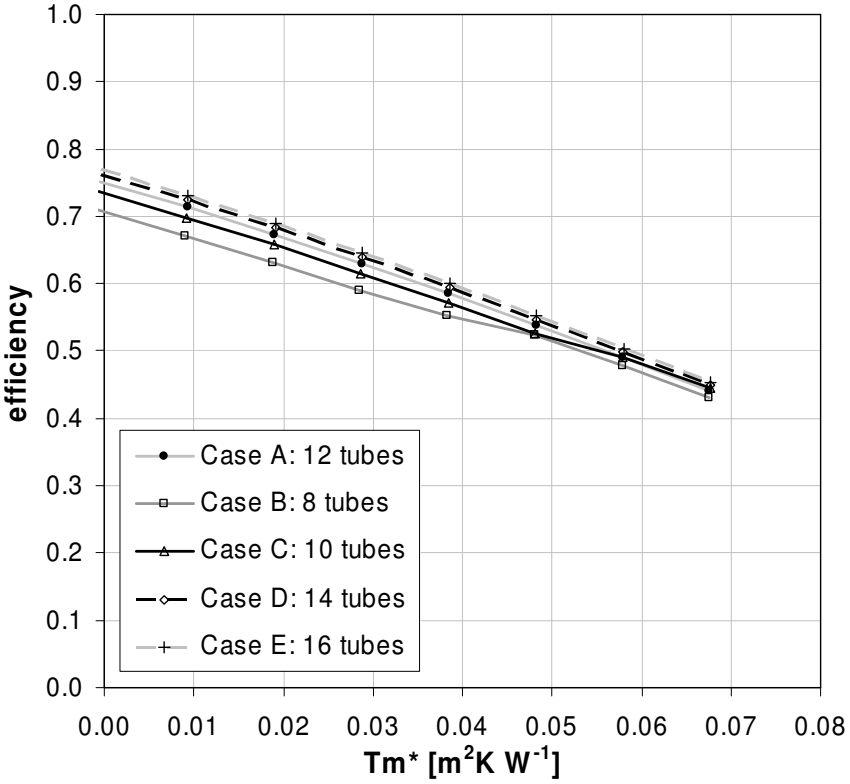

Figure 5.3. Predicted efficiency curves for different number of tube.

Different number of tubes in the same absorber plate gives different distance between tubes (*w* in Figure 4.5) and different mass flow rate flowing through the tube.

In Figure 5.3 is shown the effect on the collector efficiency caused by different number of tube in the same collector. In the considered cases the solution with 10 or 8 tubes gives a remarkable efficiency lowering mostly for T_m^*<0.040 m^2K/W where the laminar flow inside the tubes is verified (about -2% and -6% respectively) related to the reference case (12 tubes). Instead the solution with 14 or 16 tubes gives a small efficiency increase (about 1.5% and 2.5% respectively) related to the reference case (12 tubes).

5.5 Number of passes

In this section are described the efficiency effect varying the number of passes. Varying the number of passes is possible to optimize the collector performances. In the market are present collectors with one or two passes, or with serpentine solution. The analysed case (12 tubes) makes it possible to obtain six different cases:

Case 1. single pass, parallel solution (reference case)

Case 2. 2 passes

Case 3. 3 passes

Case 4. 4 passes

Case 5. 6 passes

Case 6. 12 passes, equivalent to serpentine solution.

In this analysis the other collector characteristics are kept constant.

In Table 5.4 the predicted efficiency values are reported and in Figure 5.4 the related efficiency curves are shown.

Table 5.4. Predicted efficiency values for different number of passes.

T_m^* [$m^2K\ W^{-1}$]	Efficiency [-] Case 1	Efficiency [-] Case 2	Efficiency [-] Case 3	Efficiency [-] Case 4	Efficiency [-] Case 5	Efficiency [-] Case 6
-0.0005	0.752	0.756	0.764	0.777	0.779	0.782
0.009	0.714	0.717	0.737	0.739	0.741	0.743
0.019	0.673	0.679	0.696	0.698	0.700	0.702
0.029	0.630	0.650	0.653	0.654	0.656	0.658
0.039	0.585	0.605	0.608	0.609	0.611	0.613
0.048	0.539	0.558	0.561	0.562	0.564	0.566
0.058	0.490	0.509	0.513	0.513	0.515	0.517
0.068	0.441	0.458	0.462	0.463	0.464	0.466

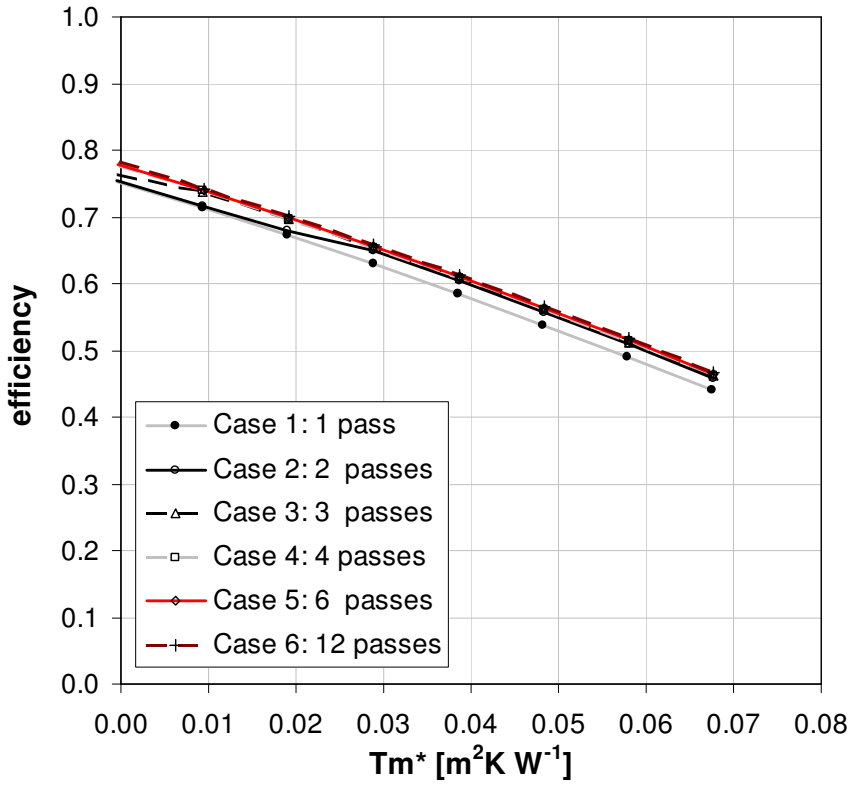

Figure 5.4. Predicted efficiency curves for different number of passes.

From this analysis it results that the solutions with 4, 6 passes and serpentine are equivalent (efficiency difference between them about 0.5%). The efficiency increase shown in Figure 5.4 is mostly due to the laminar-turbulent transition and this rise is about 4÷6% from the Cases 1 to the Case 6 in the considered range of condition.

The same effect could be obtained increasing the mass flow rate in the Case 1, in fact only the convective heat transfer coefficient for fluid inside tubes h_f strongly varies in the considered cases.

5.6 Welding length

In all the considered cases the welding length L_b has been fixed to a constructive value smaller than the absorber plate and tube lengths $L_b<L$.

In this analysis it is also considered two cases where the welding length is fixed equal to the tube length $L_b=L$ (ideal case) for the case with single pass and serpentine. The predicted efficiencies are reported in Table 5.5 and in Figure 5.5.

Table 5.5. Predicted efficiency values for $L_b=L$.

T_m^* [$m^2K\ W^{-1}$]	Efficiency [-] 1 pass	Efficiency [-] serpentine	Efficiency [-] 1 pass $L_b=L$	Efficiency [-] serpentine $L_b=L$
0.000	0.752	0.800	0.782	0.843
0.009	0.714	0.759	0.743	0.800
0.019	0.673	0.714	0.702	0.755
0.029	0.630	0.668	0.658	0.706
0.039	0.585	0.620	0.613	0.656
0.048	0.539	0.571	0.566	0.603
0.058	0.490	0.520	0.517	0.549
0.068	0.441	0.467	0.466	0.493

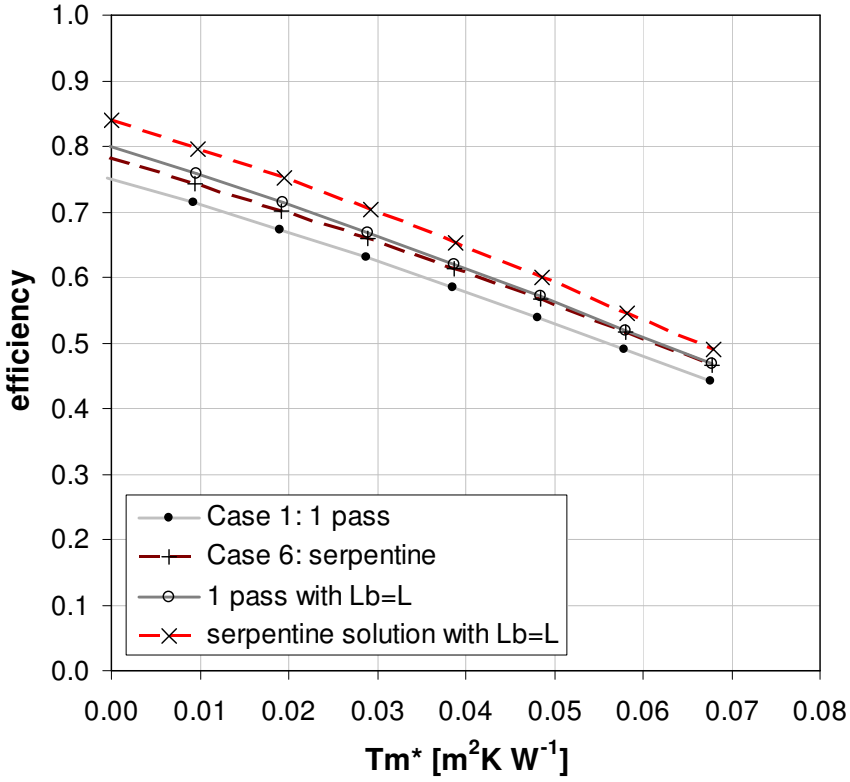

Figure 5.5. Predicted efficiency curves for L_b=L.

Increasing the welding length it is possible to increase the collector performance reducing the zone where the absorber plate is not directly bonded to the tubes. In the two cases (single pass and serpentine) the efficiency increase is about 6÷8% increasing the welding length.

5.7 Back insulation

The posterior insulation is a main component of the thermal solar collector and it reduces the thermal losses in the back side of the solar collector.

In this phase are obtained the effect of the back insulation thickness on the collector performance. The following cases are considered:

Case 1. thickness of the back board insulation s_b=40 mm (reference case)

Case 2. thickness of the back board insulation s_b=25 mm

Case 3. thickness of the back board insulation s_b=55 mm

Case 4. thickness of the back board insulation s_b=70 mm.

Also in this analysis the other collector characteristics are kept constant.

In Table 5.6 are reported the predicted efficiency values and in Figure 5.6 are shown the related efficiency curves.

Table 5.6. Predicted efficiency values for different back insulation thickness.

T_m^* [$m^2K\ W^{-1}$]	Efficiency [-] Case 1	Efficiency [-] Case 2	Efficiency [-] Case 3	Efficiency [-] Case 4
0.000	0.752	0.748	0.756	0.756
0.009	0.714	0.707	0.719	0.720
0.019	0.673	0.663	0.680	0.682
0.029	0.630	0.617	0.639	0.641
0.039	0.585	0.569	0.597	0.599
0.048	0.539	0.520	0.553	0.555
0.058	0.490	0.469	0.507	0.510
0.068	0.441	0.416	0.461	0.464

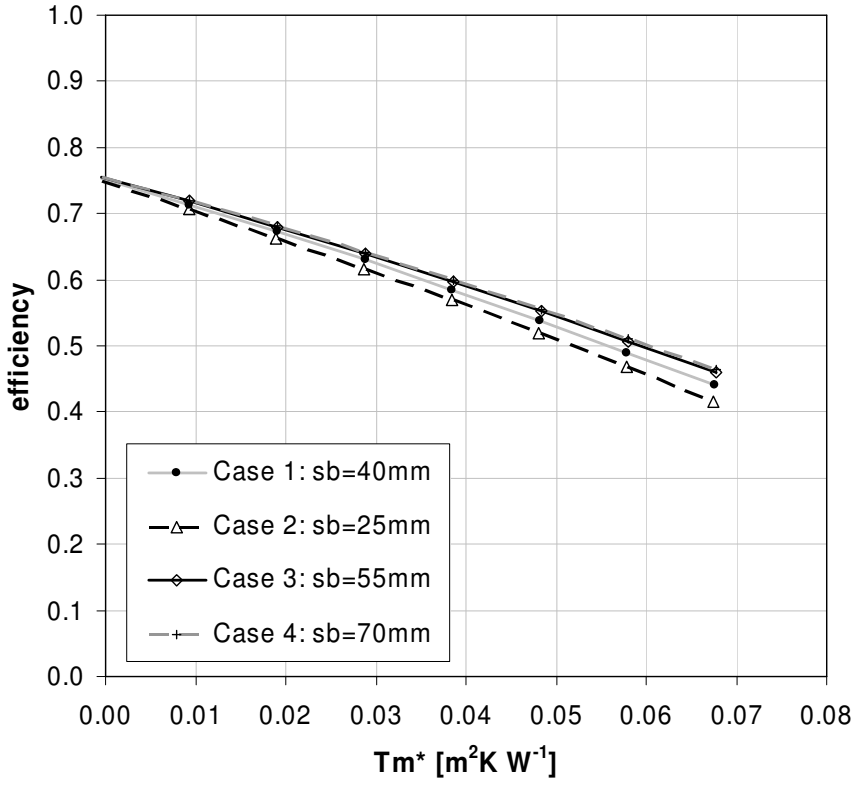

Figure 5.6. Predicted efficiency curves for different back insulation thickness.

From the efficiency curves reported in Figure 5.6 it is possible to observe that the back insulation thickness influences only the inclination of the efficiency curve, without remarkable effect on the optical collector efficiency η_0.

In Figure 5.6 are shown the efficiency advantage obtained in the cases 3 and 4 (equivalent). In these cases the conductive heat transfer in the back side of the collector and so the overall heat loss coefficient of the collector are reduced: the efficiency difference between case 1 (reference case) and cases 3 and 4, is about 5% at T_m^*=0.068 m^2K/W.

5.8 Reduced convection in the air gap between absorber plate and cover

After a deeper examination it has been verified that the convective heat transfer coefficient between absorber plate and glass cover is an important term mostly where a selective absorber coating is used. Its effects on the collector performance are considerable as shown in Figure 5.7 where are reported the efficiency curve in three cases:

Case 1. reference case with $h_{Conv\_p\text{-}c}$ calculated as described in Sect. 4.2.3.

Case 2. $h_{Conv\_p\text{-}c}$ halved respect Case 1

Case 3. $h_{Conv\_p\text{-}c}$=0.

The third case described the performances of a flat-plate collector with vacuum zone between absorber plate and cover. The efficiency curve in exam is characterizes by reduced heat loss coefficients a_1=1.35 W/(m^2K) and a_2=0.007 W/(m^2K^2) defined in Eq. (1.4). These values are coherent to the heat loss coefficients for an evacuated tube collector (vacuum zone between internal and external tubular glasses); an example for these parameters in the case of evacuated tube collector is reported in Sect. 3.4.2.

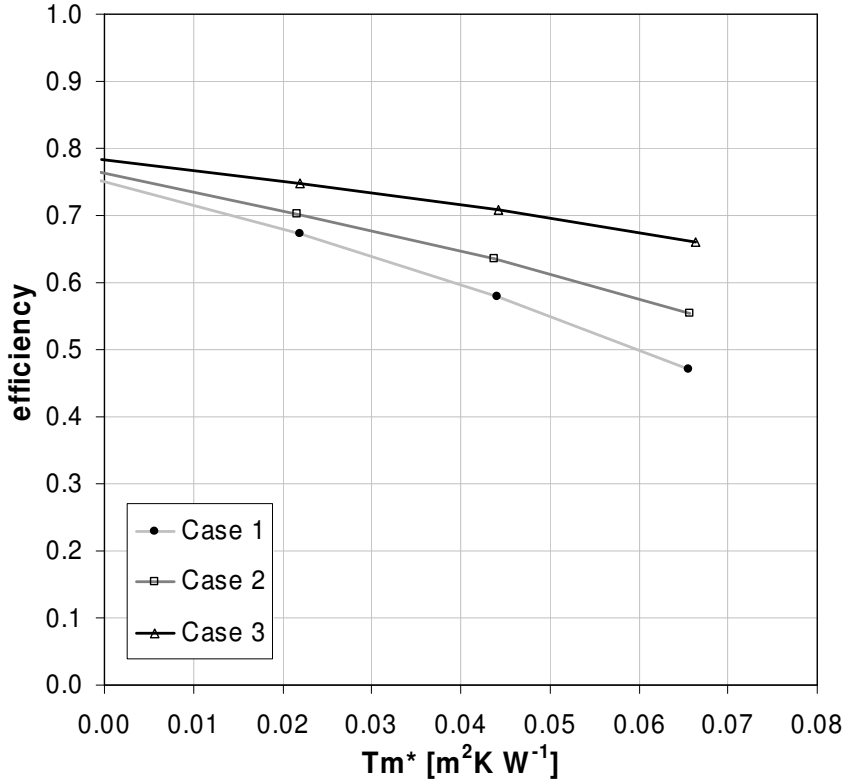

Figure 5.7. Predicted efficiency curves for different convective heat transfer coefficients.

In Figures 5.8 and 5.9 are reported the radiative, convective and overall heat transfer coefficient as functions of $s_{p\text{-}c}$, distance between absorber plate and cover, at inlet fluid temperature t_{in}=20°C and t_{in}=87.5°C respectively.

The radiative heat transfer coefficient $h_{Rad\_p\text{-}c}$ is constant varying $s_{p\text{-}c}$, instead the convective heat transfer coefficient $h_{Conv\_p\text{-}c}$ has a more complicated trend, with a local minimum in $s_{p\text{-}c}$=0.01 m and a local maximum in $s_{p\text{-}c}$=0.02 m. This trend is not dependent on the temperature of the working fluid.

From the curves reported in Figure 5.7 we can conclude that the convective heat transfer coefficient has a strongly effect on the collector efficiency so it has been examined some possible solution to reduce the convective thermal losses.

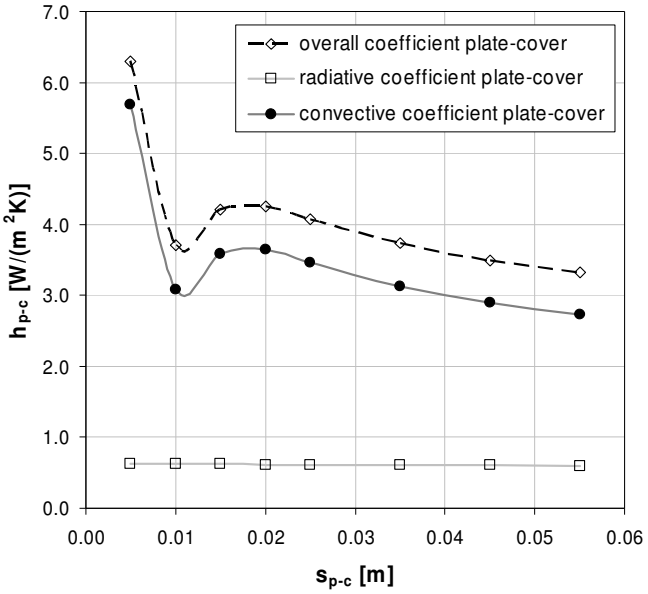

Figure 5.8. Heat transfer coefficient between plate and cover at the inlet fluid temperature t_{in}=20°C.

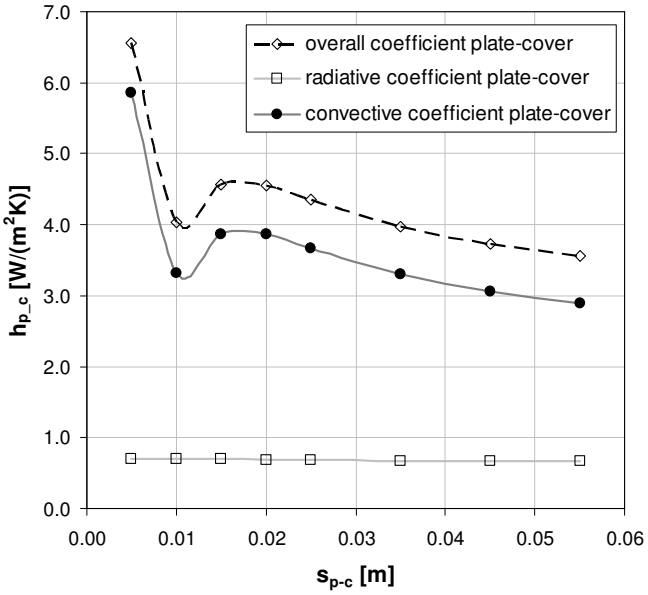

Figure 5.9. Heat transfer coefficient between plate and cover at the inlet fluid temperature t_{in}=87.5°C.

The first solution could be to choose a different distance $s_{p\text{-}c}$ between plate and cover; the following cases are considered:

Case A. reference case with $s_{p\text{-}c}$=0.025.

Case B. $s_{p\text{-}c}$=0.010

Case C. $s_{p\text{-}c}$=0.015

Case D. $s_{p\text{-}c}$=0.035

Case E. $s_{p\text{-}c}$=0.045

Case F. $s_{p\text{-}c}$=0.055.

The other collector characteristics are kept constant. In Table 5.7 are reported the predicted efficiency for the six cases and in Figure 5.10 are reported the more characteristic efficiency curves.

Table 5.7. Predicted efficiency values for different distance between plate and cover.

T_m^* [$m^2K\ W^{-1}$]	Efficiency [-] Case A	Efficiency [-] Case B	Efficiency [-] Case C	Efficiency [-] Case D	Efficiency [-] Case E	Efficiency [-] Case F
0.000	0.752	0.754	0.757	0.755	0.756	0.757
0.009	0.714	0.720	0.719	0.719	0.721	0.722
0.019	0.673	0.685	0.679	0.680	0.683	0.685
0.029	0.630	0.648	0.637	0.640	0.644	0.646
0.039	0.585	0.608	0.592	0.598	0.603	0.605
0.048	0.539	0.566	0.545	0.554	0.559	0.563
0.058	0.490	0.521	0.496	0.508	0.515	0.519
0.068	0.441	0.474	0.446	0.461	0.469	0.474

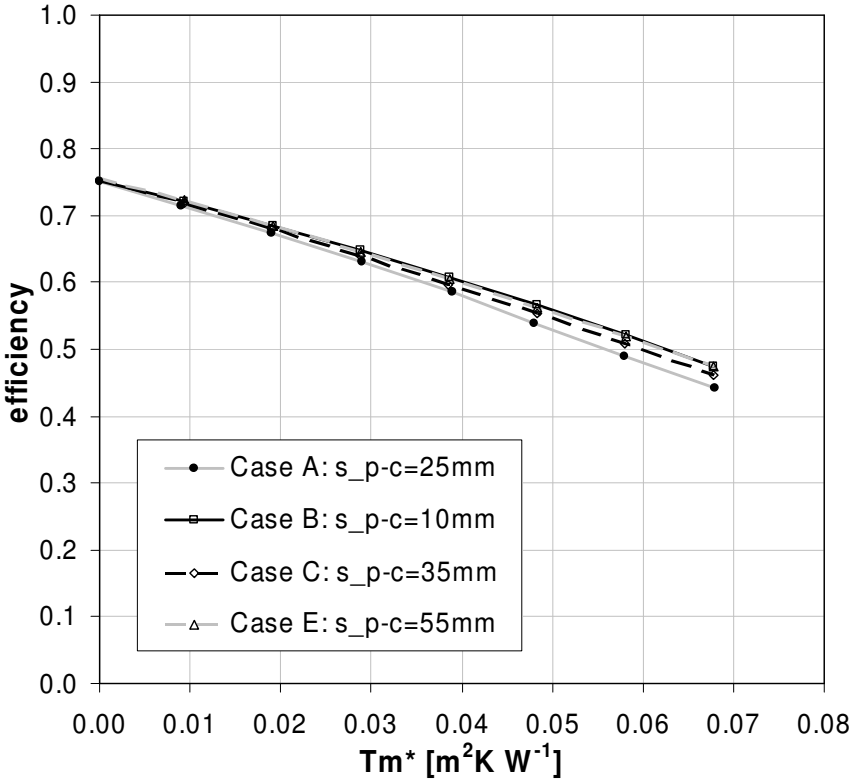

Figure 5.10. Predicted efficiency curves for different distance $s_{p\text{-}c}$ between plate and cover.

From this analysis it is possible to conclude that the convective heat transfer between absorber plate and cover is minimised for $s_{p\text{-}c}$=0.01 m or for $s_{p\text{-}c}$>0.035 m. Similar efficiency are noticed in these cases: the first solution is a local minimum so slightly variation of $s_{p\text{-}c}$ (possible in the collector assembly) can caused remarkable variation in efficiency, as shown in Figures 5.8 and 5.9; the second solution is related to a global minimum in Figures 5.8 and 5.9 so it is a preferable solution.

Another solution to reduce the convective thermal losses could be to apply convective transversal barrier between absorber sheet and cover. To simulate this case the model suggested by Hollands et al. (1976) described in Eq. (4.13) has been substituted by the model suggested by Meyer et al. and reported in Duffie and Beckman (2006) where the convective heat transfer coefficient is described as a function of the distance plate-cover $s_{p\text{-}c}$ and the distance between adjacent barriers s_{bar}.

Four cases are considered:

Case I. Holland et al. model without barrier

Case II. Meyer et al. model where s_{bar}>10$s_{p\text{-}c}$

Case III. Meyer et al. model where $s_{p-c}<s_{bar}<3s_{p-c}$

Case IV. Meyer et al. model where $s_{bar}=0.25s_{p-c}$.

The other collector characteristics are kept constant. In Table 5.8 are reported the predicted efficiency values and in Figure 5.11 are shown the related efficiency curves.

Table 5.8. Predicted efficiency values for different distance between transversal barrier s_{bar}.

T_m^* [$m^2K\ W^{-1}$]	Efficiency [-] Case I	Efficiency [-] Case II	Efficiency [-] Case III	Efficiency [-] Case IV
-0.0005	0.752	0.756	0.750	0.763
0.009	0.714	0.720	0.710	0.732
0.019	0.673	0.681	0.667	0.700
0.029	0.630	0.641	0.622	0.665
0.039	0.585	0.598	0.574	0.629
0.048	0.539	0.554	0.525	0.592
0.058	0.490	0.508	0.474	0.553
0.068	0.441	0.461	0.422	0.512

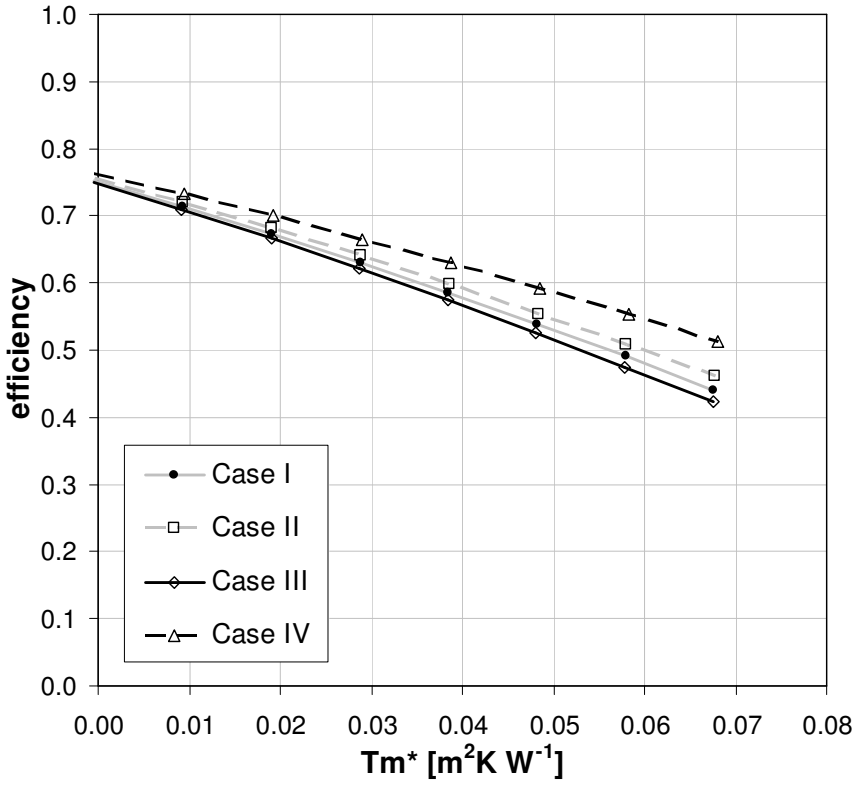

Figure 5.11. Predicted efficiency curves for different distance between transversal barrier s_{bar}.

Cases II, III and IV do not consider all the possible distance s_{bar} but describe the more characteristic cases.

In Figure 5.11 are shown the efficiency advantage obtained in the case IV, where s_{bar}=0.25$s_{p\text{-}c}$. In this case the convective heat transfer coefficient and so the overall heat loss coefficient of the collector are strongly reduced: the efficiency increase between case II (reference case in this comparison) and IV, is about 11% at T_m^*=0.068 m^{2}K/W.

However the solution described in case IV is not realistic because, being $s_{p\text{-}c}$=25 mm in the considered simulation, the distance between barrier is too little, in fact s_{bar}=6.25 mm.

In this analysis the corrugation effect on the convection losses are studied. The last solution considered in this analysis is the use of vee-corrugated absorber plate. The corrugations have been proposed for solar collectors to improve the radiative characteristics.

The Randall model, reported in Duffie and Beckman (2006) has been used to simulate the convective heat transfer in this solution with the corrugations running horizontally.

Considering the characteristic dimensions in Figure 5.12 four cases are considered:

Case a. Flat absorber plate (reference case)

Case b. Vee-corrugated absorber plate $s_{p\text{-}c}/h_c$=2

Case c. Vee-corrugated absorber plate $s_{p\text{-}c}/h_c$=1

Case d. Vee-corrugated absorber plate $s_{p\text{-}c}/h_c$=0.75.

In Figure 5.13 are reported the efficiency curve obtained in these cases.

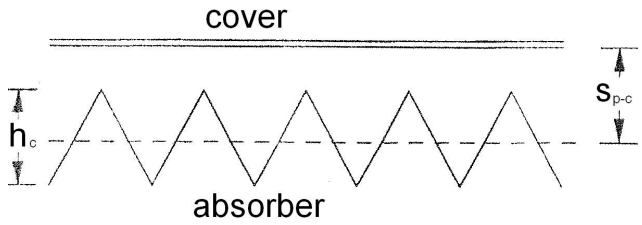

Figure 5.12. Characteristic dimensions of vee-corrugated absorber plate.

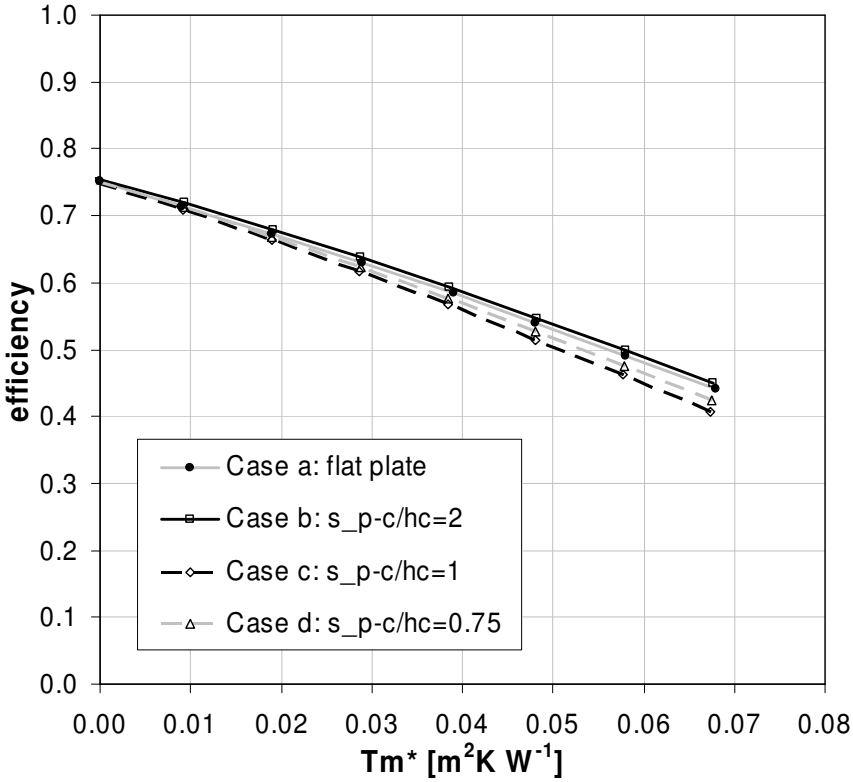

Figure 5.13. Predicted efficiency curves for vee-corrugated absorber plate.

Small corrugations (low h_c dimension) have negligible effects on the collector heat losses; if $h_c > s_{p\text{-}c}$ the convective heat transfer between plate and cover increases and the effect on the collector heat losses are considerable.

5.9 Roll-bond geometry

The roll-bond is an absorber plate composed by two aluminium sheets bonded together by means of heating procedure pressing them at high pressure. The flow channels are obtained between the sheets inflating a trace where the plates are not bonded.

In this geometry the absorber plate and the tubes grid are obtained in the same component. It allows to easily obtain geometries with different length and number of flow channels and passes.

A realistic case is considered in this analysis; the main characteristics of the sample analysed are reported in Table 5.9 and the collector efficiency obtained by the numerical

simulation is show in Figure 5.14 where is reported also the predicted efficiency curve for the standard collector reported in the previous sections as reference case.

Two roll-bond cases are considered: the first one with selective surface characteristics equal to the reference case and the second one with a semi-selective surface as provided by the manufacturer.

In Figure 5.14 is show the advantage of this solution; in the cases with equal selective characteristics the efficiency increase is about 6÷9% in the considered range.

Table 5.9. Characteristics of the considered collector with roll-bond absorber plate.

Aperture surface [m^2]	2.019	
Absorber length [m]	1.955	
Absorber width [m]	1.092	
Tilt angle [°]	45	
Number of flow channels in parallel	28	
Internal tube diameter [m]	0.0044	
Absorber plate thickness, δ[mm]	1.5	
Back insulation thickness [m]	0.04	
Glass cover thickness [m]	0.0032	
Cover-plate distance [m]	0.0025	
Absorber absorptance α	0.95	0.91
Absorber emittance, ε	0.04	0.34

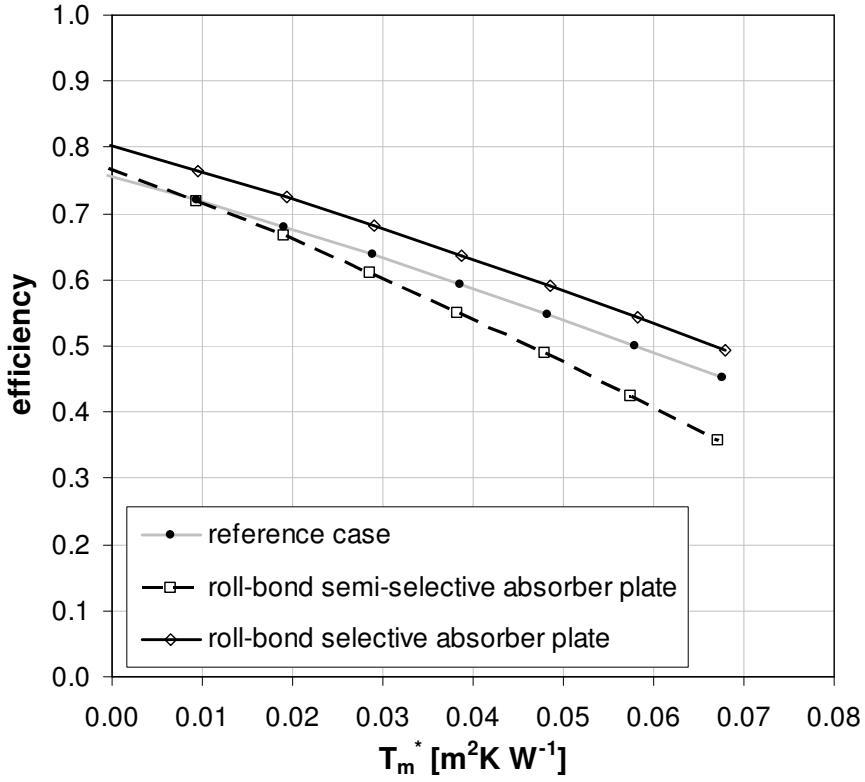

Figure 5.14. Predicted efficiency curves for collector with roll-bond absorber plate.

Chapter 6.

A new procedure for the experimental characterization of evacuated tube collectors

6.1 Introduction

Performance of a thermal solar collector can be increased by reducing the heat losses toward the external ambient reducing the radiative and convective heat transfer between absorber surface and ambient.

The peculiar design of the evacuated tube collector geometry with double glass tube allows the use of absorber tubes coated with a selective surface arranged concentrically with a transparent outer glass envelope and with the annular region evacuated. This provides outstanding thermal insulation by suppressing internal conductive, convective and radiative losses.

The evacuated tube collector shape is optically non-symmetric. In the case of tubular collectors, with concentrators or reflectors, their geometry makes more difficult to determine the specific power which irradiates the absorber surfaces as compared to the case of flat-plate collector.

In the case of an evacuated tubular collector with diffuse back reflector this analysis has been done in Cabanillas et al. (1995) where experimental measurements of the radiation distribution in the evacuated tube have been performed. This case is also studied in Chow et al. (1984) and in Theunissen and Beckman (1985) where the angular dependence of the glass transmittance and the optical efficiency were studied.

In this work the performance of an evacuated tube collector with CPC reflectors is analysed comparing it with the results obtained without reflectors for the same geometry. In this chapter the effects of this type of reflectors are presented. The same reflector geometry is also considered in the work described in Grass et al. (2004) and in Carvalho et al. (1995) where the CPC is applied to another absorber shape.

The analysis here discussed is based on experimental results reported as efficiency curves and incidence angle modifier (IAM) curves obtained from different test methods. These tests have been performed following the European Standard EN 12975 (2006).

The EN 12975 (2006) describes two test methods to determine the thermal performance of liquid heating solar collectors: the steady-state method and the quasi-dynamic method. This last method allows a much more complete characterisation of the tested collector, but it is not directly applicable to the case of evacuated tube collectors (Zambolin and Del Col, 2010).

In this work a new model for the transversal incident angle modifier for evacuated tube collectors is presented and its application in the quasi-dynamic model is described.

As a comparative tool, another procedure has been used to validate the present technique: the extended multiple linear regression (MLR). This method is described in Perers (1997) and it makes possible to identify the optical efficiency (efficiency at $T_m^*=0$) for specific incidence angle intervals. Here, the values of the transversal incident angle modifier provided by the extended MLR are compared to the corresponding results obtained from the application of the new transversal incident angle modifier model applied to the quasi-dynamic method.

6.2 Experimental tests and collector

The experimental apparatus is described in Chapter 2.

The tested collector is a direct flow type U-tube collector, north-south aligned cylindrical absorber, composed by 20 tubular glasses, with external CPC (compound parabolic concentrator) reflectors that can be taken apart. Geometrical characteristics are reported in Table 1. The collector is oriented 10° south-west and it is possible to vary the tilt angle.

Table 6.1. Characteristics of the tested collector.

Aperture surface [m2]	3.44
Collector length [m]	1.730
Collector width [m]	2.212
Collector thickness [m]	0.145
Absorber surface [m2]	4.43
Number of flow channels in parallel and glass tubes	20
Internal flow channel diameter [m]	0.0063
External glass tube diameter [m]	0.058
Glass thickness [m]	0.0016
Thickness of the absorber profile inside the glass tube [mm]	0.8
Glass trasmittance	> 0.90
Coating emittance, ε	< 0.07
Coating absorptance	> 0.94
Vacuum pressure [Pa]	<0.003

In Figures 6.1 and 6.2 the pictures of the tested collector are reported, respectively with CPC reflectors and without them. In the case without CPC reflectors, a black cloth has been placed on the back of the collector to minimize the reflections from the back side.

The glass tubes are evacuated double glass tubes and the selective coating is deposed on the external surface of the internal tube, in the vacuum zone.

The following measurements have been acquired: global and diffuse irradiance on the collector plane, inlet and outlet fluid temperature in the collector, surrounding air temperature and fluid flow rate. The surrounding air speed has been measured on the side of the test rig.

Both the global and diffuse irradiance are measured on the collector plane. The diffuse irradiance is measured by means of a pyranometer with a shading band (Padovan and Del Col, 2010).

Tests have been done to characterize the evacuated tubular collector with and without CPC reflectors and the results obtained from the regression methods are used to compare different methods for the transversal incidence angle modifier estimation.

Figure 6.1. Evacuated tube collector installed in the apparatus with CPC reflectors.

Figure 6.2. Evacuated tube collector installed in the apparatus without CPC reflectors.

The data have been acquired following the standard EN 12975 (2006) guidelines for the quasi-dynamic tests and are then filtered to obtain performance data with required conditions. The required test conditions for the quasi-dynamic method are reported in Table 3.4.

The test period includes a pre-conditioning period of at least 10 minutes; instantaneous readings are acquired with a time step of 5 seconds and are reduced to calculate characteristic mean values for each time interval equal to 10 minutes.

Experimental tests for the collector with CPC reflectors were made from April to July 2010 in 11 test days, instead for the collector without CPCs were made in 22 different tests from May to September 2010. Tests were made for different tilt angle of the collector (30°, 45° and 60°) to obtain information for varying longitudinal incidence angles.

Different test conditions have been obtained varying the inlet fluid temperatures, from the ambient temperature to about 80°C.

6.3 Incidence angle modifier model

The effect of incidence angle of the direct incident radiation on the aperture collector area is described by the incidence angle modifier $K_{\theta b}$ defined as described in Chapter 1 by Eq. (1.6).

As reported in Chapter 3, for flat-plate collectors with flat covers, the angular dependence of the incidence angular modifier is given by Eq. (3.7), instead for evacuated tube collectors the incidence angle dependence can be described by Eq. (3.8).

For the computation of $K_{\theta t}$ and $K_{\theta l}$ two methods are applicable using a stationary test installation: a routine described in EN 12975 (2006) based on a steady-state method, where the results are obtained in fixed conditions, and the so called extended multiple linear regression in the quasi-dynamic method, also mentioned in EN 12975 (2006).

This last method is described in Perers (1997) and in the specific case it can accurately identify non-linear optical performances by dividing the space in transversal and longitudinal angle intervals (θ_t and θ_l) and providing an average value of $K_{\theta b}$ for each θ_t and θ_l angle interval; it allows the application of the quasi-dynamic method to collectors with incidence angle effects that cannot be easily described with a combination of elementary functions.

As described in Budihardjo and Morrison (2009) for a water-in-glass evacuated tube, the simple model reported in Eq. (3.7) can be used exclusively for the longitudinal angle modifier:

$$K_{\theta l} = 1 + b_0 \cdot \left(\frac{1}{\cos(\theta_l)} - 1 \right) \tag{6.1}$$

In this chapter an alternative method is presented. The angular dependence of the optical efficiency is assumed to follow a predetermined function also for the transversal incidence angle: $K_{\theta t}$ is described as a function of θ_t (a 4th order polynomial function) as reported in the following equation:

$$K_{\theta t} = 1 + b_1 \cdot \left(\frac{1}{\cos(\theta_t)} - 1 \right) + b_2 \cdot \left(\frac{1}{\cos(\theta_t)} - 1 \right)^2 + b_3 \cdot \left(\frac{1}{\cos(\theta_t)} - 1 \right)^3 + b_4 \cdot \left(\frac{1}{\cos(\theta_t)} - 1 \right)^4 \tag{6.2}$$

where b_1, b_2, b_3 and b_4 are parameters that can be obtained, together with b_0 for the longitudinal angle modifier, by the multiple linear regression.

This method has been applied in Zambolin and Del Col (2010), while a polynomial function of θ was used to fit the values of incidence angle modifier for parabolic trough collectors in Gaul and Rabl (1980).

This method is experimentally validated in the following.

6.4 Regression analysis for the determination of collector coefficients

The collector parameters are identified with the multiple linear regression (MLR) of the acquired data.

The basic equation of the solar thermal collector energy balance for the quasi-dynamic approach is reported in Eq. (3.6). It is here reported again:

$$\frac{\dot{Q}_{out}}{A_a} = F' \cdot (\tau\alpha)_{en} \cdot K_{\theta b} \cdot (\theta) \cdot G_b + F' \cdot (\tau\alpha)_{en} \cdot K_{\theta d} \cdot G_d - c_6 \cdot u \cdot G +$$
$$- c_1 \cdot (t_m - t_a) - c_2 \cdot (t_m - t_a)^2 - c_3 \cdot u \cdot (t_m - t_a) + c_4 \cdot \left(E_L - \sigma \cdot T_a^{\,4}\right) - c_5 \cdot dT_m / d\tau \qquad (6.3)$$

The coefficients c_6, c_3 and c_4 can be assumed to be without statistical significance for evacuated tube collectors, where the wind and the long-wave irradiance losses are neglected.

The first term of the right-hand side of Eq. (6.3) $F' \cdot (\tau\alpha)_{en} \cdot K_{\theta b}(\theta) \cdot G_b$ is the zero loss efficiency for beam radiation. Two methods are used in this work for the determination of this term:

- New procedure: in the first method this parameter is obtained through the energy balance reported in Eq. (6.3), the polynomial function in Eq. (6.2) for the transversal incidence angle modifier $K_{\theta t}$ and the Eq. (6.1) for the longitudinal modifier $K_{\theta l}$.
- Extended MLR: in the second procedure the extended multiple linear regression method (extended MLR) is applied. This method makes it possible to determine the incidence parameters in different subsets or ranges of the database. In this work it is used to determine the incidence transversal angle $K_{\theta t}$ at specific intervals of the incidence angle. The extended MLR method is described in detail in Perers (1997).

In this second procedure, the transversal incidence angle modifier is identified without defining an ad-hoc equation, whereas the function reported in Eq. (6.1) is used to describe the longitudinal angle modifier. The extended MLR is used with a resolution of 15°.

In Rönnelid et al (1997) the extended MLR is applied to the experimental data of a CPC collector considering angular intervals both in the longitudinal and transversal directions (twenty angular intervals were considered), without using any specific equation for the prediction of optical efficiency.

In the present work the multiple linear regression (MLR) is used to calculate the parameters c_i of Eq. (6.3) and their uncertainties uc_i, but also the coefficients of Eqs. (6.1) and (6.2). The multiple linear regression applied to the new procedure and the extended MLR are described as here used in annex A.

The basic climatic quantities in Eq. (6.3) are determined from the experimental data points. Each point corresponds to a 10 min time acquisition and the related quantities,

after a proper weighting procedure (EN 12975, 2006), are the elements of one single row matrix (matrix K in annex A). The whole experimental data set allows to fill a complete matrix, whose number of rows is equal to the number of data points. The coefficients in Eqs. (6.1), (6.2) and (6.3) and their uncertainties are obtained from the above matrix computation as described in EN 12975 (2006) and Kratzenberg et al (2006).

The same data taken for the quasi-dynamic tests are also filtered to obtain the performance data in steady-state conditions. The required test conditions for the steady-state method are reported in Table 3.3. The standard regression method in steady-state conditions is applied to these filtered data.

The multiple linear regression provides parameter values and relative uncertainties. In this paper uncertainties with 95% confidence interval are reported, calculated following the instructions provided in EN 12975 (2006) and Kratzenberg et al (2006) and described in Zambolin and Del Col (2010).

As reported in Eqs. (6.1) and (6.2) the parameter $K_{\theta t}$ and $K_{\theta l}$ are defined as functions of θ_t and θ_l respectively, which are required inputs. In this work they are estimated following the method described in McIntire and Reed (1983).

6.5 Discussion of results

The regression results are used to compare the methods described in Sect. 6.4, in order to validate the transversal angle modifier model reported in Eq. (6.2) and its applicability to the quasi-dynamic model (Eq. (6.3)) and also to compare the performance of the collector with and without CPC reflectors.

In the two cases, with and without reflectors, the same value of the aperture area (reported in Table 6.1) is considered in the calculation of efficiency to get a direct comparison between the two data sets, although the European standard provides a different rule for the aperture area computation in the case without back reflectors as described in Figure 1.3.

6.5.1 Comparison of different regression methods

In this work the results obtained by the parameter identification applied to the quasi-dynamic model, using the polynomial function in Eq. (6.2) for $K_{\theta t}$ and the function in Eq. (6.1) for $K_{\theta l}$, have been compared to the results obtained by the extended multiple linear regression applied to the quasi-dynamic method and also to the results obtained by means of the steady-state analysis.

In the following, the first procedure will be named new quasi-dynamic method (new q-d), the second extended quasi-dynamic method (extended q-d) and the third one steady-state method (s-s). The third method does not allow to obtain any information regarding the trend of optical efficiency when varying incidence angle.

The quasi-dynamic method described in this chapter is validated by comparing its results to the efficiency curve in standard stationary conditions as described in EN 12975 (2006), i.e. at G=1000 W/m^2, at normal incidence angle of the solar direct radiation.

In Figure 6.3 the stationary standard efficiency curves obtained from the new quasi-dynamic method for the evacuated collector with and without CPC reflectors are compared to the corresponding curves obtained from the steady-state method.

Similarly, the efficiency curves obtained from the extended quasi-dynamic method are plotted in Figure 6.4. The curves reported in Figures 6.3 and 6.4 with the new quasi-dynamic test method are in agreement, within their uncertainty ranges, with the curves given by the steady-state and extended quasi-dynamic methods.

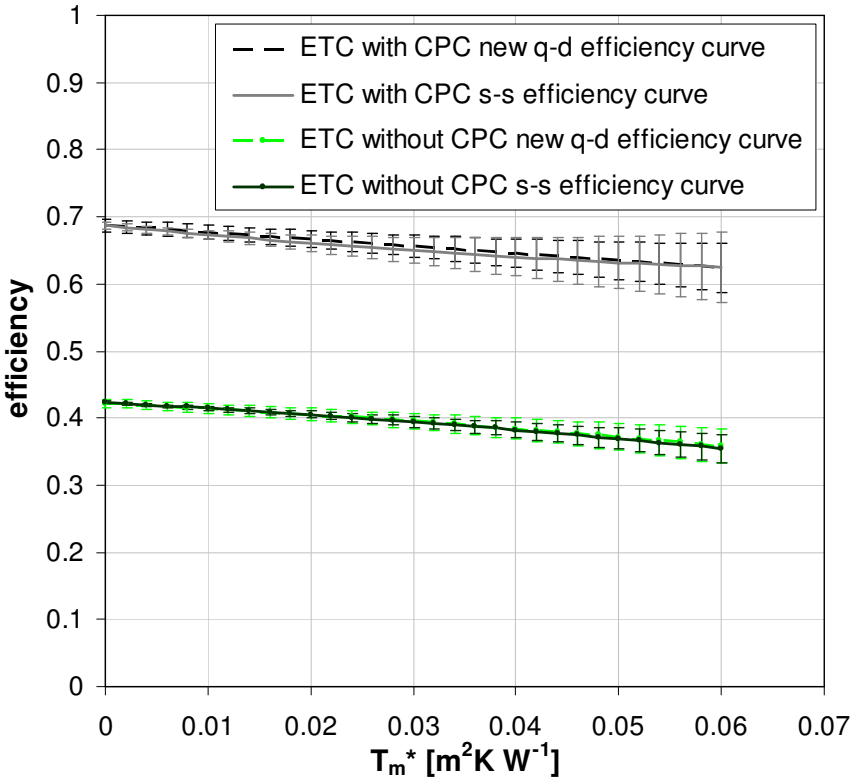

Figure 6.3. Efficiency curves at *G*=1000 W/m^2 and normal incidence angle of the solar direct radiation. Comparison between results obtained with the new quasi-dynamic method and with the steady-state method, with and without CPC reflectors.

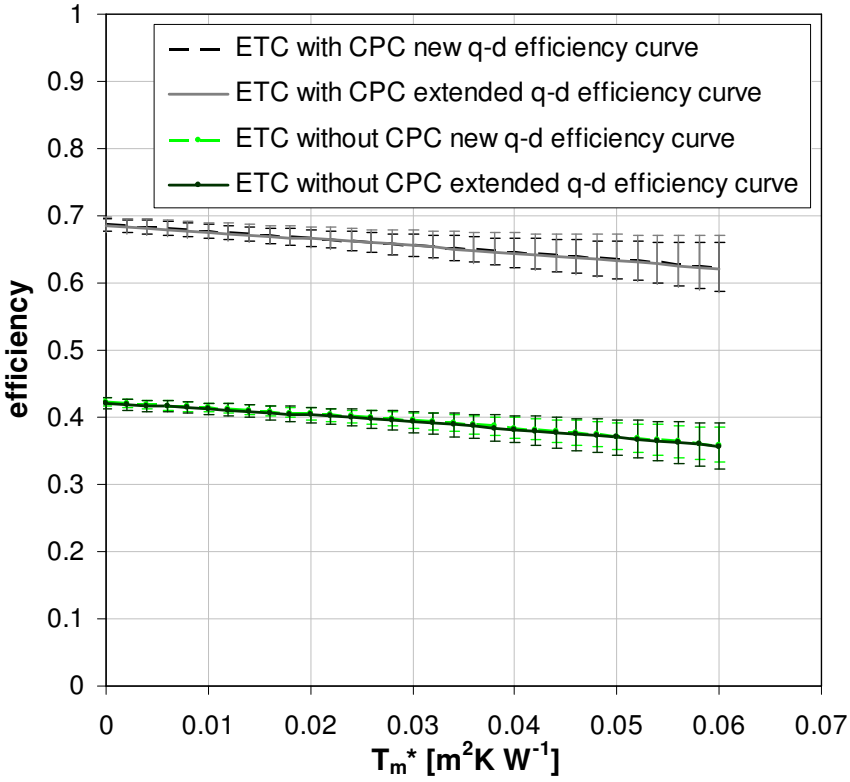

Figure 6.4. Efficiency curves at G=1000 W/m^2 and normal incidence angle of the solar direct radiation. Comparison between results obtained with the new quasi-dynamic method and with the extended quasi-dynamic method, with and without CPC reflectors.

Another comparison can be made in terms of incidence angle modifier versus incidence angle between the new method and the extended quasi-dynamic method.

In Figure 6.5 the incidence angle modifiers obtained from the new quasi-dynamic method are reported: $K_{\theta t}$ and $K_{\theta l}$ are the modifiers defined in Eqs. (6.1) and (6.2), as a function of θ_t and θ_l respectively. The same modifiers are depicted both with and without CPC reflectors. The trends display maximum $K_{\theta t}$ values at around θ_t=62°. At this angle the reciprocal shading between adjacent tubes (absorber tubes) starts. This value was verified from geometrical computation.

The modifiers obtained by this procedure are continuous curves and these results look different from the results obtained by extended quasi-dynamic method, where average values of $K_{\theta t}$ for each angle interval are provided. This can be seen in Figure 6.6 where the transversal incidence angle modifiers obtained by the quasi-dynamic method and by the extended quasi-dynamic method are reported. The extended method provides a step function. Apart from this basic difference, the agreement between the curves is clearly shown, in fact for each θ_t interval the medium $K_{\theta t}$ value obtained from the new

quasi-dynamic method is comparable with the value resulting from the extended quasi-dynamic method. Results are depicted both for the case with and without CPC reflectors. Only in the range between 45° and 60°, in the case without reflectors, the two curves display some discrepancy.

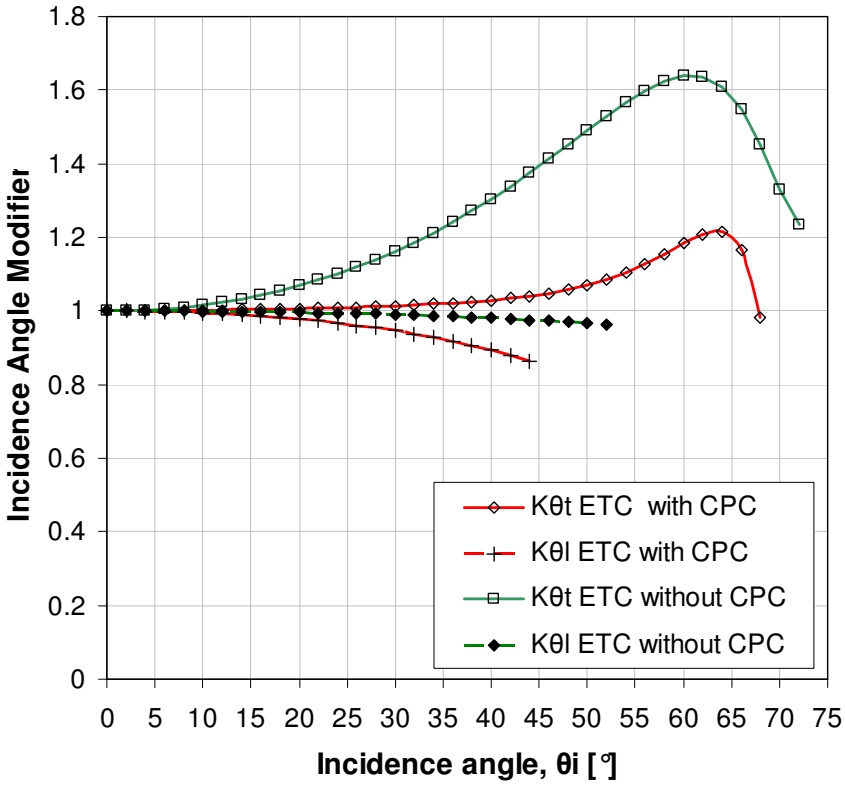

Figure 6.5. Incidence angle modifiers obtained by means of the new quasi-dynamic method: $K_{\theta t}$ and $K_{\theta l}$ are the parameters defined in Eqs. (6.1) and (6.2), with $\theta_i=\theta_t$ and $\theta_i=\theta_l$, respectively. Both the IAM for the collector with and without CPCs are depicted.

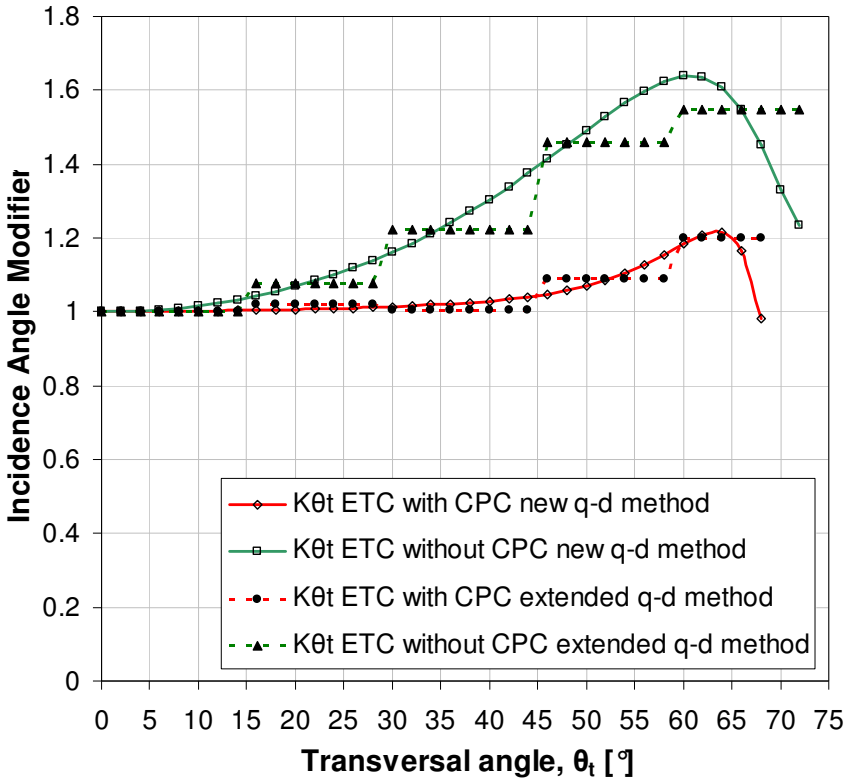

Figure 6.6. Comparison of the transversal incidence angle modifiers obtained by means of the new quasi-dynamic method and the extended quasi-dynamic method, with and without CPCs.

The comparative parameters and their uncertainties, both with and without reflectors, are reported in Tables 6.2, 6.3 and 6.4. Table 6.2 reports the collector coefficients obtained by means of the new quasi-dynamic method with the predetermined function for the transversal incidence angle; the coefficients obtained by the extended quasi-dynamic method are listed in Table 6.3 and the parameters given by the steady-state method in Table 6.4.

From Table 6.3, one can see the uncertainties of the incidence angle modifiers obtained from the extended MLR method at varying transversal angle and these values can be used to compute the uncertainty of the optical efficiency in the transversal direction when θ_l=0. An uncertainty analysis has also been performed for the new procedure, leading to the computation of the uncertainty bands of the optical efficiency in the transversal direction. The amplitude of these bands increases with increasing transversal incidence angle but it is lower as compared to the extended quasi-dynamic (extended MLR) method up to the incidence angle θ_l=62°.

Table 6.2. Collector coefficients and uncertainties obtained with the new procedure: the MLR is applied to the quasi-dynamic model with the predetermined function for the transversal incidence angle, as in Eq. (6.2). Results are reported for the collector with and without CPC reflectors.

	ETC with CPC		ETC without CPC	
Parameter	**Value**	**Uncertainty**	**Value**	**Uncertainty**
$F'(\tau\alpha)_{en}$	0.6882	0.0105	0.4046	0.0066
b_1	0.1100		1.0835	
b_2	-0.1936		-0.1870	
b_3	0.5602		-0.3777	
b_4	-0.2920		0.1188	
b_0	-0.3475	0.6735	-0.0605	0.7219
$K_{\theta d}$	1.0135	0.0326	1.1869	0.0459
c_1 [W/(m^{2}K)]	1.022	0.383	0.727	0.274
c_2 [W/(m^{2}K^2)]	0.001	0.007	0.006	0.005
c_5 [J/(m^{2}K)]	48587	2931	44817	3586

Table 6.3. Collector coefficients and uncertainties obtained by means of the extended MLR applied to the quasi-dynamic model. Results are reported for the collector with and without CPC reflectors.

	ETC with CPC		ETC without CPC	
Parameter	**Value**	**Uncertainty**	**Value**	**Uncertainty**
$F'(\tau\alpha)_{en}$	0.6859	0.015	0.4083	0.0083
$K_{\theta t}$ ($\theta_t < 15°$)	1		1	
$K_{\theta t}$ ($15° < \theta_t < 30°$)	1.0186	0.0330	1.078	0.0335
$K_{\theta t}$ ($30° < \theta_t < 45°$)	1.0042	0.0377	1.2224	0.0438
$K_{\theta t}$ ($45° < \theta_t < 60°$)	1.0882	0.0524	1.4599	0.0642
$K_{\theta t}$ ($60° < \theta_t < 75°$)	1.1989	0.1236	1.5486	0.1488
b_0	-0.2864	0.4377	0.2006	0.4054
$K_{\theta d}$	1.0186	0.0464	1.1774	0.0596
c_1 [W/(m^{2}K)]	0.907	0.534	0.756	0.369
c_2 [W/(m^{2}K^2)]	0.003	0.010	0.005	0.007
c_5 [J/(m^{2}K)]	47766	4051	46816	4642

Table 6.4. Collector coefficients and uncertainties obtained by means of the steady-state method. Results are reported for the collector with and without CPC reflectors.

	ETC with CPC		ETC without CPC	
Parameter	**Value**	**Uncertainty**	**Value**	**Uncertainty**
η_0	0.6869	0.0048	0.4229	0.0017
a_1 [W/(m2K)]	-1.4709	0.5201	-0.7640	0.2112
a_2 [W/(m2K2)]	0.0073	0.0115	-0.0062	0.0045

From this comparison it follows that the efficiency and incidence angle modifier curves obtained with the new procedure are in agreement with the corresponding results from other procedures; the resulting coefficients and their uncertainties are comparable.

For both cases, with and without CPC reflectors, the new procedure is experimentally validated.

The results reported in this work show the advantage of the present new procedure as compared to the extended MLR: it provides a complete trend of the optical efficiency, depicted by a continuous curve of the incidence angle modifier, whereas the extended MLR provides a step function. Plus, at similar uncertainty of the computed parameters, it requires less experimental data points since the incidence angle is not divided in subintervals. This allows to reduce the duration of the experimental tests.

6.5.2 Performance comparison with and without CPC reflectors

All the figures described in Sect. 6.5.1 provide information on the comparison of the evacuated tube collector with and without CPC reflector, and show the improved performance given by the use of reflector.

Figures 6.3 and 6.4 show that the collector with CPCs displays higher performance than the collector without CPCs, at normal incidence angle of the solar direct radiation (θ=0°). As expected the effect of the CPC reflector turns out only in the optical characteristics, in fact the efficiency curves in the two cases are parallel, therefore the thermal losses are the same.

In the considered collector geometry the reflector effect is described by an optical efficiency increase of 0.274 (66% higher compared to the optical efficiency without CPCs). In fact, in the case without reflector only half section of the evacuated tube is irradiated by the solar direct beam, whereas in the case with CPCs all the tube is irradiated by direct or reflected radiation. The radiation distribution around the tube in a similar case with back reflector has been measured and described in Cabanillas et al. (1995).

At normal incidence angle conditions, in the collector without reflectors, some radiation beams (between the tubes) don't irradiate the absorber surface and go past. In the case with CPCs these beams are reflected into the absorber surface and this effect is responsible for the efficiency difference.

Figure 6.7 reports the efficiency curves obtained at θ_t=62°, which means not at normal incident conditions, but in the case where $K_{\theta t}$ assumes the maximum value (see Figures 6.5 and 6.6). In this condition the CPCs application allow an optical efficiency increase of 0.178 (28% compared to the optical efficiency without CPCs).

In Figure 6.8 the optical efficiency η_0 (efficiency at T_m^*=0) is plotted versus the transversal incidence angle for the collector with and without CPCs. The graph shows that the optical efficiency difference between the two cases reduces with the increase of the angle θ_t. The minimum difference, before reciprocal shading between adjacent tubes

occurs, is obtained at θ_t=54° where the optical efficiency increases is 0.140 (23% compared to the optical efficiency without CPCs).

From these results it appears that the reflector effect is to improve the collector performance at normal incidence angle but also at high transversal angles of incidence, and also at θ_t=62°, where the direct radiation irradiates only the tubes, not directly the reflectors. It means that part of the direct radiation is locally reflected by the glass tube and, if there is a reflector, is reflected again toward the tubes. This local effect is more important where the incidence angle between beam and glass is high and thus the specular reflectance increase, as described in Chow et al. (1984) for flat surface. This local reflects are also shown in Grass et al. (2004) by ray-tracing analysis for evacuated tubes.

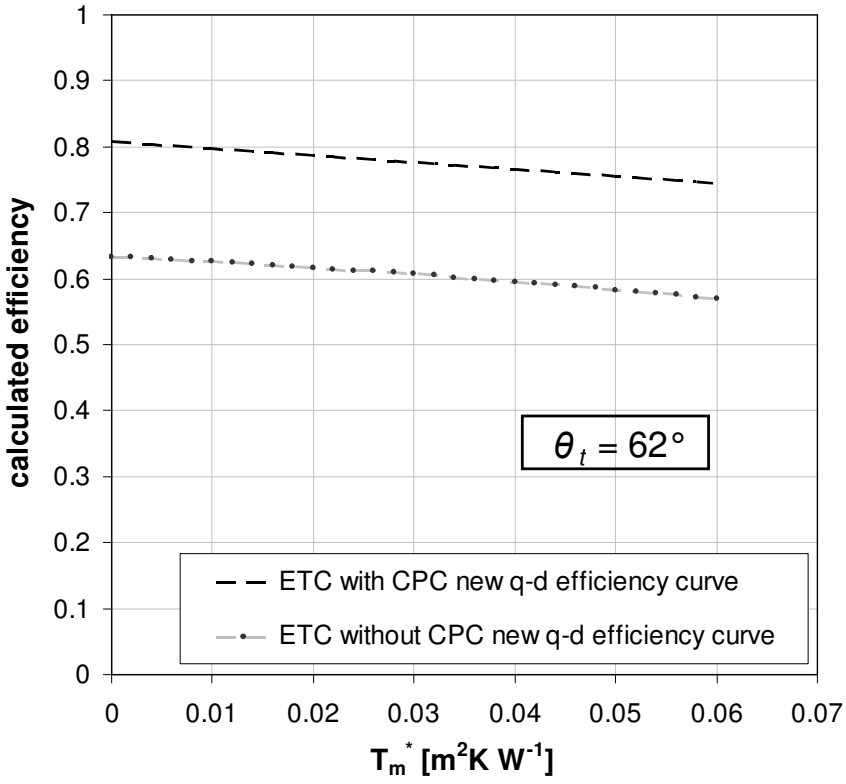

Figure 6.7. Comparison between the cases with and without CPCs: efficiency curves at G=1000 W/m^2 and θ_t=62° (maximum $K_{\theta t}$).

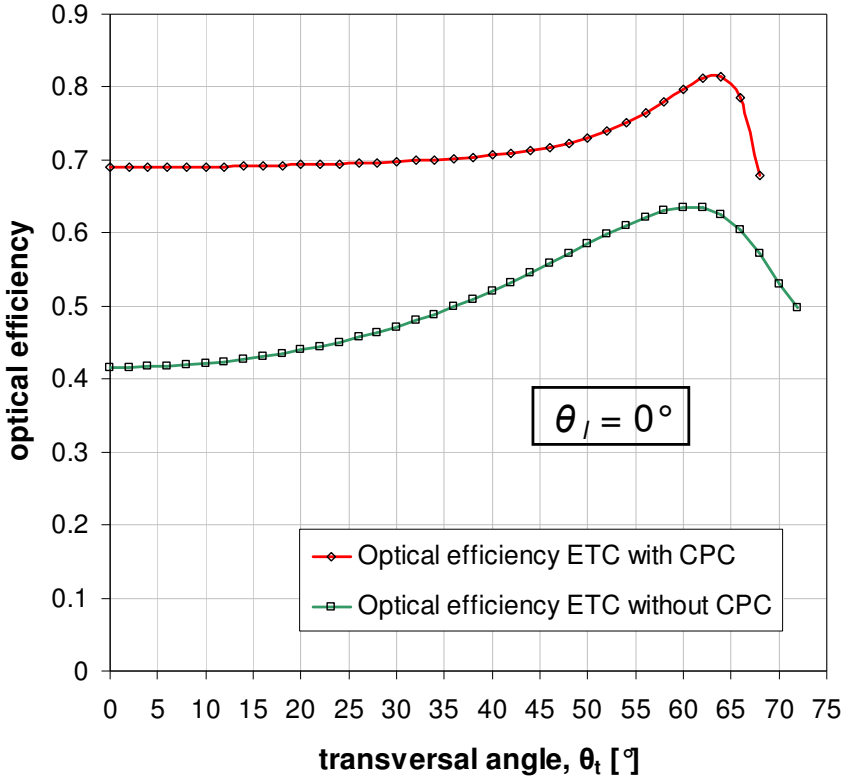

Figure 6.8. Optical efficiency as a function of the transversal incidence angle in the tested evacuated tube collector with and without CPCs.

The optical parameters referred to the cases with and without reflectors are reported in Tables 6.2 and 6.3, according to the two quasi-dynamic methods used in the evaluation. The effect of the longitudinal incidence angle, as described by the b_0 parameter, is also included in these Tables. The values of b_0 are close to 0, as expected. In Budihardjo and Morrison (2009), for instance, the authors find b_0=-0.1.

A confirmation of the slight dependence of the IAM $K_{\theta l}$ on the longitudinal incidence angle can be found from Eq. (1.6). In fact, in the analysed longitudinal angle range $\theta_l \leq 52°$, an almost constant solar absorptance for most coating surfaces can be expected also in the cylindrical geometry (Tesfamichael and Wäckelgård, 2000). Besides, the simulated beam transmittances of a tubular cover are nearly constant in this angle interval (Theunissen and Beckman, 1985). Therefore, when $\theta_l \leq 52°$, it is expected that the derived parameter $K_{\theta l}$ is near to one.

6.5.3 Practical considerations on optical efficiency

The results obtained in this work provide some tips for practical considerations.

Figure 6.8 shows a roughly constant optical efficiency for $\theta_t \leq 52°$ in the case with reflectors, while in the case without reflectors this parameter increases continuously until $\theta_t = 62°$ where the reciprocal shading between adjacent tubes begins.

These trends have been obtained with tubes aligned north-south but similar results are expected also for the east-west tube alignment. This is confirmed in Carvalho et al. (1995) where CPC collector performance has been compared with tubes aligned north-south and east-west for a non-evacuated tube collector (inverted V absorber). In these two cases low differences result for the measured efficiency due to convective effects between glass cover and absorber sheet. Convective heat transfer is negligible in the case of evacuated tube collectors considered in the present work.

The aligned east-west configuration could be a solution to make the converted solar energy for domestic heating and hot water production more constant along the entire year, especially in the case without CPC reflectors and when the inclination of the collector cannot be changed freely. In fact with an appropriate design and choosing a proper distance between the tubes, it is possible to optimize the $K_{\theta t}$ trend and its maximum value. With this solution, in the central hours of the day during the summer season, the average efficiency could be maintained low while in the winter season it could be amplified. Also the stagnation temperature could be maintained low in the summer season; this is a problem for the classic ETC with back reflectors.

This comparison can be done by simulations using the obtained collector coefficients with specified climatic characteristics using TMY (Typical Meteorological Year).

Conclusions

Experimental measurements taken on flat-plate and evacuated tube collectors are presented in this thesis. Tests have been made to compare these two types of solar collectors, to validate a numerical model developed to simulate the performance of a flat-plate collector and to validate a new procedure to characterize evacuated tube collectors.

The efficiency curves and the incidence angle modifier curves have been obtained following the steady-state and the quasi-dynamic methods described in the standard EN 12975 (2006).

a. Collectors comparison and daily efficiency

Test runs in daily conditions are performed for the characterization of the collectors' performance. Input/output diagrams and daily efficiency curves are obtained from these tests.

The curves obtained from steady-state and quasi-dynamic test methods are in agreement within their uncertainty ranges; this is true both for FPC and for ETC. For the latter, a particular MLR with predetermined function of $K_{\theta l}$ and $K_{\theta t}$ in the quasi-dynamic method has been used.

The input/output diagrams provide a linear relationship between the daily energy collected and daily solar radiation energy at constant operating temperature difference $(\overline{t_m} - \overline{t_a})$.

As expected, the flat-plate collector is more sensitive to this temperature difference than the evacuated tube collector. Essentially, the flat-plate collectors here considered work more efficiently when the inlet fluid temperature is near to the ambient air temperature, while the evacuated tube collector displays higher efficiency when the temperature difference between the mean temperature of the fluid and the surrounding air is higher than about 25 K.

From the comparison between the efficiency diagrams obtained in standard stationary and daily conditions, two different cross-over points between the evacuated and flat plate efficiency curves are observed: 0.037 m^2K/W in standard conditions and 0.027 m^2K/W in the daily tests. This difference is essentially due to the variations of the optical efficiency term in the daily tests for the evacuated tube and flat-plate collector, in fact the heat loss coefficients (in the first order curve) for both sets of data have roughly the same values.

In the flat-plate collector the optical efficiency of the collector in the morning and in the afternoon hours decreases due to the larger reflection losses. In the vacuum tube collector, these efficiency losses are reduced; this effect is due to the cylindrical geometry and to the CPC reflectors.

As a result, in the daily tests the evacuated collector displays a higher efficiency for a larger range of operating conditions, as compared to the flat-plate collector. The daily average reduced temperature can represent a proper characteristic parameter for usual working conditions and it may be calculated from ambient data and operating conditions.

By using the parameters of the quasi-dynamic model, it is possible to estimate the daily efficiency, covering a wider range of operating conditions as compared to the stationary standard case. The daily efficiency curve is experimentally based and theoretically explained. The collector coefficients from the quasi-dynamic model can be used for the simulation of the yearly energy production in a region with specified climatic characteristics but can also be used to construct a daily efficiency curve which represents an easy-to-use tool for quick evaluation of collectors (without considering the system) in a wide range of operating conditions.

b. New procedure to characterize evacuated tube collectors

A polynomial model for the transversal incidence angle modifier of evacuated tube collectors has been presented and applied to the quasi-dynamic model described in EN 12975 (2006). The results obtained by the multiple linear regression applied to the experimental data have been compared to the corresponding results obtained by means of the steady-state method and extended multiple linear regression method.

From this comparison it follows that the efficiency and incidence angle modifier curves obtained with the new procedure are in agreement with the corresponding results from other procedures; the obtained coefficients and their uncertainties are comparable.

This validation has been performed for one evacuated tube collector in two different configurations, with and without CPC reflectors. For both cases the new procedure is experimentally validated.

The results reported in this work show the advantage of the present new procedure as compared to the extended MLR: it provides a complete trend of the optical efficiency, depicted by a continuous curve of the incidence angle modifier, whereas the extended MLR provides a step function. Plus, at similar uncertainty of the computed parameters,

it requires less experimental data points. This allows to reduce the duration of the experimental tests.

The same results can also be used to obtain information on the performance increase due to the use of CPC reflectors in the specific geometry. As expected, the reflectors affect only the optical efficiency of the collector. The use of this type of reflectors brings an optical efficiency increase of 0.274 (66% higher) in near normal incidence angle conditions. This effect reduces with the transversal incidence angle increase; at θ_t=62°, where $K_{\theta t}$ assumes the maximum value, the CPCs application allows an optical efficiency increase of 0.178 (28% higher).

The experimental trend of optical efficiency allows to conclude that, when using reflectors, the optical efficiency is pretty constant for a wide range of incidence angle; if there are not reflectors, the east-west tube alignment could be a tool for balancing the heat production between summer and winter seasons. This could allow to use a higher collector area without encountering overheating problems in the summer season and improving the heating production in the winter season.

c. Numerical model for flat-plate collector

A numerical model for flat-plate solar thermal collectors has been developed, and predictions have been compared with experimental data. Tests on two flat-plate collectors (a prototype collector and a flat-plate collector with aluminium plate) have been performed to validate the model.

The calculated and experimental stationary efficiency curves referred to the examined collectors show that the efficiency curve deviation is below 5% in the reduced temperature range between 0 and 0.07 m^2K/W for both the test collectors.

To obtain a more detailed analysis, proper tests have been performed to provide the temperature profile on the prototype collector.

The investigation shows that the fin theory, used in the model, describes the sheet temperature in agreement with the experimental results.

From the results obtained by means of the heat loss investigation with and without solar radiation on the prototype collector, it is possible to conclude that the efficiency curve deviation is caused by a small underestimation of both the heat loss and the optical efficiency of the collector.

In the model the control element welded to the plate and the control element not welded, have been considered separately: this consideration is in agreement with the results obtained by the infrared thermal analysis, where two completely different plate behaviours can be seen.

The numerical model presented in this thesis has been used to analyse various collector configurations and to compare different component materials. From these simulations we can conclude that:

- The copper plate could be replaced with aluminium absorber plate obtaining similar collector efficiency;

- the convective heat transfer coefficient between absorber plate and glass cover is an important term of the collector heat loss;
- the serpentine solution is equivalent to the parallel tubes configuration;
- the roll-bond geometry can be a solution to optimize the collector performance.

Annex A.
Multiple linear regression

The Multiple linear regression (MLR) is a method which calculate, on the base of the measured values and their uncertainty, not only the model parameters but also their uncertainty (EN 12975, 2006).

In this annex this procedure is described. It is used for the steady-state method (FPC and ETC), quasi-dynamic method (FPC), new quasi-dynamic method and extended quasi-dynamic method (ETC).

A.1 General procedure and uncertainty analysis

In all the over reported methods it is assumed that the behaviour of the collector can be described by a M-parameter model:

$$\eta = c_1 \cdot p_1 + c_2 \cdot p_2 + ... + c_M \cdot p_M \qquad \text{(A.1)}$$

where:

$p_1, p_2, ..., p_M$ are the basic climatic quantities, the value of which are determined experimentally through testing;

$c_1, c_2, ..., c_M$ are characteristic unknown constants of the collector;

The basic climatic quantities p_m are measured in J state experimental points (in this work time interval of 10 minutes). The experimental procedure of the testing leads to a formation of a group of J observations which comprise, for each one of the J testing points, the values of $\eta_j, p_{1,j}, p_{2,j}, ..., p_{6,j}$.

In each point j the uncertainty u is estimated for each value of p_m and η following generals rules reported in ISO GUM (1995). The variance u_j for each experimental point is obtained as:

$$u_j = \sqrt{\left(u(\eta)_j\right)^2 + c_1{}^2 \cdot \left(u\left(p_{1,j}\right)\right)^2 + \ldots + c_M{}^2 \cdot \left(u\left(p_{M,j}\right)\right)^2} \tag{A.2}$$

where the initial parameters c_m can be obtained by the least square fittings or by the available information.

Let K be a matrix $J \times M$:

$$K = \begin{bmatrix} \frac{p_{1,1}}{u_1} & \frac{p_{1,2}}{u_1} & \cdot & \cdot & \cdot & \frac{p_{1,M}}{u_1} \\ \frac{p_{2,1}}{u_2} & \frac{p_{2,2}}{u_2} & \cdot & \cdot & \cdot & \frac{p_{2,M}}{u_2} \\ \cdot & \cdot & \cdot & \cdot & \cdot & \cdot \\ \cdot & \cdot & \cdot & \cdot & \cdot & \cdot \\ \frac{p_{J,1}}{u_J} & \frac{p_{J,2}}{u_J} & \cdot & \cdot & \cdot & \frac{p_{J,1}}{u_J} \end{bmatrix} \tag{A.3}$$

and L a vector of length J:

$$L = \begin{bmatrix} \frac{\eta_1}{u_1} \\ \frac{\eta_2}{u_2} \\ \cdot \\ \cdot \\ \frac{\eta_J}{u_J} \end{bmatrix} \tag{A.4}$$

the normal equation of the least square problem can be written:

$$C = (K^T \cdot K)^{-1} \cdot K^T \cdot L \tag{A.5}$$

where C is the vector whose elements c_m are the fitted coefficients.

Moreover $(K^T \cdot K)^{-1}$ is a matrix whose diagonal elements are the squared uncertainties (variances) related to fitted coefficients and the off-diagonal elements are the covariances between the fitted coefficients. Two quantities are uncorrelated where the covariance between them is equal to zero, otherwise they are correlated.

A.2 Application to the steady-state method

The steady-state method is applicable to flat-pate (FPC) and evacuated tube collectors (ETC). The basic model for this method is:

$$\eta = \eta_0 - a_1 T_m^* - a_2 G (T_m^*)^2 \tag{A.6}$$

and so in reference to the Eq. (A.1):

$$\eta = \eta$$
$$c_1 = \eta_0$$
$$c_2 = -a_1$$
$$c_3 = -a_2$$
$$p_1 = 1$$
$$p_2 = T_m^*$$
$$p_3 = G \cdot T_m^{*2}$$

The parameters in the left side are referred to Eq. (A.1) while the ones in the right side to Eq. (A.6).

A.3 Application to the quasi-dynamic method

The basic model in the quasi-dynamic method is:

$$\frac{\dot{Q}_{out}}{A_a} = F' \cdot (\tau\alpha)_{en} \cdot K_{\theta b} \cdot (\theta) \cdot G_b + F' \cdot (\tau\alpha)_{en} \cdot K_{\theta d} \cdot G_d - c_6 \cdot u \cdot G +$$
$$- c_1 \cdot (t_m - t_a) - c_2 \cdot (t_m - t_a)^2 - c_3 \cdot u \cdot (t_m - t_a) + c_4 \cdot \left(E_L - \sigma \cdot T_a^{\,4}\right) - c_5 \cdot dT_m / d\tau \tag{A.7}$$

where, following the guidelines in EN 12975 (2006), the coefficients c_6, c_3 and c_4 are assumed to be without statistical significance.

A.3.1 Quasi-dynamic method for flat-plate collector

In this case the parameter $K_{\theta b}(\theta)$ is assumed:

$$K_{\theta b}(\theta) = 1 + b_0 \cdot \left(\frac{1}{\cos(\theta)} - 1 \right) \tag{A.8}$$

and the global model reported in Eq. (A.7) become:

$$\frac{\dot{Q}_{out}}{A_a} = F' \cdot (\tau\alpha)_{en} \cdot G_b + F' \cdot (\tau\alpha)_{en} \cdot b_0 \cdot G_b \cdot \left(\frac{1}{\cos(\theta)} - 1 \right) + F' \cdot (\tau\alpha)_{en} \cdot K_{\theta d} \cdot G_d +$$
$$- c_1 \cdot (t_m - t_a) - c_2 \cdot (t_m - t_a)^2 - c_5 \cdot dT_m / d\tau \tag{A.9}$$

and so in reference to the Eq. (A.1):

$$\eta = \frac{\dot{Q}_{out}}{A_a}$$
$$c_1 = F' \cdot (\tau\alpha)_{en}$$
$$c_2 = b_0 \cdot F' \cdot (\tau\alpha)_{en}$$
$$c_3 = F' \cdot (\tau\alpha)_{en} \cdot K_{\theta d}$$
$$c_4 = -c_1$$
$$c_5 = -c_2$$
$$c_6 = -c_5$$
$$p_1 = G_b$$
$$p_2 = G_b \cdot \left(\frac{1}{\cos(\theta)} - 1 \right)$$
$$p_3 = G_d$$
$$p_4 = t_m - t_a$$
$$p_5 = (t_m - t_a)^2$$
$$p_6 = \Delta t_m / \Delta\tau \, .$$

The parameters in the left side are referred to Eq. (A.1) while the ones in the right side to Eq. (A.9).

It may be notice that in this case $b_0 = c_2 / c_1$ and $K_{\theta d} = c_3 / c_1$.

A.3.2 New quasi-dynamic method for evacuated tube collector

This method has been developed by the author for tests on evacuated tube collectors. In this case the parameter $K_{\theta b}(\theta)$ is not dependent on one single incidence angle θ as in Eq. (A.8). Instead, the incident beam must be split in two dimensions and the modifier can be described as $K_{\theta b}\ (\theta_t,\theta_l)$, where θ_t and θ_l are the transverse and longitudinal projection of incidence angle θ, respectively.

For this type of collector the incidence angle modifier is approximated by the product of two separate incidence angle modifiers (McIntire and Reed, 1983): $K_{\theta t}\ (\theta_t,0)$ and $K_{\theta l}\ (0,\theta_l)$:

$$K_{\theta l} = 1 + b_0 \cdot \left(\frac{1}{\cos(\theta_l)} - 1 \right) \tag{A.10}$$

$$K_{\theta t} = 1 + b_1 \cdot \left(\frac{1}{\cos(\theta_t)} - 1 \right) + b_2 \cdot \left(\frac{1}{\cos(\theta_t)} - 1 \right)^2 + b_3 \cdot \left(\frac{1}{\cos(\theta_t)} - 1 \right)^3 + b_4 \cdot \left(\frac{1}{\cos(\theta_t)} - 1 \right)^4 \tag{A.11}$$

The global model reported in Eq. (A.7) become:

$$\begin{aligned}
\frac{\dot{Q}_{out}}{A_a} = {} & F' \cdot (\tau\alpha)_{en} \cdot G_b + \left[b_1 \cdot \left(\frac{1}{\cos(\theta_t)} - 1 \right) + b_2 \cdot \left(\frac{1}{\cos(\theta_t)} - 1 \right)^2 + b_3 \cdot \left(\frac{1}{\cos(\theta_t)} - 1 \right)^3 + b_4 \cdot \left(\frac{1}{\cos(\theta_t)} - 1 \right)^4 \right] \cdot F' \cdot (\tau\alpha)_{en} \cdot G_b + \\
& + \left(b_0 \cdot \left(\frac{1}{\cos(\theta_l)} - 1 \right) \right) \cdot F' \cdot (\tau\alpha)_{en} \cdot G_b + \left[b_0 \cdot b_1 \cdot \left(\frac{1}{\cos(\theta_t)} - 1 \right) \left(\frac{1}{\cos(\theta_l)} - 1 \right) + b_0 \cdot b_2 \cdot \left(\frac{1}{\cos(\theta_t)} - 1 \right)^2 \left(\frac{1}{\cos(\theta_l)} - 1 \right) + \right. \\
& \left. + b_0 \cdot b_3 \cdot \left(\frac{1}{\cos(\theta_t)} - 1 \right)^3 \left(\frac{1}{\cos(\theta_l)} - 1 \right) + b_0 \cdot b_4 \cdot \left(\frac{1}{\cos(\theta_t)} - 1 \right)^4 \left(\frac{1}{\cos(\theta_l)} - 1 \right) \right] \cdot F' \cdot (\tau\alpha)_{en} \cdot G_b + \\
& + F' \cdot (\tau\alpha)_{en} \cdot K_{\theta l} \cdot G_d - c_1 \cdot (t_m - t_a) - c_2 \cdot (t_m - t_a)^2 - c_5 \cdot dT_m / d\tau
\end{aligned} \tag{A.12}$$

and in reference to the Eq. (A.1):

$$\eta = \frac{\dot{Q}_{out}}{A_a}$$

$$c_1 = F' \cdot (\tau\alpha)_{en}$$

$$c_2 = F' \cdot (\tau\alpha)_{en} \cdot b_1$$

$$c_3 = F' \cdot (\tau\alpha)_{en} \cdot b_2$$

$$c_4 = F' \cdot (\tau\alpha)_{en} \cdot b_3$$

$$c_5 = F' \cdot (\tau\alpha)_{en} \cdot b_4$$
$$c_6 = F' \cdot (\tau\alpha)_{en} \cdot b_0$$
$$c_7 = F' \cdot (\tau\alpha)_{en} \cdot b_0 \cdot b_1$$
$$c_8 = F' \cdot (\tau\alpha)_{en} \cdot b_0 \cdot b_2$$
$$c_9 = F' \cdot (\tau\alpha)_{en} \cdot b_0 \cdot b_3$$
$$c_{10} = F' \cdot (\tau\alpha)_{en} \cdot b_0 \cdot b_4$$
$$c_{11} = F' \cdot (\tau\alpha)_{en} \cdot K_{\theta d}$$
$$c_{12} = -c_1$$
$$c_{13} = -c_2$$
$$c_{14} = -c_5$$
$$p_1 = G_b$$
$$p_2 = G_b \cdot \left(\frac{1}{\cos(\theta_t)} - 1 \right)$$
$$p_3 = G_b \cdot \left(\frac{1}{\cos(\theta_t)} - 1 \right)^2$$
$$p_4 = G_b \cdot \left(\frac{1}{\cos(\theta_t)} - 1 \right)^3$$
$$p_5 = G_b \cdot \left(\frac{1}{\cos(\theta_t)} - 1 \right)^4$$
$$p_6 = G_b \cdot \left(\frac{1}{\cos(\theta_l)} - 1 \right)$$
$$p_7 = G_b \cdot \left(\frac{1}{\cos(\theta_t)} - 1 \right) \cdot \left(\frac{1}{\cos(\theta_l)} - 1 \right)$$
$$p_8 = G_b \cdot \left(\frac{1}{\cos(\theta_t)} - 1 \right)^2 \cdot \left(\frac{1}{\cos(\theta_l)} - 1 \right)$$
$$p_9 = G_b \cdot \left(\frac{1}{\cos(\theta_t)} - 1 \right)^3 \cdot \left(\frac{1}{\cos(\theta_l)} - 1 \right)$$
$$p_{10} = G_b \cdot \left(\frac{1}{\cos(\theta_t)} - 1 \right)^4 \cdot \left(\frac{1}{\cos(\theta_l)} - 1 \right)$$
$$p_{11} = G_d$$
$$p_{12} = t_m - t_a$$

$$p_{13} = (t_m - t_a)^2$$
$$p_{14} = \Delta t_m / \Delta \tau$$

The parameters in the left side are referred to Eq. (A.1) while the ones in the right side to Eq. (A.12).

It may be notice that in this case $b_1 = c_2/c_1$, $b_2 = c_3/c_1$, $b_3 = c_4/c_1$, $b_4 = c_5/c_1$, $b_0 = c_6/c_1$ and $K_{\theta l} = c_{11}/c_1$. The coefficient c_7, c_8, c_9 and c_{10} are not considered.

A.3.3 Extended quasi-dynamic method for evacuated tube collector

The extended quasi-dynamic method is described in Perers (1997). It can identify non-linear parameters by dividing the range of conditions where it is applied, providing an average value of the considered parameter.

In this work it is used for evacuated tube collectors, to determine the incidence transversal angle $K_{\theta t}$ at specific intervals of the incidence angle, dividing the space in transversal angle (θ_t) intervals and providing an average value of $K_{\theta t}$ for each θ_t angle interval.

In this work Eq. (A.10) has been used for the longitudinal incidence angle modifier $K_{\theta l}$ and $K_{\theta t}$ has been considered as a vector:

$$K_{\theta t} = [K_{\theta t1}, K_{\theta t2}, K_{\theta t3}, K_{\theta t4}, K_{\theta t5}, K_{\theta t6}] \tag{A.13}$$

where the components $K_{\theta ti}$ are the average incidence angle modifiers for each angle interval: $K_{\theta t1}$ is defined for $|\theta_t| < 15°$ and it is assumed equal to 1, $K_{\theta t2}$ for $15° < |\theta_t| < 30°$, $K_{\theta t3}$ for $30° < |\theta_t| < 45°$, $K_{\theta t4}$ for $45° < |\theta_t| < 60°$, $K_{\theta t5}$ for $60° < |\theta_t| < 75°$, $K_{\theta t6}$ for $75° < |\theta_t| < 90°$. This last parameter ($K_{\theta t6}$) has not considered because was not acquired data in this range of angle.

The global model reported in Eq. (A.7) become:

$$\frac{\dot{Q}_{out}}{A_a} = F' \cdot (\tau\alpha)_{en} \cdot K_{\theta t} \cdot G_b + F' \cdot (\tau\alpha)_{en} \cdot K_{\theta t} \cdot b_0 \cdot G_b \cdot \left(\frac{1}{\cos(\theta_l)} - 1 \right) + F' \cdot (\tau\alpha)_{en} \cdot K_{\theta l} \cdot G_d +$$
$$- c_1 \cdot (t_m - t_a) - c_2 \cdot (t_m - t_a)^2 - c_5 \cdot dT_m / d\tau \tag{A.14}$$

The input data are arranged for the extended method defining the matrix K where the direct radiation terms are sorted in different columns depending on the average incidence angle during the period of observation. The model parameters are identified by the matrix K defined as:

$$K=\begin{bmatrix}
0 & 0 & 0 & 0 & G_b/\mathrm{u}_1 & 0 & 0 & 0 & 0 & G_b\cdot\left(\frac{1}{\cos(\theta_t)}-1\right)\Big/\mathrm{u}_1 & G_d/\mathrm{u}_1 & .. & (\Delta t_m/\Delta\tau)/\mathrm{u}_1 \\
0 & 0 & 0 & G_b/\mathrm{u}_2 & 0 & 0 & 0 & 0 & G_b\cdot\left(\frac{1}{\cos(\theta_t)}-1\right)\Big/\mathrm{u}_2 & 0 & G_d/\mathrm{u}_2 & .. & (\Delta t_m/\Delta\tau)/\mathrm{u}_2 \\
0 & 0 & G_b/\mathrm{u}_3 & 0 & 0 & 0 & 0 & G_b\cdot\left(\frac{1}{\cos(\theta_t)}-1\right)\Big/\mathrm{u}_3 & 0 & 0 & G_d/\mathrm{u}_3 & .. & (\Delta t_m/\Delta\tau)/\mathrm{u}_3 \\
0 & G_b/\mathrm{u}_4 & 0 & 0 & 0 & 0 & G_b\cdot\left(\frac{1}{\cos(\theta_t)}-1\right)\Big/\mathrm{u}_4 & 0 & 0 & 0 & G_d/\mathrm{u}_4 & .. & (\Delta t_m/\Delta\tau)/\mathrm{u}_4 \\
G_b/\mathrm{u}_5 & 0 & 0 & 0 & 0 & G_b\cdot\left(\frac{1}{\cos(\theta_t)}-1\right)\Big/\mathrm{u}_5 & 0 & 0 & 0 & 0 & G_d/\mathrm{u}_5 & .. & (\Delta t_m/\Delta\tau)/\mathrm{u}_5 \\
0 & G_b/\mathrm{u}_6 & 0 & 0 & 0 & 0 & G_b\cdot\left(\frac{1}{\cos(\theta_t)}-1\right)\Big/\mathrm{u}_6 & 0 & 0 & 0 & G_d/\mathrm{u}_6 & .. & (\Delta t_m/\Delta\tau)/\mathrm{u}_6 \\
. & . & . & . & . & . & . & . & . & . & . & .. & . \\
. & . & . & . & . & . & . & . & . & . & . & .. & . \\
0 & 0 & 0 & 0 & G_b/\mathrm{u}_J & 0 & 0 & 0 & 0 & G_b\cdot\left(\frac{1}{\cos(\theta_t)}-1\right)\Big/\mathrm{u}_J & G_d/\mathrm{u}_J & .. & (\Delta t_m/\Delta\tau)/\mathrm{u}_J
\end{bmatrix} \tag{A.15}$$

This matrix is an example where: the 1st raw is related to an interval $60° < |\theta_t| < 75°$, the 2nd raw is related to $45° < |\theta_t| < 60°$, the 3rd is related to $30° < |\theta_t| < 45°$, the 4th is related to $15° < |\theta_t| < 30°$, the 5th is related to $|\theta_t| < 15°$, the 6th is related to $15° < |\theta_t| < 30°$ and the last one (the Jth) raw is related to $60° < |\theta_t| < 75°$.

In reference to the Eq. (A.1):

$$\eta = \frac{\dot{Q}_{out}}{A_a}$$
$$c_1 = F' \cdot (\tau\alpha)_{en}$$
$$c_2 = F' \cdot (\tau\alpha)_{en} \cdot K_{\theta t2}$$
$$c_3 = F' \cdot (\tau\alpha)_{en} \cdot K_{\theta t3}$$
$$c_4 = F' \cdot (\tau\alpha)_{en} \cdot K_{\theta t4}$$
$$c_5 = F' \cdot (\tau\alpha)_{en} \cdot K_{\theta t5}$$
$$c_6 = F' \cdot (\tau\alpha)_{en} \cdot b_0$$
$$c_7 = F' \cdot (\tau\alpha)_{en} \cdot b_0 \cdot K_{\theta t2}$$
$$c_8 = F' \cdot (\tau\alpha)_{en} \cdot b_0 \cdot K_{\theta t3}$$
$$c_9 = F' \cdot (\tau\alpha)_{en} \cdot b_0 \cdot K_{\theta t4}$$
$$c_{10} = F' \cdot (\tau\alpha)_{en} \cdot b_0 \cdot K_{\theta t5}$$
$$c_{11} = F' \cdot (\tau\alpha)_{en} \cdot K_{\theta d}$$
$$c_{12} = -c_1$$
$$c_{13} = -c_2$$
$$c_{14} = -c_5$$

$$p_1 = G_b$$
$$p_2 = G_b$$
$$p_3 = G_b$$
$$p_4 = G_b$$
$$p_5 = G_b$$
$$p_6 = G_b \cdot \left(\frac{1}{\cos(\theta_l)} - 1 \right)$$
$$p_7 = G_b \cdot \left(\frac{1}{\cos(\theta_l)} - 1 \right)$$
$$p_8 = G_b \cdot \left(\frac{1}{\cos(\theta_l)} - 1 \right)$$
$$p_9 = G_b \cdot \left(\frac{1}{\cos(\theta_l)} - 1 \right)$$
$$p_{10} = G_b \cdot \left(\frac{1}{\cos(\theta_l)} - 1 \right)$$
$$p_{11} = G_d$$
$$p_{12} = t_m - t_a$$
$$p_{13} = (t_m - t_a)^2$$
$$p_{14} = \Delta t_m / \Delta \tau$$

The parameters in the left side are referred to Eq. (A.1) while the ones in the right side to Eq. (A.14).

In this case $K_{\theta t2} = c_2/c_1$, $K_{\theta t3} = c_3/c_1$, $K_{\theta t4} = c_4/c_1$, $K_{\theta t5} = c_5/c_1$, for $|\theta_t| < 15°$ $b_0 = c_6/c_1$, for $15° < |\theta_t| < 30°$ $b_0 = c_7/c_2$, for $30° < |\theta_t| < 45°$ $b_0 = c_8/c_3$, for $45° < |\theta_t| < 60°$ $b_0 = c_9/c_4$, for $60° < |\theta_t| < 75°$ $b_0 = c_{10}/c_5$, and $K_{\theta l} = c_{11}/c_1$.

Nomenclature

$A_{x,y}$ control element area [m^2]

A_{edge_dw} edge lateral area in the back side of the absorber plate [m^2]

A_{edge_up} edge lateral area in the upper side of the absorber plate [m^2]

A_a aperture area of the collector [m^2]

A_c reference area of the collector [m^2]

a heat loss coefficient for linear regression, Eq. (3.5) [$W/(m^2K)$]

a_1 heat loss coefficient [$W/(m^2K)$]

a_2 temperature dependence of the heat loss coefficient [$W/(m^2K^2)$]

b_0 incidence angle modifier coefficient for FPC and for longitudinal projection of angle θ in ETC [-]

b_1 incidence angle modifier coefficient in Eq. (6.2) [-]

b_2 incidence angle modifier coefficient in Eq. (6.2) [-]

b_3 incidence angle modifier coefficient in Eq. (6.2) [-]

b_4 incidence angle modifier coefficient in Eq. (6.2) [-]

c heat loss coefficient for daily linear regression, Eq. (3.9) [$W/(m^2K)$]

c_1 heat loss coefficient, Eqs. (3.6) and (6.3) [$W/(m^2K)$]

c_2 temperature dependence of the heat loss coefficient, Eqs. (3.6) and (6.3) [W/(m^{2}K^2)]

c_3 wind speed dependence of heat loss coefficient, Eqs. (3.6) and (6.3) [J/(m^{3}K)]

c_4 long wave irradiance dependence of heat loss coefficient, Eqs. (3.6) and (6.3) [W/(m^{2}K)]

c_5 effective thermal capacitance, Eqs. (3.6) and (6.3) [J/(m^{2}K)]

c_6 wind speed dependence in the zero loss efficiency, Eqs. (3.6) and (6.3) [s/m]

C_b bond (welding) conductance [W/(m K)]

c_p specific heat of the working fluid [J/(kg K)]

d internal tube diameter [m]

D external tube diameter [m]

E_L longwave irradiance (λ>3μm) [W/m^2]

F' collector efficiency factor [-]

F_R collector heat removal factor [-]

ft temperature conversion coefficient for the thermal conductivity of the back insulation [K^{-1}]

F_t corrective factor for the thermal conductivity of the back insulation [-]

F_v view factor between absorber control area and lateral surface [-]

G global solar irradiance [W/m^2]

G_b direct solar irradiance [W/m^2]

G_d diffuse solar irradiance [W/m^2]

h heat transfer coefficient [W/(m^{2}K)]

h_c corrugation height [m]

h_f heat transfer coefficient between the fluid and tube wall [W/(m^{2}K)]

K extinction coefficient [m^{-1}]

$K_{\theta b}$ incidence angle modifier for direct radiation [-]

$K_{\theta d}$ incidence angle modifier for diffuse radiation [-]

$K_{\theta l}$ incidence angle modifier for direct longitudinal radiation [-]

$K_{\theta t}$ incidence angle modifier for direct transversal radiation [-]

L tube length [m]

L_b welding length [m]

$\dot{m}$, m mass flow rate [kg/s]

n number of interval acquisitions [-]

$p_1, p_2, ..., p_M$ basic climatic quantities in multiple linear regression procedure

Q_{in} daily irradiated energy over unitary area [J/m^2] (in the graphs [kWh/m^2])

$\dot{Q}_{in}$ input power provided from the solar radiation [W]

Q_{out} daily collected energy over unitary area [J/m^2] (in the graphs [kWh/m^2])

$\dot{Q}_{out}$ useful power extracted from collector [W]

s_b thickness of the back board insulation [m]

s_{bar} distance between transversal barrier: Meyer et al. model [m]

s_c cover thickness [m]

s_{edge} distance between the edge of the back insulation board and the plate edge [m]

$s_{p\text{-}c}$ air gap thickness between plate and cover [m]

T_a ambient or surrounding air temperature [K]

t_a ambient or surrounding air temperature [°C]

t_b insulation temperature (average temperature between plate and ambient) [°C]

t_{b0} reference insulation temperature provided by the standard [°C]

t_c cover temperature [°C]

T_c cover temperature [K]

t_{in} inlet liquid temperature [°C]

T_m average liquid temperature [K]

t_m average liquid temperature [°C]

T_m^* reduced temperature difference [m^2K/W]

$T_{m\,m}^*$ daily average reduced temperature difference [m^2K/W]

t_{out} outlet liquid temperature [°C]

t_p absorber plate temperature [°C]

T_p absorber plate temperature [K]

T_s sky temperature [K]

u uncertainty

U_c overall heat loss coefficient of a collector [$W/(m^2K)$]

U_{down} bottom heat loss coefficient [$W/(m^2K)$]

U_{edge} edge heat loss coefficient [$W/(m^2K)$]

U_{tp} heat transfer coefficient between absorber plate and working fluid [$W/(m^2K)$]

U_{up} top heat loss coefficient [W/(m^{2}K)]

u surrounding air speed [m/s]

w distance between two adjacent tubes in the grid [m]

Greek letters

α absorptance of the absorber coating [-]

α_0 absorptance of the absorber coating at normal incidence angle[-]

β tilt angle of the collector [°]

δ_p absorber plate thickness [m]

ε_c emittance of the cover in the infrared wavelength range [-]

ε_p emittance of the plate in the infrared wavelength range [-]

η collector efficiency [-]

η_0 zero loss collector efficiency (η at $T_m^* = 0$) [-]

λ_b actual value for the thermal conductivity of the back insulation [W/(m K)]

λ_{b0} reference value for the thermal conductivity of the back insulation [W/(m K)]

λ_f fluid thermal conductivity [W/(m K)]

λ_p thermal conductivity of the absorber plate [W/(m K)]

$\lambda_{p\text{-}c}$ thermal conductivity of the air gap between plate and cover [W/(m K)]

λ_t thermal conductivity of the tube [W/(m K)]

θ angle of incidence [°]

θ_l longitudinal projection of angle θ [°]

θ_{ref} angle of refraction [°]

θ_t transversal projection of angle θ [°]

ϑ switching function, 0 or 1.

ρ_d reflectance of the cover for diffuse radiation [-]

σ Stefan-Boltzman constant [W/(m^{2}K^4)]

τ time interval [s]

τ_a "calculated" transmittance of a single cover [-]

τ_c transmittance of the cover [-]

$(\tau\alpha)$ effective trasmittance-absorptance product [-]

$(\tau\alpha)_{en}$ effective trasmittance-absorptance product at normal incidence [-]

Adimensional number

Nu_f Nusselt number for the working fluid [-]

$Nu_{p\text{-}c}$ Nusselt number for the air gap between plate and cover [-]

Pr Prandtl number for the working fluid [-]

Ra Rayleigh number for the air gap between plate and cover [-]

Re Reynolds number for the working fluid [-]

Subscript

b back side

Cond	conductive term
Conv	convective term
c-a	between cover and ambient
f	fluid
p-c	between absorber plate and cover
p-e	between absorber plate and lateral frame
Rad	radiative term
x,y	absorber plate element coordinate (2-D)

References

Al-Ajlan, S.A., Al Faris, H., Khonkar, H., 2003. A simulation modelling for optimization of flat plate collector design in Riyadh, Saudi Arabia, Renewable Energy 28, pp. 1325-1339.

Badran, A.A., Al-Hallaq, A.A., Eyal Salman, 2005. I.A., Odat, M.Z., A solar still augmented with a flat-plate collector, Desalinisation, vol. 172, pp. 227-234.

Budihardjo, I., Morrison, G.L., 2009. Performance of water-in-glass evacuated tube solar water heaters, Solar Energy, vol.83, pp. 49-56.

Cabanillas, R.E., Estrada, C.A., Avila, F., 1995. A device for measuring the angular distribution of incident radiation on tubular solar collectors, Renewable Energy, vol. 6, pp. 843-847.

Cadafalch, J., 2009. A detailed numerical model for flat-plate solar thermal devices, Solar Energy 83, 2157-2164.

Carvalho, M.J., Collares-Pereira, M., Correia de Oliveira, J., Farinha Mendes, J., Haberle, A., Wittwer, V., 1995. Optical and thermal testing of a new 1.12X CPC solar collector, Solar Energy Materials and Solar Cells, vol. 37, pp. 175-190.

Chow, S.P., Harding, G.L., Window, B., Cathro, K.J., 1984. Effect of collector components on the collection efficiency of tubular evacuated collectors with diffuse reflectors, Solar Energy, vol. 32, pp. 251-262.

Cucumo, M., Cucumo, S., De Rosa, A., Ferraro, V., Kaliakatsos, D., Marinelli, V., 2008. Comparison between test methods for parameters determination of flat plate solar collectors in transient conditions, 63rd ATI congress (in Italian).

Del Col, D., Padovan, A., 2007. New experimental apparatus for testing the performance of solar collectors, 62nd ATI congress.

Drummond, A.J., 1956. On the measurements of sky radiation, Arch. Meteor. Geophys. Bioklim, vol. 7, pp.413-436.

Duffie, A., Beckman, W.A., 2006. Solar engineering of thermal processes, 3rd ed., Wiley & Sons, New Jersey.

EN 12975, 2006. European Standards. Thermal solar systems and components - Solar collectors - Part 2: Test methods.

EN ISO 10456, 2008. International Standard. Building materials and products – Hygrothermal properties – Tabulated design values and procedures for determining declared and design thermal values.

Fisher, S., Heidemann, W., Muller-Steinhagen, H., Perers, B., Bergquist, P., Hellström, B., 2004. Collector test method under quasi-dynamic conditions according to the European Standard EN 12975-2, Solar Energy, vol. 76, pp. 117-123.

Gaul, H., Rabl, A., 1980. Incidence angle modifier and average optical efficiency of parabolic trough collectors, Trans. ASME J. Solar Energy Eng., vol. 102, pp. 547-551.

Grass C., Shoelkopf W., Staudacher L., Hacker Z., 2004. Comparison of the optics of non-tracking and novel types of tracking solar thermal collectors for process heat applications up to 300 °C, Solar Energy, vol. 76, pp. 207-215.

Groenhout, N.K., Behnia, M., Morrison, G.L., 2002. Experimental measurement of heat loss in an advanced solar collector, Experimental Thermal and Fluid Science, vol. 26, pp. 131-137.

Hollands, K.G.T., Unny, T.E., Raithby, G.D., Konicek, L., 1976. Free convection heat transfer across inclined air layers, Trans. ASME J. Heat Transfer, vol. 98, p. 189.

Hussein, H.M.S., El-Ghetany, H.H., Nada, 2008. S.A., Experimental investigation of novel indirect solar cooker with indoor PCM thermal storage and cooking unit, Energy Conversion and Management, vol. 49, pp. 2237-2246.

Incropera, F.P., DeWitt, D.P., 1996. Fundamentals of heat and mass transfer, 4th ed., Wiley & Sons, New Jork.

ISO, 1995, Guide to the Expression of Uncertainty in Measurement.

Kalogirou, S.A., 2004. Solar thermal collectors and applications, Progress in Energy and Combustion Science, vol. 30, pp. 231-295.

Kratzenberg, M.G., Beyer, H.G., Colle, S., 2006. Uncertainty calculation applied to different regression methods in the quasi-dynamic collector test, Solar Energy, vol. 80, pp. 1453-1460.

Kratzenberg, M.G., Beyer, H.G., Colle, S., Albertazzi, A., Güths, S., Fernandes, D., Oikawa, P.M.V., Machado, R.H., Petzoldt, D., 2005. Assessment of the partial model stability of the quasi-dynamic collector test under outdoor conditions EN 12975 by the application of uncertainty analysis, International Solar Energy Conference, Orlando – USA.

Lazzarin, R., 1981. Sistemi solari attivi, Franco Muzzio & c. editore, Padova (in Italian).

Liu, B.Y.H., Jordan, R.C., 1963. The long-term average performance of flat-plate solar energy collectors, Solar Energy, vol. 7.

Marion, W., Urban K., 1995. User's manual TMY2s - Typical Meteorological Year, National Renewable Energy Laboratory, Golden, Colorado, U.S.A.

Mathioulakis, E., Voropoulos, K., Belessiotis, V., 1999. Assessment of uncertainty in solar collector modelling and testing, Solar Energy, vol. 66, pp. 337-347.

McAdams, W.H., 1954. Heat transmission, 3rd ed., McGraw-Hill, New York.

McIntire, W.R., Reed, K.A., 1983. Orientational relationships for optically non-symmetric solar collectors, Solar Energy, vol. 31, pp. 405-410.

Minn, M.A., Ng, K.C., Khong, W.H., Melvin, T., 2002. A distributed model for a tedlar-foil flat plate solar collector, Renewable Energy, vol. 27, pp. 507-523.

Mohammed, H.A., Salman Y.K., 2007. Combined convection heat transfer for thermally developing aiding flow in an inclined circular cylinder with constant heat flux, Applied Thermal Engineering, vol. 27, pp. 1236-1247.

Nicholas, J.V., White, D.R., 1994. Traceable temperatures, Wiley series in measurement science and technology, Wiley.

Padovan, A., Del Col, D., 2010. Measurement and modelling of solar irradiance components on horizontal and tilted planes, Solar Energy, vol. 84, pp. 2068-2084.

Perers, B., 1997. An improved dynamic solar collector test method for determination of non-linear optical and thermal characteristics with multiple regression, Solar Energy, vol. 59, pp. 163-178.

Perers, B., Zinko, H., Holst, P., 1984b. Analytical model for the input/output energy relationship, Commission of the European Communities.

Perers, B., Zinko, H., Holst, P., Eriksson, L., 1984. Comparison of the effective system performance of flat plate and evacuated tube collectors used for district heating purposes in Sweden, Pergamon Press, vol. 2, pp. 1096-1105.

Phillips, W. F., 1979. The effects of axial conduction on collector heat removal factor, Solar Energy 23, 187-191.

Prapas, D.E., Norton, B., Milonidis E., Probert S. D., 1988. Response function for solar-energy collectors, Solar Energy, vol. 40, pp. 371-383.

Rojas, D., Beermann, J., Klein, S.A., Reindl, D.T., 2008. Thermal performance testing of flat-plate collectors, Solar Energy, vol. 82, pp. 746-757.

Rönnelid, M., Perers, B., Karlsson, B., 1997. On the factorisation of incidence angle modifiers for CPC collectors, Solar Energy, vol. 59, pp. 281-286.

Sabatelli, V., Marano, D., Braccio, G., Sharma, V. K., 2002. Efficiency test of solar collectors: uncertainty in the estimation of regression parameters and sensitivity analysis, Energy Conversion and Management, vol. 43, pp. 2287-2295.

Schmid, R., Collins, R.E., Mannik, E., 1984. Performance comparison of flat plate and evacuated tubular collectors used in the Sydney University solar cooling and heating project, Biennial Congress of Int. Solar Energy Society Perth 1984, vol. 2, pp. 1056-1060.

Tesfamichael, T., Wäckelgård, E., 2000. Angular solar absorbtance and incident angle modifier of selective absorbers for solar thermal collectors, Solar Energy, vol. 68, pp. 335-341.

Theunissen, P.H., Beckman, W.A., 1985. Solar transmittance characteristics of evacuated tubular collectors with diffuse back reflectors, Solar Energy, vol. 35, pp. 311-320.

VDI heat atlas/ed. Verein Deutscher Ingenieure, VDI-Gesellschaft Verfahrenstechnik und Chemieingenieurwesen (GVC) [Transl. J. W. Fullarton]. – Düsseldorf, VDI-Verl., 1993.

Zambolin, E., Del Col, D., 2010. Experimental analysis of thermal performance of flat plate and evacuated tube collectors in stationary standard and daily conditions, Solar Energy, vol. 84, pp. 1382-1396.

Zambolin, E., Del Col, D., 2010b. Development and experimental validation of a numerical model for flat-plate solar collectors, Heat Set 2010 Congress, Opatija - Croatia.

Zambolin, E., Del Col, D., Padovan, A., 2009. Experimental daily energy performance of flat plate and evacuated tube solar collectors, 3rd International Conference on Energy Sustainability ES2009, San Francisco, California, USA.